Propulsion/Airframe Integration of an Ultra High-Bypass Ratio Turbofan and a Slotted, Natural-Laminar-Flow Wing

A Thesis Presented for the

Master of Science

Degree

The University of Tennessee, Knoxville

David Edward Palmer

August 2019

© by David Edward Palmer, 2019

All Rights Reserved.

Acknowledgments

I would like to thank all of my friends and family for their love and support over the last two years. I would not have accomplished anything without their help.

I would also like to thank my advisor, Dr. Coder, for serving as my advisor and giving me the opportunity to succeed as a graduate student. I'm grateful to my committee members, Dr. Stephanie Termaath and Dr. Zhili Zhang, for their guidance and input.

This material is based upon work supported by the National Aeronautics and Space Administration (NASA) under cooperative agreement award number NNX17AJ95A. The work was performed under the University Leadership Initiative (ULI) at the University of Tennessee, Knoxville for the "Advanced Aerodynamic Design Center for Ultra-Efficient Commercial Vehicles." Any opinions, findings, and conclusions or recommendations expressed in this material are those of the author(s) and do not necessarily reflect the views of NASA."

Resources supporting this work were provided by the NASA High-End Computing (HEC) Program through the NASA Advanced Supercomputing (NAS) Division at Ames Research Center.

Abstract

Next-generation aircraft concepts such as the transonic truss-braced wing, integrate ultra-high-bypass-ratio turbofan engines and natural-laminar-flow wings. Slotted, natural-laminar-flow technology shows the potential to further reduce fuel burn. Currently, propulsion/airframe integration effects between the engine and wing are not well characterized. A representative N+3 turbofan engine model was created by scaling a NASA reference engine to the fan diameter and cruise thrust requirements of the transonic truss-brace wing. NASA's OVERFLOW computational fluid dynamics code was used to characterize a semi-infinite slotted, natural-laminar-flow wing and a representative N+3 turbofan both installed and in isolation to quantify the influence of propulsion/airframe integration on interference drag. Four engine positions were investigated: trailing-edge/over-wing, leading-edge/over-wing, leading-edge/under-wing, and trailing-edge/under-wing. It was determined that leading-edge/over-wing and trailing-edge/under-wing mounted nacelles created similar or less interference drag than conventional leading-edge under-wing nacelles at cruise conditions. The trailing-edge/under-wing had the minimum interference drag of all configurations considered. These findings show the need for full 3-D wing integration testing to accurately place the engine.

Table of Contents

1 Introduction **1**

1.1 Transonic Truss-Braced Wing 5

1.2 Slotted, Natural-Laminar-Flow Airfoils 6

1.3 Research Questions and Goals 7

2 Background **9**

2.1 Propulsion/Airframe Integration 10

2.1.1 N+3 Engine 22

2.2 Thrust-Drag Bookkeeping 24

2.2.1 Conventional Thrust-Drag Bookkeeping 24

3 Technical Approach **28**

3.1 Governing Equations 28

3.2 NASA OVERFLOW code 31

3.2.1 Roe Flux-Difference Splitting 32

3.2.2 D3ADI and SSOR 33

3.2.3 Spalart-Allmaras Turbulence Model 33

3.2.4 Coder Amplification Factor Transport (AFT) Transition Model 35

3.3 OVERFLOW Specified Massflow Boundary Condition Update 38
3.3.1 Old Algorithm 39
3.3.2 New Algorithm 39
3.3.3 Verification of the New Algorithm 40

4 Propulsion/Airframe Integration Results **44**

4.1 N+3 Engine CFD Model 44
4.1.1 Scaled NASA N+3 Reference Engine 45
4.1.2 Boundary Condition Specification 48
4.1.3 Grid Topology 48
4.1.4 Engine Model Validation 51
4.2 Slotted, Natural-Laminar-Flow Wing 53
4.2.1 Isolated S204 Semi-infinite Wing 54
4.2.2 Isolated S207 Semi-infinite Wing 54
4.3 Thrust-Drag Bookkeeping Methodology 55
4.4 S204 Semi-Infinite Wing, Flow-Through-Nacelle Study 57
4.5 S204 Semi-infinite Wing, Powered-on-Nacelle Study 60
4.5.1 Trailing-edge/Over-wing 61
4.5.2 Leading-Edge/Over-Wing 63
4.5.3 Leading-Edge/Under-Wing 63
4.5.4 Trailing-Edge/Under-Wing 65
4.6 S207 Semi-Infinite Wing Powered-on-Nacelle Study 70
4.6.1 Trailing-Edge/Over-Wing 71
4.6.2 Leading-Edge/Over-Wing 77
4.6.3 Leading-Edge/Under-Wing 81

4.6.4 Trailing-Edge/Under-Wing 85

5 Conclusions **90**

Bibliography **94**

Vita **104**

List of Tables

2.1 Cruise condition Euler and Navier-Stokes [40] 20

2.2 Summary of turbofan engines installed on a single-aisle transport (Boeing 737) in chronological order 23

4.1 NASA N+3 reference engine data at cruise conditions scaled to develop gFan+ engine model [45] 45

4.2 Comparison of prescribed and actual mass flow values for versions 1 & 2 of the duct design. 51

4.3 Drag buildup of flow-through nacelle study with S204 wing 60

4.4 Drag buildup of powered-on nacelle with S204 wing 61

4.5 Drag buildup of powered-on nacelle with S207 wing 72

List of Figures

1.1 737 aircraft with retrofitted engine technology [1] 2

1.2 Correlation between turbofan BPR and TSFC [70] 3

1.3 Common commercial transport aircraft with slightly different design missions 4

1.4 Boeing SUGAR High Transonic Truss-Braced Wing N+3 design [10] 6

1.5 S204 SNLF airfoil designed by Somers [66] 7

2.1 Jet fuel prices over time [18] 10

2.2 Aft-mounted nacelle tested experimentally by Carlson and Lamb [22] 13

2.3 Boeing 777 engine installation location compared to previous Boeing commercial aircraft [15] 14

2.4 ONERA wind tunnel setup [63] 15

2.5 HondaJet Business-Jet[4] 18

2.6 OWN configuration for commercial transport aircraft [46, 40] 19

2.7 Boeing 777 established thrust-drag bookkeeping [15] 25

2.8 Stankowski et al. [68] TDB methodology 26

2.9 The TDB methodology used by Hooker et al. [43] to compared engine configuration performance. 27

3.1 Old mass flow algorithm failure at $M_{ref} = 0.1$ 41

3.2 Setup of mass flow boundary conditions to validate new back pressure update. . . . 42

3.3 $M_{ref} = 0.5$ 43

4.1 Summary of engine ducting design process 47

4.2 Near-body grids for the N+3 representative engine (not to scale) 50

4.3 Mach number plotted for versions 1 & 2 of the N+3 representative engine OVERFLOW simulations at cruise conditions 52

4.4 Results of isolated S204 semi-infinite wing at $C_L = 0.6$ and $M_\infty = 0.745$ 54

4.5 Results of isolated S204 semi-infinite wing at $C_L = 0.6$ and $M_\infty = 0.70$ 55

4.6 Proposed thrust-drag bookkeeping surfaces: (Blue) mass-sink; (Red) nozzle inflow; (Black) ducting losses/internal drag; (Green) nacelle drag 56

4.7 C_p plotted for the isolated FT nacelle at flight conditions 58

4.8 Results of S204 wing and FT nacelle integration 59

4.9 Trailing-edge over-wing-nacelle congifuration (left) pressure coefficient (right) upper surface turbulence index 62

4.10 Leading-edge/over-wing configuration (left) pressure coefficient (right) lower surface turbulence index 64

4.11 Leading-edge/under-wing configuration (left) pressure coefficient (right) lower surface turbulence index 66

4.12 Trailing-edge/under-wing configuration (left) pressure coefficient (right) upper surface turbulence index 67

4.13 S204 surface pressure distribution for Case 1 at Y = 0 69

4.14 Engine fan face location relative to the S207 semi-infinite wing for each simulation (drawing not to scale) 70

4.15 TE OWN Cases 1-4 (left) pressure contours (right) upper surface turbulence index . 74

4.16 TE OWN Cases 5-7 (left) pressure contours (right) upper surface turbulence index . 75

4.17 S207 surface pressure distribution at Y = 0 for TE OWN configuration 76

4.18 LE OWN Cases 1-3 (left) pressure contours (right) upper surface turbulence index . 78

4.19 LE OWN Cases 5-6 (left) pressure contours (right) upper surface turbulence index . 79

4.20 S207 surface pressure distribution at Y = 0 for LE OWN configuration 80

4.21 LE UWN Cases 1-4 (left) pressure contours (right) lower surface turbulence index . 82

4.22 LE UWN Cases 5-6 (left) pressure contours (right) lower surface turbulence index . 83

4.23 S207 surface pressure distribution at Y = 0 for LE UWN configuration 84

4.24 TE UWN Cases 1-4 (left) pressure contours (right) lower surface turbulence index . 86

4.25 TE UWN Cases 5-8 (left) pressure contours (right) lower surface turbulence index . 87

4.26 S207 surface pressure distribution at Y = 0 for TE UWN configuration 88

Nomenclature

α	speed of sound
$\Delta C_{D_{nac}}$	nacelle interference drag coefficient
ΔC_{D_w}	wing interference drag coefficient
Δx	Change in x engine position
Δz	Change in z engine position
$\dot{m}_0$	mass flow rate entering engine inlet
$\dot{m}_c$	mass flow rate entering engine core
$\dot{m}_e$	mass flow rate exiting engine core
$\dot{m}_f$	mass flow rate exiting engine fan
$\dot{m}_{total}$	total mass flow rate through engine
γ	ratio of specific heats
BPR	Engine Bypass Ratio
C_p	pressure coefficient
$C_{D_{interf}}$	interference drag coefficient

$C_{D_{internal}}$ internal drag coefficient

$C_{D_{nac}}$ isolated nacelle drag coefficient

C_{D_w} isolated wing drag coefficient

cts $C_D \times 10^{-4}$

M Mach number

P_0 total pressure

T_0 total temperature

$TSFC$ thrust specific fuel consumption

V_0 free-stream velocity

V_e velocity exiting engine core

V_f velocity exiting engine fan

LE OWN leading-edge/over-wing nacelle configuration

LE UWN leading-edge/under-wing nacelle configuration

MFRC OVERFLOW Mass Flow Rate Coefficient

Re Reynolds number

TE OWN trailing-edge/over-wing nacelle configuration

TE UWN leading-edge/under-wing nacelle configuration

Chapter 1

Introduction

Early aircraft such as the one flown by the Wright brothers featured an early propeller design. In 1939 Hans von Ohain was the first to demonstrate a gas turbine engine [14], and after World War II, aircraft propulsion development soared. Propellers were fundamentally limited by how fast they could fly. At higher cruise Mach numbers, the propeller efficiency drops as the tip speed nears sonic speeds [52]. Thus, turbojets allowed faster, more efficient travel compared to the most efficient propellers. Turbojet engines also featured a much higher power-to-weight ratio compared to propellers [52]. The Boeing 707 benefitted from the implementation of the turbojet engine [70].

The advent of high-bypass turbofans made large wide-body jets like the Boeing 747 possible [70, 2]. Turbofans generated more takeoff thrust and reduced fuel consumption, and they have been continually improved since the 1960s. As the engines improved, older aircraft were retrofitted with newer, more efficient engine technology. The Boeing 737 alone has benefitted from two generations of turbofan engine development [1]. The first 737s featured JT8D turbofan engines. The 737-800 employed CFM56 engines, and the 737 Max features very efficient, quieter LEAP engines. The growth in bypass ratio (BPR) from the 737-200 to the 737 Max is evident from Fig. 1.1.



(a) Boeing 737-200 with JT8D engines [1]



(b) Boeing 737 Max with GE LEAP engines [23]

Figure 1.1: 737 aircraft with retrofitted engine technology [1]

Today, most commercial aircraft engines are very-high-bypass ratio turbofans with $BPR \approx 10$. Larger bypass ratio engines have a bigger fan diameter, which complicates the engine installation because of increased nacelle drag [64]. Thus, increasing the bypass ratio has diminishing returns [70]. This is evident from Fig. 1.2. Larger fan diameters resulted in the engine installation becoming more closely coupled to the wing [64]. The fan pressure ratio (FPR) and thrust specific fuel consumption (TSFC) are reduced. Defined as the fuel mass flow rate per unit thrust, TSFC is the standard metric to compare engine efficiency [70]. A higher BPR directly correlates to decreased TSFC, and this trend is shown in Fig. 1.2 for an engine with a constant overall thermal efficiency and turbine entry temperature. With current high BPR turbofans as a reference point, the increase in bypass ratio would ideally reduce TSFC by approximately 30%. Though the component losses increase with engine size, the limiting factor is the external drag of the nacelle and second-order effects resulting from propulsion/airframe integration (1.2). Properly integrating the engine onto the wing could mitigate the increased nacelle drag due to the larger BPR.

Propulsion/airframe integration (PAI) studies are essential to a commercial aircraft's overall success. PAI investigations usually seek to minimize interference drag, which means that the isolated nacelle drag and isolated wing drag do not equal the installed drag. As previously stated,

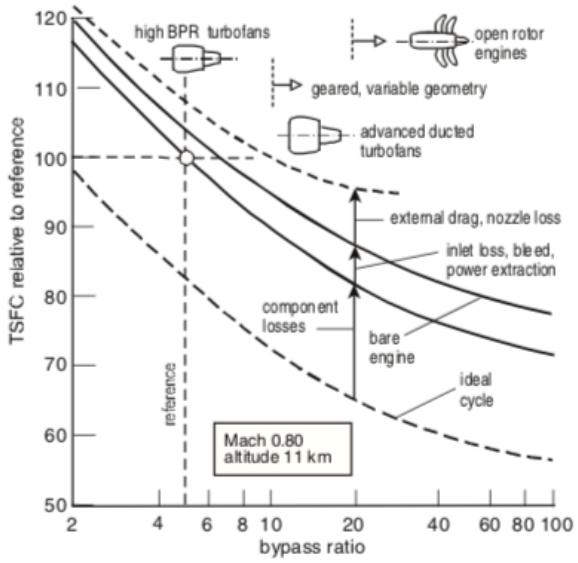


Figure 1.2: Correlation between turbofan BPR and TSFC [70]

BPRs are expected to grow for next-generation turbofans. For example, Jones and Tong [45] project next-generation turbofan engines to feature BPRs of 25 by 2035.

As the engine diameter increases, aerodynamicists must ensure that the installed engine drag does not offset the efficiency of a high-bypass ratio turbofan. Most previous and current aircraft such as Boeing's 737 and 757 implement an under-wing nacelle (UWN) configuration. The 757 (Fig. 1.3a) features turbofans with a BPR in the range from 5 to 6 [6, 8, 7]. The Boeing 737 shown in Fig. 1.1b is outfitted with a General Electric turbofan with a bypass ratio of 10:1 [5]. In the case of the 737, the ground clearance is further reduced. Landing gear can only extend so far before becoming too heavy [42]. For the Boeing 757 and 737, the larger engine diameter means that the wing and engine must be closely coupled. It is not desirable for the engine exhaust to impinge upon the takeoff/landing flaps due to thermal and vibrational loading. Thrust gates reduce the amount of lift at takeoff, and the 757 and 737 require longer takeoff distances. The flattened bottom of the 737 Max engine allows adequate ground clearance.



(a) Boeing 757 [6] **(b)** DC-9 [3]

Figure 1.3: Common commercial transport aircraft with slightly different design missions

The DC-9 was designed to serve smaller airports with shorter runways. This design consideration resulted in the engine mounted on the aft section of the fuselage where no thrust gates were needed [3]. The DC-9 (Fig. 1.3b) has shorter and lighter landing gear because of the high engines mounted on the rear fuselage, and there is no direct engine interference on the wing. The DC-9 engines shift the center of gravity aft; thus, the wing position must accommodate this change. The T-tail must be higher in order to avoid the engine exhaust from impinging upon the tail.

Traditionally, over-the-wing nacelles (OWN) induce unfavorable interference drag due to locally increased dynamic pressure and the tendency to induce a strong shock between the nacelle cowling and wing. Almost all commercial aircraft with wing-mounted engines such as the Boeing 777 placed the engine forward and under the wing [15]. Lange [49] performed an extensive study to optimize engine position of an high-bypass engine (BPR = 15) installed on a conventional tube-and-wing aircraft. It was determined that increasing the vertical distance between the wing and nacelle to its maximum distance had a favorable aerodynamic effect. The horizontal position was more complicated. Increasing the horizontal position of the nacelle did not significantly reduce drag due to superimposing drag on the wing and engine when the engine was shifted horizontally.

HondaJet designers found that for the business-jet application the over-the-wing (OWN) nacelle was optimal because this engine configuration increased the wing drag divergence Mach number and reduced cabin noise [35]. Fujino and Kawamura [35] determined that at cruise, the drag divergent Mach number of the natural-laminar-flow (NLF) wing was increased because of engine interference effects. Hooker et al. [43] found after testing 70 engine positions, that over-the-wing nacelles could increase aerodynamic efficiency up to 5% compared to the UWN for $M > 0.80$. More recent investigations [16] agree with Hooker et al. [43] that carefully located over-the-wing nacelles can have favorable interference drag if shocks between the wing and nacelle are prevented. To achieve these gains, computational fluid dynamics allows researchers to test a multitude of engine positions without the large expense of experimental setup. Future propulsion/airframe integration studies will investigate all available engine positions so that the interference effects are favorable. For a commercial transport at fixed weight and cruise speed, the drag must be minimized. Thus, eliminating interference drag associated with engine installation is of the utmost importance in designing next-generation transports.

1.1 Transonic Truss-Braced Wing

NASA and Boeing have set design goals for next-generation aircraft to keep pace with the increasing demand of commercial air transport and fuel [18]. It is expected that the tube-and-wing aircraft will need to be significantly improved upon to reach the milestones. Consequently, commercial transports are expected to look radically different in 2035. This is evident from the Transonic Truss-Braced Wing (TTBW) design shown in Fig. 1.4. Reducing fuel burn/energy consumption mitigates the environmental and monetary impact of air travel. In Boeing's Subsonic Ultra Green Aircraft Research (SUGAR) Phase I, five potential candidate designs were selected for the N+3 generation aircraft: SUGAR Free, Refined SUGAR, SUGAR High, SUGAR Volt, and SUGAR Ray.



Figure 1.4: Boeing SUGAR High Transonic Truss-Braced Wing N+3 design [10]

The SUGAR High features a high aspect ratio wing that is braced by a truss. For all potential designs, a significant reduction in fuel/energy consumption stems from the use of natural-laminar-flow airfoils [66] and advanced turbofan engines. The engine implemented on the SUGAR High is designed by General Electric, and it was termed the "gFan+". The gFan+ has a fan diameter of approximately 71-77 inches, a $BPR = 13$, and advanced geared turbofan technology [18, 17]. Along with the maturation of other next-generation technologies, the SUGAR High aims to reduce fuel burn by 70% compared to the Boeing 737 baseline aircraft equipped with CFM56 turbofan engines [18].

1.2 Slotted, Natural-Laminar-Flow Airfoils

Laminar flow airfoils achieve a laminar boundary layer over as much of the airfoil as possible. It is known that laminar flow wings are known to significantly reduce wing profile drag. Because it is estimated that one-third of the total aircraft drag of a commercial transport stems from profile drag, it is the aim of airfoil designers to maximize the amount of laminar flow [66]. Laminar boundary layers usually exist in strong favorable pressure gradients whereas turbulent boundary layers stay attached longer in adverse pressure gradients [74]. There are two well-known methods for achieving



Figure 1.5: S204 SNLF airfoil designed by Somers [66]

laminar flow [66]: natural laminar flow airfoils and laminar-flow-control (LFC). NLF airfoils use airfoil shaping techniques to allow laminar flow over both the upper and lower surfaces [66]. LFC uses suction to impart momentum into the boundary layer [74]. This approach is complex, but 100 % laminar flow can be achieved. An alternative presented by Somers [66] is slotted, natural-laminar-flow (SNLF) airfoils. SNLF airfoils allow the pressure at the trailing edge of the fore element to not recover to freestream pressure [66]. Somers [66] determined that this effect creates a favorable pressure gradient that can extend further back on the airfoil. Because of the favorable pressure gradient, the large amounts of laminar flow are achieved [66]. SNLF airfoil show the potential to even further reduce drag versus NLF airfoils. The S204 design by Somers [66] is shown in Fig. 1.5.

1.3 Research Questions and Goals

Future commercial aircraft such as the transonic-truss braced wing are expected to decrease fuel/energy consumption with natural-laminar-flow (NLF) wings and high-bypass turbofan engines. NLF wings, including the SNLF concept, offer lower drag due to the large amounts of laminar flow over the wing at cruise conditions. Currently, the influence of a high-bypass ratio turbofan installed on a SNLF wing is unknown. It is essential that the decreased fuel/energy consumption of due to the NLF wing is not lost when the engine is installed; thus, propulsion/airframe interference effects must be characterized using CFD for potential engine locations. Both conventional and unconventional engine positions must be investigated (i.e. over-the-wing, under-the-wing, etc.), and will provide insight into how to answer the following guiding questions:

1. How does a high-bypass ratio engine influence laminar flow over the slotted, natural-laminar-flow wing at cruise conditions?

2. What position of the engine relative to a slotted, natural-laminar-flow wing minimizes interference drag at cruise conditions?

Without a CFD engine model, it was impossible to accurately simulate propulsion/airframe integration effects. Currently, engine models are developed in house [68, 16]; therefore, a major obstacle to simulating integration effects is the development of an accurate CFD engine model. It is of community interest to have an N+3 engine model to simulate engine integration effects using CFD. This research developed an engine model using an outer cowling supplied by Boeing. A 0-D model was used to predict the core geometry and mass flow at key engine stations. The mass flow was matched and verified using the structured, overset CFD code OVERFLOW.

Chapter 2

Background

It is in the commercial aircraft industry's interest to develop fuel efficient transports for future generations. The conventional "tube-and-wing" design may be fundamentally limited in performance, and airframers such as Boeing are invested in the development of new concepts for reducing fuel/energy consumption of aircraft. Fig. 2.1 shows the uncertainty of fuel price per gallon. NASA has set a goal of reducing fuel burn by more than 70% for N+3 aircraft (2030-2035) to allow for market growth, rising fuel prices, and reducing aircraft emissions [18], and a large amount of this reduction stems from improved turbofan engine technology [18]. Turbofans have been used on commercial aircraft since the Boeing 747, and progress towards more efficient engines has been slow and steady [70]. This thesis used the following naming convention for turbofan sizing [64, 65]:

- Low-Bypass Ratio (LBPR) $\leq$ 1 - 3
- High-Bypass Ratio (HBPR) $\approx$ 4 - 9
- Very-High-Bypass Ratio (VHBR) $\approx$ 10 - 14
- Ultra-High-Bypass Ratio (UHBR) $\approx$ 15 - 25

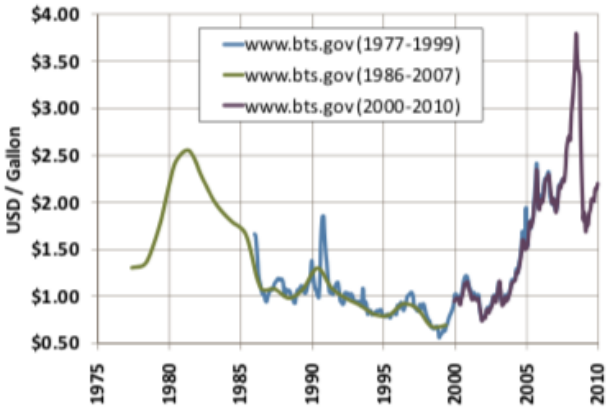


Figure 2.1: Jet fuel prices over time [18]

2.1 Propulsion/Airframe Integration

It has long been known that the sum of the drag on an isolated wing and and isolated engine is not equal to the drag on the installed wing/engine combination. The change in drag associated with installation effects is termed interference drag. Hoerner [41] defines interference drag as being two components that are placed in close proximity to each other so that their installed drag is different than their isolated component drag. Because interference drag can be as high as three to five percent of total aircraft drag, aircraft designers prefer to install the engine at a position where the interference drag is minimized, and sometimes it is possible to achieve negative interference drag [22, 31].

In 1972 the Advisory Group for Aerospace Research and Development (AGARD), held a lecture series detailing the challenges and phenomena of propulsion/airframe integration [32, 44, 12, 33, 75]. Ferri [32] concluded that while numerical methods were not trusted in 1972, they should be developed and matured along with experimental methods. Typical engine integration studies at that time focused on optimizing the inlet or exhaust of the engine, rather than engine location [12, 44, 75]. This was attributed to both the inaccuracy of computational methods and engine developers' preference for clean, uniform inflow into the engine. This meant that the engine was

mounted on a pylon and below and ahead of the wing for commercial transports. Jaarsma [44] acknowledged that it is essential to characterize the isolated engine before combining the wing and engine so that each force is accounted for only once. In order to correctly characterize an engine, proper definitions of thrust and drag must be developed [33]. This is discussed in further detail in Section 2.2.1 below.

As bypass ratios and engine fan diameters grew, research and development was needed to ensure the accuracy of commercial airplane interference drag measurements. There were many methods of simulating a powered engine experimentally. The major methods used to simulate engines were flow-through nacelles (non-powered), powered nacelles (blowing), turbine powered simulators (TPS), and inlet models with TPS representing the state-of-the-art capability in 1981. Many propulsion/airframe integration studies investigated engine positions of a flow-through nacelle as a starting point. Once poor engine configurations are eliminated, powered-on engines are studied for a select few engine positions [31].

NASA Langley became an active investigator of the interference drag between bypass nacelles and supercritical wings starting in the late 1970s and early 1980s. The United States wanted to maintain its lead in the commercial aviation industry by taking full advantage of larger bypass ratio engines [39, 21, 61, 37]. Reubush [61] simulated the effects of an over-the-wing nacelle in the Langley 16-ft transonic wind tunnel and concluded that in some cases the wing/body interference drag could be negative. Nacelle drag could not be considered because it was non metric. The most feasible configuration placed the nacelle at 25% wingspan with the nacelle 1 fan exit diameter above the wing and 1.5 fan exit diameters aft of the leading edge. Reubush [61] stated that a proper investigation should be done to consider nacelle drag.

Henderson and Patterson [39] reviewed the following nacelle positions:

1. Upper surface nacelle

2. Over-the-wing nacelle
3. Wing-aft-mounted nacelle
4. Conventional under-wing nacelle

Henderson and Abeyounis [38] investigated the promising over-the-wing nacelle position described by Reubush [61] on a high-wing transport aircraft, It was found that even with contouring the engine and pylon, the increase in interference drag was "excessive." Under-wing nacelles integrated onto supercritical wings were previously shown to influence the surface pressure distribution along the entire wingspan. This had the effect of locally reducing lift. Henderson and Patterson [39] reviewed the engine position studies listed above. Henderson and Patterson [39] determined that interference drag must be accounted; furthermore, interference drag could be minimized for a supercritical wing. It was determined that engine position had a large influence upon the interference drag along with contouring the pylon. Lee and Pendergraft [51] added that higher bypass ratio nacelles must have high clearance between the nacelle and wing to reduce interference drag.

A few years later in 1987, NASA Langley researchers investigated nacelle positions to determine potential future candidate configurations for future aircraft [22]. Carlson and Lamb [22] stated that nacelle position, nacelle geometry, and pylon contouring could be optimized for the current under-wing engine designs, and potential positions for future aircraft include: upper surface, over-the-wing, and under-the-wing aft-mounted. The aft-mounted nacelle is shown in Fig. 2.2. Carlson and Lamb [22] agreed with Reubush [61] that contouring the pylon was beneficial. The aft-mounted nacelle created a local increase in lift due to high pressure region at the nacelle inlet [22]. The engine increased lift much like a trailing-edge flap [22].

Henderson [37] investigated methods to reduce interference drag on transport aircraft by placing the nacelle below the wing and contouring the pylon/wing junction. In this study, it was shown that

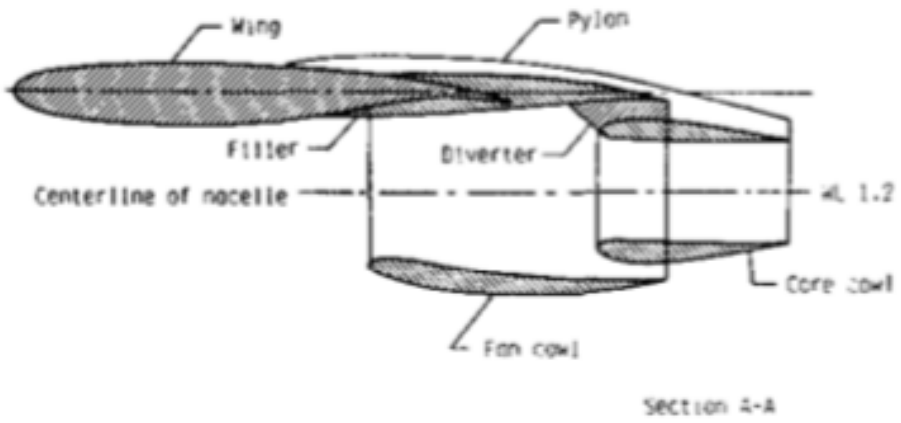


Figure 2.2: Aft-mounted nacelle tested experimentally by Carlson and Lamb [22]

placing the engine below the wing where the inlet is located at approximately 70% chord, negative interference drag is possible. Henderson [37] expected that even for very high-bypass ratio engines ($BPR \approx 20$), interference drag could be eliminated [37]. It was further shown that under-the-wing aft-mounted nacelles achieved higher cruise lift was achieved compared to the conventional engine location [37]. These findings agreed well with Carlson and Lamb [22].

In 1994, the efforts of the Langley propulsion/airframe interference effects team contributed to the development of the Boeing 777 commercial airliner [15]. Berry [15] states, "The 777 airplane presented a unique challenge due to the size and complexity of the powerplants involved ..." The GE-90 engine featured a $BPR = 9$ and a low fan nozzle pressure ratio at cruise. The lower FPR resulted in fewer blowing drag counts [15]. The high-bypass engines designed by GE, Rolls-Royce, and Pratt & Whitney were for the first time implemented in a Boeing commercial aircraft [15]. While Langley scientists showed that an interference benefit is possible with proper engine configuration, Boeing placed the 777 engines in a conventional fashion because of the complicated nature of installing the engines. The 777 engine location relative to the wing is illustrated in Fig. 2.3, and it is also compared to previous aircraft engine positions. Boeing incorporated CFD in the

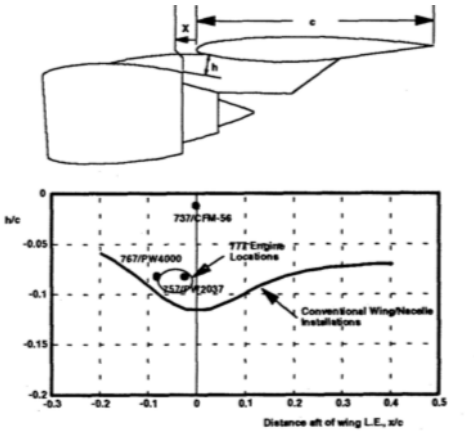


Figure 2.3: Boeing 777 engine installation location compared to previous Boeing commercial aircraft [15]

design process, but while CFD was overall helpful, the drag data was not reliable enough to make confident decisions based solely on CFD [15].

Rossow et al. [63] recognized that future engine BPR could range from 5 to 15. It was essential that these effects be better understood through experimental and computational testing. DLR and ONERA collaborated for a study of propulsion integration effects on a DLR-F4 configuration. The propulsion was modeled using flow-through nacelles to simplify the analysis. The engine was placed where strong interference effects are known to exist. A Euler (compressible, inviscid) solver was used to simulate the influence of propulsion installation on the wave drag. Rossow et al. [63] used a central differencing finite volume scheme with artificial dissipation. An explicit Runga-Kutta scheme was used to integrate the Euler equations in time. The DLR-F4 geometry was discretized on a body-fitted structured mesh. The solver, CEVCATS, was validated against the experimental setup shown in Fig. 2.4. The experimental tests covered a range of Mach numbers starting with the high subsonic regime deep into the transonic regime ($M = 0.82$). The Reynolds number was held constant at 3×10^6. In order to simulate the inviscid flow around the wing numerically, viscous effects were taken into account. The CFD simulation included the displacement thickness into the

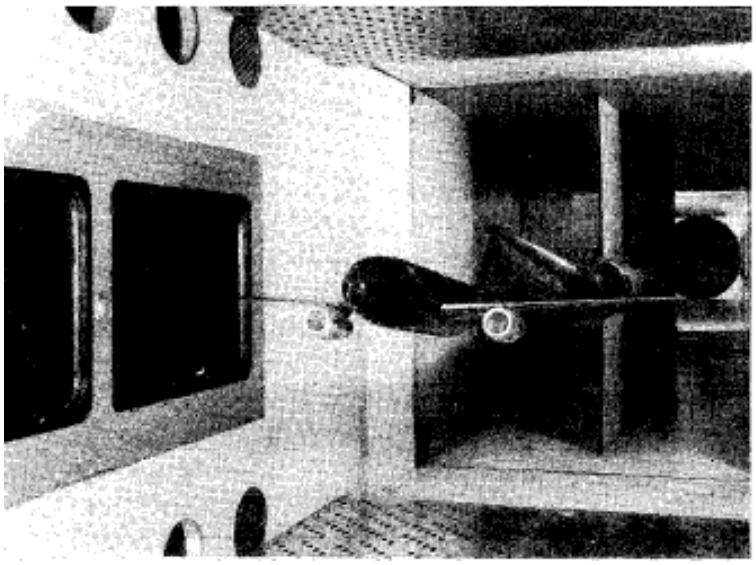


Figure 2.4: ONERA wind tunnel setup [63]

model geometry. The displacement thickness was calculated using a boundary-layer code coupled with a potential flow solver [63].

In another study, Rossow and Hoheisel [64] modeled the same "Airbus-type" aircraft given by the DLR-AVAST wind tunnel model. Interference effects of a standard CMF-56 turbofan ($BPR \approx 5$), VHBR, and UHBR engine were compared. Inviscid jets were used to model the propulsion effects in the same CEVCATS code used by Rossow et al. [63]. Rossow and Hoheisel [64] used the same numerical scheme as Rossow et al. [63] for the advective and time discretization of the Euler equations. It was determined that the very-high-bypass ratio (VHBR) and through-flow nacelle (TF) had unchanged interference drag for the same position [64]. As the UHBR engines was moved vertically closer to the wing, the pressure distribution was unchanged, but moving the engine downstream and horizontally closer to the wing exacerbated the suction peak under the wing [64]. The low-pressure region was created by the fan exhaust interfering with the wing lower surface. This low-pressure region resulted in a local loss of lift and unfavorable interference drag [64].

Kinney et al. [46] used an unstructured Full Potential solver to investigate whether an over-the-wing nacelle was viable for a subsonic transport. Up to this point, most of the successful OWN

used Upper Surface Blowing (USB) for short takeoff and landing. Kinney et al. [46] believed that investigating a commercial transport without USB was worthwhile. Galerkin Finite Element was used, and upwinding was introduced in supersonic regions. An implicit time marching scheme was used to discretize time. The OWN design is based on an UWN transport design. The pylons were removed, and the engine is attached directly to the wing upper surface [46]. Kinney et al. [46] found that near cruise Mach numbers ($M \approx 0.78$) the overall inviscid aircraft drag was comparable to conventional transport configurations. Below $M \approx 0.78$ the OWN had more interference drag than the typical UWN.

Broderson and Stürmer [20] calculated the installation drag of VBPR nacelles at $M_\infty = 0.75$ for the DLR-F6 configuration. Instead of solving the compressible, inviscid Euler equations, Broderson and Stürmer [20] solved the Reynolds Averaged Navier-Stokes (RANS) equations with the Spalart-Allmaras turbulence model. It was possible to easily obtain drag and lift using viscous CFD. The simulation did not require the viscous correction used by used by Rossow et al. [63]. Broderson and Stürmer [20] showed that the RANS solver was consistent and accurate for calculating installation drag. The calculated installed drag varied from the experiment by only 1%. Rudnik et al. [65] compared propulsion/airframe interference effects for an Euler code, an Euler code with viscous correction, and a RANS solver. It was determined that a high-bypass ratio nacelle induces a local lift loss upon the wing, and this effect is lessened if the nacelle is shifted further upstream of the wing. Rudnik et al. [65] concluded that in general previously validated codes are capable of simulated propulsion/airframe interference effects.

Rudnik et al. [65] acknowledged that the propulsion/airframe integration of large bypass engines is dominated by engine position while nacelle, pylon, and wing shape play a smaller role. It was determined that for a traditional engine placement the local lift loss is proportional to engine size [65]. Shifting the engine horizontally upstream of the wing reduced interference effects for a

VBPR turbofan while increasing the vertical distance between the engine and wing did not have a significant effect [65]. This result agreed well with Rossow and Hoheisel [64].

In 2001, the first drag prediction workshop (DPW1) was held to assess the accuracy of current 3D RANS methods. The 2nd workshop (DPW2) focused on the ability to capture airframe interference effects. In this workshop, the DLR-F6 wing/body(WB) and wing/body/nacelle/pylon (WBNP) were simulated. Experimental data showed that the drag due to the nacelle/pylon was 43 counts (1 drag count $= C_D \times 10^{-4}$), but the calculated drag was about 60-63 counts. Most of the participants over predicted lift and under predicted drag coefficients [48]. Overall, RANS methods in 2003 could not accurately predict aircraft drag because of the severe pockets of flow separation [73].

Langtry et al. [50] used the CFX-5 code from ANSYS and the shear stress turbulence (SST) model. Although the results of Langtry et al. [50] agreed well with experimental data, most of the DPW2 participant's calculations did not. Most of the DPW2 participants used the Spalart-Allmaras (S-A) turbulence model, which was known to slightly underpredict the amount of separated flow in strong adverse pressure gradients [50]. Langtry et al. [50] believed that the SST model more accurately captured the separation bubble between the fuselage and wing, and that the S-A model could be adjusted to better capture flow separation. The Quadratic Constitutive Relation (QCR) for turbulent stresses arose from the DPW2, and it is now the standard used to simulate juncture-flows accurately [73].

Fujino and Kawamura [35] studied the over-the-wing (OWN) engine concept (HondaJet Business-jet) because Reubush [61] and Henderson and Abeyounis [38] showed its potential for positive interference effects. For a business jet, the under-wing engine position is not viable due to lack of ground clearance. An Euler code with artificial dissipation and Runge-Kutta in time was used to study the interference effects of the configuration shown in Fig. 2.5. The airfoil used to define the wing is a natural-laminar-flow airfoil with a favorable pressure gradient back



Figure 2.5: HondaJet Business-Jet[4]

to 45% chord. Fujino and Kawamura [35] compared all CFD calculations with experimental results. Because the HondaJet utilizes a natural-laminar-flow wing, the authors aimed to minimize interference drag and the strength of the wing upper-surface shock wave. Fujino and Kawamura [35] determined that a powered-on engine did not have a significant influence on wave drag at cruise Mach numbers. Multiple engine positions were tested (conventional UWN, trailing-edge UWN, and OWN). It was found that the TE OWN raised the drag divergence Mach number. The under-wing nacelle performed worse than the OWN. No interference drag calculations were given. It was concluded that the wave drag could be minimized by placing the engine so that:

1. The nacelle duct inlet should be located near the shock position of the clean wing.
2. The vertical distance between the nacelle bottom and wing upper surface is between $\frac{1}{3}$ to $\frac{1}{2}$ the maximum nacelle diameter.

Hill et al. [40] aimed to examine the effects of viscosity (i.e. shock-induced separation) of interference drag for an OWN configuration originally studied by Kinney et al. [46]. Fig. 2.6 shows

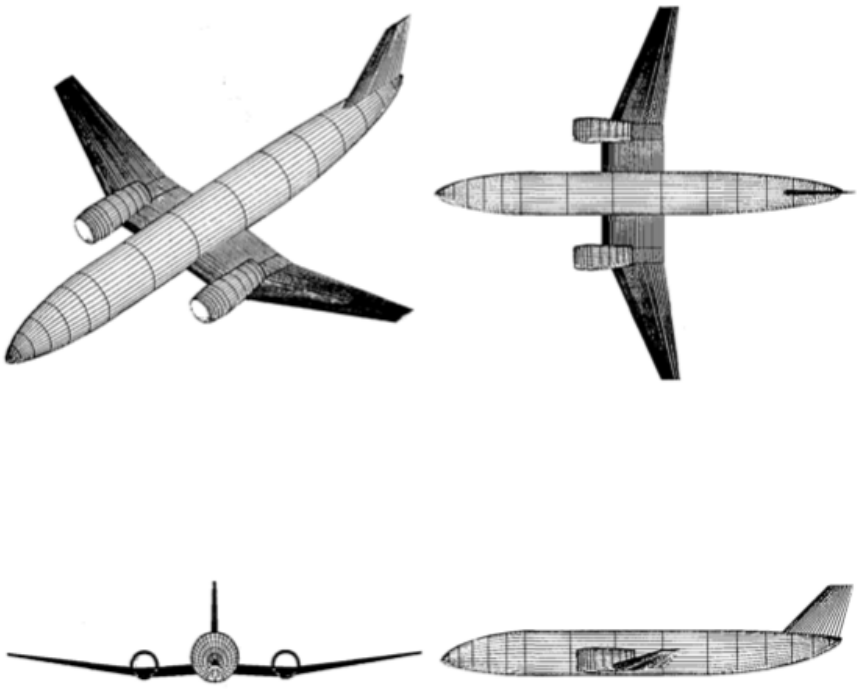


Figure 2.6: OWN configuration for commercial transport aircraft [46, 40]

the wing inboard of the nacelle has a constant chord that extends to near the nacelle lip. This region is intended to create a channel like effect on the wing. The channel is intended to create a large low-pressure region that acts forward which will negate the overall drag on the aircraft. The wing upper surface shock is moved forward, but this effect is by design since the longer chord length accounts for the loss of lift generated by the further upstream shock location compared to conventional wings.

Hill et al. [40] compared Euler and Navier-Stokes solvers for validation against experimental data. This study generated unstructured grids using VGRID, and the CFD solver USM3D was used. USM3D uses an upwind, cell-centered, finite volume scheme with the Roe approximate Riemann solver. The authors ensured the mesh at the predicted shock locations was fine enough to avoid excessive smearing the shock waves. The cases were run as fully turbulent with the

Table 2.1: Cruise condition Euler and Navier-Stokes [40]

Alt = 35,000 ft, Mach 0.78, $C_L = 0.44$, $Re_L = 41.1 \times 10^6$				
Euler Grids	C_{Dp}	C_{Dv}	C_D	L/D
OWN	0.0188		0.0188	
UWN	0.0178		0.0178	
WB	0.0142		0.0142	
Fine NS Grids				
OWN	0.0247	0.0087	0.0334	13.2
UWN	0.0210	0.0092	0.0302	14.6
WB	0.0169	0.0069	0.0238	18.5

Spalart-Allmaras one-equation turbulence model. The code was validated by simulating the DLR-F6 wing-body-nacelle-pylon configuration, and the results of this were compared to data from the 2nd Drag Prediction Workshop [40].

It was determined that the Euler solver did not properly capture shock-induced flow separation due to the inviscid nature of the scheme. Compared to the Navier-Stokes solver, the Euler code drastically under-predicted drag at cruise conditions. This is shown in Table 2.1. The Euler solver did not capture the shock-induced flow separation, and Hill et al. [40] cite this as the reason for the discrepancy between the Euler and N-S pressure drags. Thus, a Navier-Stokes solver better captures the influence of propulsion integration for transonic cruise Mach numbers. Hill et al. [40] stated that the excess drag of the OWN was due to the interior drag of the nacelle; thus, a powered-on engine must be investigated to better characterize interference effects.

Hooker et al. [43] used CFD to simulated a variety of engines at many different locations to determine if the OWN could improved energy efficiency. The effect of configuration type, engine size, engine placement on the aircraft performance was studied for difference powered-on engines. The "slipper-wing" configuration was tested based on the work by Hill et al. [40]. The flow solver USM3D was used with unstructured grids to solve the Reynolds Averaged Navier-Stokes equations. A finite volume method was used with upwind flux differencing. A total of 1,548 N-S CFD simulations were carried out with 70 engine positions investigated. Hooker et al. [43] found

that up to 5% energy reduction was possible with an OWN configuration as long as it is carefully designed. This conclusion agrees well with Blaesser et al. [16]; however, the UWN is simpler because there is a smaller risk of an adverse interaction between the nacelle and wing.

CFD has allowed the investigation of unusual engine positions, especially over-the-wing concepts that may be used for future high-bypass ratio turbofans [43, 16]. More conventional engine locations have also been optimized. Stankowski et al. [68] assessed the influence of engine position, size, and power settings for a conventional, 300-seat aircraft at cruise with the engine located under the wing. It is estimated that for this type of aircraft, two turbofan engines account for 10-15% of the total aircraft drag. The propulsion integration study simulated the nine engine positions, and extrapolated all positions in between to approximate the optimum. Stankowski et al. [68] used a commercial CFD code, ANSYS Fluent. This study used the RANS equations and the $k-\omega$ shear stress transport (SST) turbulence model. The authors validated the clean aircraft model by comparing mesh and turbulence model dependence compared to the DPW6. Two powered-on engines were simulated. Engine 1 (E1) implemented current engine thrust requirements while Engine 2 (E2) had a larger fan diameter ($D_{fan,E2} = 1.23 D_{fan,E1}$) [68]. The smaller engine was found to have better net aircraft performance on account of lighter weight. The positions with the most vertical distance between the nacelle and wing had the least amount of interference drag [68].

Lange [49] optimized the engine configuration for a turbofan with a $BPR = 15$ at cruise conditions. The engine was placed in the conventional, under-wing, fore position with varying horizontal position, vertical position, toe-in angle, and pitch angle. Lange [49] used a DLR optimizer tool to find the optimum engine configuration. The optimizer increase the vertical distance between the wing and engine to the largest possible amount. This result agrees well with other propulsion/airframe integration studies [51].

Overall, literature states that engine position is heavily dependent upon mission requirements [35, 16, 43]. The trailing-edge/over-wing position is viable for commericial transports cruising above $M = 0.80$ [43, 16]. For conventional aircraft, the leading-edge/under-wing engine position can be closely coupled without larger interference drag penalties [64, 65, 49]. The leading-edge/over-wing and nacelles show the potential for efficient configurations, but not as efficient as the conventional under-wing nacelles [46, 40, 37]. Trailing-edge/under-wing nacelles show the potential for eliminating interference drag [37, 39, 22], but clearance issues do not make them feasible for current transport aircraft.

2.1.1 N+3 Engine

Aircraft entering service during the 2030-2040 timeframe are considered N+3 aircraft, or aircraft in service three generations from now. Engines installed on these aircraft are expected to be highly efficient compared to todays turbofans [45]. Jones and Tong [45] expect that N+3 engines will feature a 52 decibel reduction in noise, 50% reduction in NOx emissions, and a 60% reduction in overall aircraft fuel burn compared to the baseline CFM56-7B engines. Because of the popularity of single-aisle transports, reducing the fuel/energy consumption of regional jets is essential for next-generation aircraft to meet N+3 design goals [45, 18]. Improved performance stems from an expected advancement in engine aerodynamics, advanced cooling techniques, and composite materials [45]. It is expected that the core becomes more efficient, and the increase in bypass ratio does not solely stem from increasing the fan diameter [45].

N+3 turbofan engines are expected to have reduced FPR [45]. A lower FPR due to a higher BPR results in a lower TSFC. Lower FPR leads to a reduced exit velocity, which ultimately results in a lower nozzle exit velocity, and leads to less blowing drag from the nozzle exhaust [15]. Fan diameters are expected to range from 71 to 100 inches [17, 45]. This is a significant increase from

Table 2.2: Summary of turbofan engines installed on a single-aisle transport (Boeing 737) in chronological order

Engine	BPR	Fan Diameter (in)
JT8D	1.91:1	54.0
CFM56	5.4:1	61
LEAP	9:1	69
NASA N+3	25:1	100

current turbofan technology [5], which is evident from Table 2.2. A variable area fan nozzle allows the engine to allow the fan to operate at peak efficiency at climb and cruise conditions [45].

Boeing in a NASA-sponsored effort defined a baseline aircraft configuration for the Subsonic Ultra Green Aircraft Research (SUGAR) study to replace single aisle transport aircraft in the 2035 timeframe. The baseline configuration was labeled generation "N". Bradley and Droney [18] chose the CFM56 engine and 737 as the baseline configuration. NASA set a 70% fuel burn reduction goal for aircraft in service three generations from now ("N+3"). Boeing partnered with General Electric in SUGAR Phase I to determine challenging engine developments for a N+3 engine. These technological development goals were approximated by extrapolating data from the CFM56 engine out to 2035 [18]. The engine designed for the SUGAR High configuration was termed the gFan+ engine. The gFan+ bypass ratio and fan diameter are listed in Table 2.2. The gFan+ engine is expected to have higher bypass ratio and a larger fan diameter compared to the current turbofan technology [18].

SUGAR Phase I was only the beginning of the Boeing's BR & T investigation into advancing aircraft technology of the future. The gFan+ specifications originally had a 77 inch fan diameter; however, in Phase II the diameter decreased to 71 inches. The fan pressure ratio for the gFan+ was given as 1.35 in Phase I [18], but was later increased to 1.46 to reduce weight and drag [17]. The bypass ratio was held at 13, which is higher than any of the turbofan engines currently in service.

2.2 Thrust-Drag Bookkeeping

2.2.1 Conventional Thrust-Drag Bookkeeping

Brazier and Ball [19] defined thrust-drag bookkeeping (TDB) as successfully defining and accounting for thrust and drag acting on an aircraft. MIDAP (Ministry - Industry Drag Analysis Panel) determined that TDB was essential to determining the how to best design aircraft [55]. This is because the aircraft engine is generally designed separate from the airframe. Propulsion engineers develop the inside ducting of the engine while the aerodynamicists are typically concerned with the outer nacelle cowling. Each force acting on the engine must be accounted for only once to ensure that the drag and thrust decomposition is accurate [55]. Many different thrust drag bookkeeping methodologies have been used in practice [15, 68, 19, 63]. While all of these methods differ slightly, it is essential that the thrust-drag bookkeeping scheme is consistent throughout the design process.

Berry [15] distinguished between the thrust and drag forces by considering all forces inside of the nacelle streamtube as thrust, and forces acting outside of the nacelle streamtube were considered drag. In order to calculate the ducting or scrubbing losses of the internal nacelle, the engine statically was characterized. This procedure required a special calibration test [15]. Any change in the forces on the installed engine exhaust system due to the wing were then considered drag. The thrust-drag bookkeeping methodology is shown in Fig. 2.7 [15]. Although studying a flow-through nacelle, Rossow et al. [63] also subtracted nacelle internal losses in their bookkeeping scheme so that the internal nacelle surface is not considered drag in the thrust-drag bookkeeping methodology. The internal drag was previously approximated by ONERA based on special calibration tests done experimentally [63].

Stankowski et al. [68] used a similar bookkeeping system as Berry [15], and followed the AGARD thrust-drag bookkeeping methodology [55]. All forces inside of the nacelle act as thrust while forces

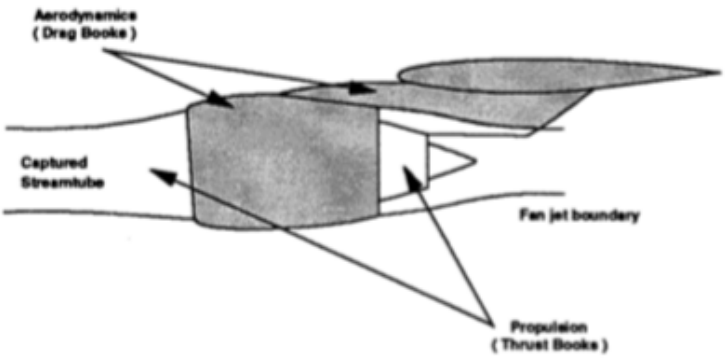


Figure 2.7: Boeing 777 established thrust-drag bookkeeping [15]

outside acted as drag [68]. These are denoted as θ and ϕ in Fig. 2.8 respectively. This is fairly trivial with the use of CFD, and usually, the thrust and drag domain are separated at the stagnation line of the nacelle [53]. Malouin et al. [53] warned that thrust and drag integration heavily depends upon the location of the stagnation line. The engine and airframe were tested in isolation at flight conditions before they were installed. Total interference drag was calculated using Eqn. 2.1. The interference thrust and interference drag were bookkept for each configuration. Then the total interference drag was a function of the installed nacelle drag, airframe drag, and thrust.

$$F_{interf} = \Delta F_N^* - \Delta D_{A/F} - \Delta D_{nac}^* \tag{2.1}$$

where

$$\begin{aligned} F_N^* &= F_N - \Theta_{exhaust} \\ D_{nac}^* &= \Phi_{pre} + \Phi_{nac} \\ \Delta D_{A/F} &= D_{A/F,installed} - D_{A/F,clean} \end{aligned} \tag{2.2}$$

Hooker et al. [43] state that CFD made the thrust-drag bookkeeping simpler since each surface can be separated into its thrust and drag contributions. While this method was similar to

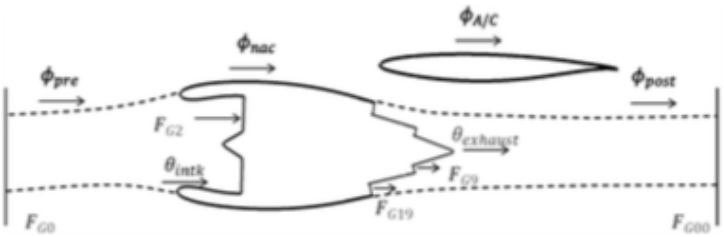


Figure 2.8: Stankowski et al. [68] TDB methodology

Stankowski et al. [68], the major difference was that the total forces and momentum fluxes were integrated over all engine surfaces. Thus, the interference thrust and drag are bookkept as the same force [43]. Hooker et al. [43] only wanted to know the net impact of the installed engine on the airframe. This led to not keeping track of thrust and drag independently. The engine and aircraft were studied in isolation, and three interference drag components were bookkept to compare the performance of each configuration. Then the total interference drag was calculated by compared the isolated components to the installed configuration. Hooker et al. [43] provide a useful chart that best describes their drag buildup (Fig. 2.9).

The method of Hooker et al. [43] simply integrates the normal force, tangential force, and momentum flux along the engine surface. Pressure act normal and viscosity acts in the direction tangential to the surface [72]. Another approach to calculating drag is by summing all the forces acting on a fluid inside of a control volume. This method is called the far-field method [72]. van Dam [72] states that the far-field method often results in spurious drag.

Drela [29] proposed a control volume analysis to assess aircraft performance; however, instead of bookkeeping the force and momentum, power and kinetic energy are calculated. This method is appropriate for complex aircraft configurations with tightly integrated propulsion (boundary layer ingestion, distributed propulsion, embedded propulsion, etc.) [29]. The method decomposes power and dissipation in the flow field through the Trefftz plane for a trimmed aircraft. Drela

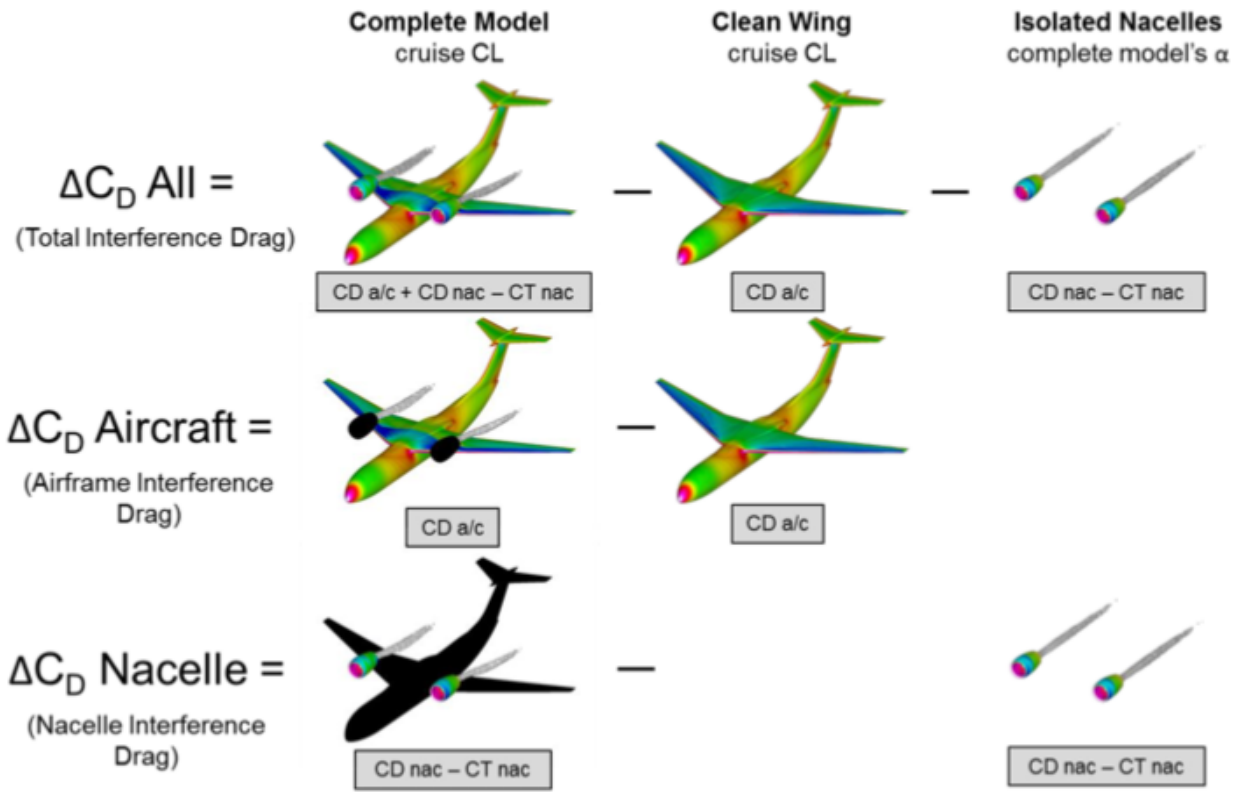


Figure 2.9: The TDB methodology used by Hooker et al. [43] to compared engine configuration performance.

.

[29] determined that the power balance method showed promise in determining interference drag origins.

Chapter 3

Technical Approach

3.1 Governing Equations

The governing equation of fluid flow at compressible Mach numbers are the compressible Navier-Stokes equations. The compressible Navier-Stokes equations were simulated using OVERFLOW, which is an implicit structured, overset solver. In their nondimensional form, the governing equations may be written as [60]

$$\partial_\tau + \partial_\xi(\hat{E} - \hat{E}_v) + \partial_\eta(\hat{F} - \hat{F}_v) + \partial_\zeta(\hat{G} - \hat{G}_v) = 0 \tag{3.1}$$

where:

$$\hat{q} = J^{-1}\begin{bmatrix}\rho\\ \rho u\\ \rho v\\ \rho w\\ e\end{bmatrix} \quad \hat{E} = J^{-1}\begin{bmatrix}\rho U\\ \rho uU + \xi_x p\\ \rho vU + \xi_y p\\ \rho wU + \xi_z p\\ (e+p)U - \xi_t p\end{bmatrix} \tag{3.2}$$

$$\hat{F} = J^{-1}\begin{bmatrix}\rho V\\ \rho uV + \eta_x p\\ \rho vV + \eta_y p\\ \rho wV + \eta_z p\\ (e+p)V - \eta_t p\end{bmatrix} \quad \hat{G} = J^{-1}\begin{bmatrix}\rho W\\ \rho uW + \zeta_x p\\ \rho vW + \zeta_y p\\ \rho wW + \zeta_z p\\ (e+p)W - \zeta_t p\end{bmatrix}$$

U, V, and W are the contravariant velocities without metric normalization, and they can be written as

$$\begin{aligned} U &= \xi_t + \xi_x u + \xi_y v + \xi_z w \\ V &= \eta_t + \eta_x u + \eta_y v + \eta_z w \\ W &= \zeta_t + \zeta_x u + \zeta_y v + \zeta_z w \end{aligned} \tag{3.3}$$

The viscous flux terms in Eq. (3.2) can then be written in terms of ξ, η, and ζ. These are given by:

$$\hat{E} = J^{-1} \begin{bmatrix} 0 \\ \xi_x \tau_{xx} + \xi_y \tau_{xy} + \xi_z \tau_{xz} \\ \xi_x \tau_{yz} + \xi_y \tau_{yy} + \xi_z \tau_{yz} \\ \xi_x \tau_{zx} + \xi_y \tau_{zy} + \xi_z \tau_{zz} \\ \xi_x \beta_x + \xi_y \beta_y + \xi_z \beta_z \end{bmatrix}$$

$$\hat{F} = J^{-1} \begin{bmatrix} 0 \\ \eta_x \tau_{xx} + \eta_y \tau_{xy} + \eta_z \tau_{xz} \\ \eta_x \tau_{yz} + \eta_y \tau_{yy} + \eta_z \tau_{yz} \\ \eta_x \tau_{zx} + \eta_y \tau_{zy} + \eta_z \tau_{zz} \\ \eta_x \beta_x + \eta_y \beta_y + \eta_z \beta_z \end{bmatrix} \tag{3.4}$$

$$\hat{G} = J^{-1} \begin{bmatrix} 0 \\ \zeta_x \tau_{xx} + \zeta_y \tau_{xy} + \zeta_z \tau_{xz} \\ \zeta_x \tau_{yz} + \zeta_y \tau_{yy} + \zeta_z \tau_{yz} \\ \zeta_x \tau_{zx} + \zeta_y \tau_{zy} + \zeta_z \tau_{zz} \\ \zeta_x \beta_x + \zeta_y \beta_y + \zeta_z \beta_z \end{bmatrix}$$

and

$$
\begin{aligned}
\tau_{xx} &= \lambda(u_x + v_y + w_z) + 2\mu u_x \\
\tau_{xy} &= \tau yx = \mu(u_y + v_x) \\
\tau_{xz} &= \tau_{zx} = \mu(u_z + w_x) \\
\tau_{yy} &= \lambda(u_x + v_y + w_z) + 2\mu v_y \\
\tau_{zz} &= \lambda(u_x + v_y + w_z) + 2\mu w_z \\
\tau_{yz} &= \tau zy = \mu(v_z + w_y \\
\beta_x &= \gamma\kappa Pr^{-1}\partial_x e_I + u\tau_{xx} + v\tau_{xy} + w\tau_{xz} \\
\beta_y &= \gamma\kappa Pr^{-1}\partial_y e_I + u\tau_{yx} + v\tau_{yy} + w\tau_{yz} \\
\beta_z &= \gamma\kappa Pr^{-1}\partial_z e_I + u\tau_{zx} + v\tau_{zy} + w\tau_{zz} \\
e_I &= e\rho^{-1} - 0.5(u^2 + v^2 + w^2)
\end{aligned}
\tag{3.5}
$$

The cartesian derivatives (u_x, etc.) are to be expanded via chain rule in ξ, η, ζ space. γ is the ratio of specific heats. κ is the coefficient of thermal conductivity, μ is the dynamic viscosity, and λ is determined assuming Stokes' hypothesis ($\lambda = -\frac{2}{3}$). The ideal gas law is assumed, so the pressure term is defined in Eq. (3.6). With the chain-rule expansions of $x_\xi, y_\xi, etc.$ the $\xi_x, \xi_y, etc.$ are solved to yield the metric terms.

$$
p = (\gamma - 1)[e - 0.5\rho(u^2 + v^2 + w^2)] \tag{3.6}
$$

3.2 NASA OVERFLOW code

OVERFLOW 2.2 uses structured, overset grids to solve the Reynolds Averaged Navier-Stokes (RANS) equations in three dimensions. OVERFLOW is a NASA-developed code capable of using

a variety of implicit numerical schemes. Many boundary conditions can be specified in the code. These include slip wall, adiabatic no-slip wall, periodic, Riemann far-field, and mass flow conditions. The current research uses OVERFLOW-D mode operation where the grids are created and the hole cutters are specified in the first step. Then the domain connectivity function (DCF) assembles the grids with the correct amount of overlap between grid cells.

In this research, Roe upwind flux-difference splitting (IRHS = 4) scheme was used to discretize the inviscid flux terms. The Spalart-Allmaras (SA-neg-1a) model with Coder SA-AFT2017b transition model was used to simulate all cases presented in this thesis [56]. The solutions were advanced to steady-state conditions using the following two implicit schemes: D3ADI diagonalized solver (ILHS = 4) and SSOR algorithm (ILHS = 6).

3.2.1 Roe Flux-Difference Splitting

Riemann solvers are essential for capturing shockwaves in compressible aerodynamics flow. Exact Riemann solvers are computationally expensive, so a number of approximate Riemann solvers have been introduced to CFD in the past 40 years [56]. This research used an approximate Riemann solver proposed by Roe [71, 62]. Following Godunov [36], the inviscid flux vector can be discretized:

$$\frac{\partial F}{\partial \xi} = F_{j+\frac{1}{2}} - F_{j-\frac{1}{2}} \tag{3.7}$$

Roe then defines the numerical flux as:

$$\hat{F} = \frac{1}{2}(\hat{F}_L + \hat{F}_R) - \frac{1}{2} \mid \hat{A} \mid (\hat{q}_R - \hat{q}_L) \tag{3.8}$$

where $\hat{A}$ is the inviscid flux Jacobian matrix defined by:

$$| \hat{A} | = \hat{T} \mid \hat{\Lambda} \mid \hat{T}^{-1} \tag{3.9}$$

The Roe scheme is known for introducing nonphysical expansion shocks. This effect arises from the scheme improperly enforcing the entropy condition, and this was fixed in OVERFLOW by holding the eigenvalues above a minimum value [71].

3.2.2 D3ADI and SSOR

This research used implicit Diagonalized Diagonal Dominant Alternating Direction Implicit (D3ADI) and the implicit, unfactored Symmetric Successive Over Relaxation (SSOR) algorithms in OVERFLOW. The D3ADI scheme is a diagonal form of the Diagonal Dominant Alternating Direction (DDADI) [13]. The D3ADI scheme is beneficial because it is more diagonally dominant than previous schemes [47]. The further diagonalization of the DDADI scheme can be achieved by incorporating the methods of Pulliam and Chaussee [59]. Diagonal schemes such as D3ADI have made OVERFLOW extremely fast in advancing the solution to steady state conditions for higher-order, upwind spatial discretizations[58]. The unfactored N-S equations can also be solved by using a relaxation method which eliminates factorization error present in diagonalization approaches. Relaxation methods do not have factorization error [58]. They require more computational work per time step since the entire flux jacobian matrix must be stored for the solution procedure [58].

3.2.3 Spalart-Allmaras Turbulence Model

The accuracy of aerodynamic flow simulations are largely dependent upon how the turbulence is modeled [50]. This research exclusively used the Spalart-Allmaras 1-equation turbulence model with the SA-neg variant [67, 11]. The turbulence model implements a transport equation for turbulent viscosity using empiricism, scaling arguments, Galilean invariance, and selective dependence upon

molecular viscosity [67]. Reynolds stresses are calculated using the Boussinesq eddy viscosity assumption:

$$-\overline{u_i' u_j} = 2\nu_T S_{ij} = 2\mu_t\Big(S_{ij} - \frac{1}{3}\frac{\partial u_k}{\partial x_k}\delta_{ij}\Big) - \frac{2}{3}\rho k \delta_{ij} \tag{3.10}$$

Since the S-A model does not directly calculate TKE, the second term on the right hand side of Eq. (3.10) is neglected in OVERFLOW, and $S_{ij} \equiv \frac{1}{2}(\frac{\partial U_i}{\partial x_j} - \frac{\partial U_j}{\partial x_i})$.

The eddy viscosity, ν_t, is determined by:

$$\nu_t = \tilde{\nu} f_{v1}, \quad f_{v1} = \frac{X^3}{X^3 + c_{v1}^3}, \quad X \equiv \frac{\tilde{\nu}}{\nu}, \tag{3.11}$$

where ν is the kinematic viscosity, $\tilde{\nu}$ is the S-A working variable and obeys the transport equation:

$$\frac{D\tilde{\nu}}{Dt} = P - D + T + \frac{1}{\sigma}\Big[\nabla\cdot((\nu+\tilde{\nu})\nabla\tilde{\nu}) + c_{b2}(\nabla\tilde{\nu})^2\Big], \tag{3.12}$$

where production, wall destruction and trip terms are

$$P = c_{b1}(1 - f_{t2})\tilde{S}\tilde{\nu}, \quad D = (C_{w1} f_w - \frac{c_{b1}}{\kappa^2})[\frac{\tilde{\nu}}{d}]^2 \tag{3.13}$$

$\tilde{S}$ equals the modified vorticity

$$\tilde{S} \equiv S + \frac{\tilde{\nu}}{\kappa^2 d^2} f_{v2}, \quad f_{v2} = 1 - \frac{X}{1 + X f_{v1}} \tag{3.14}$$

S is the vorticity magnitude, and d is the distance closest to the wall. f_w is defined:

$$f_w = g[\frac{1 + c_{w3}^6}{g^6 + c_{w3}^6}]^{\frac{1}{6}}, \quad g = r + c_{w2}(r^6 - r), \quad r = min(\frac{\tilde{\nu}}{\tilde{S}\kappa^2 d^2}, r_{lim}) \tag{3.15}$$

Finally, the trip and laminar suppression terms are defined:

$$f_{t2} = c_{t3} exp(-c_{t4} X^2) \tag{3.16}$$

The constants are $c_{b1} = 0.1355$, $c_{b2} = 0.622$, $\kappa = 0.41$, $c_{w1} = c_{b1}/\kappa^2 + (1 + c_{b2})/\sigma$, $c_{w2} = 0.3$, $c_{w3} = 2$, $c_{v1} = 7.1$, $c_{t3} = 1.2$, $c_{t4} = 0.5$ and $r_{lim} = 10$. The Prandtl number is set to 0.9 which obeys turbulent heat transfer.

3.2.4 Coder Amplification Factor Transport (AFT) Transition Model

The amplification factor transport (AFT) model uses linear stability theory in a way that is based on traditional computational fluid dynamics [26]. The model uses the method of Drela and Giles [30] where the envelope amplification factor n of the Tollmien-Schlichting instabilities is determined from (3.17). The integrand is a function of the local boundary-layer shape factor and momentum thickness. In order to simulate the impact of laminar flow over the wing, the Spalart-Allmaras (SA-neg-1a) model with Coder SA-AFT2017b transition model was used [56, 27]. It is an extension of the transition model of Coder and Maughmer [26] and Coder [25]. AFT2017b is based on the solution of two transport equations for amplification factor and modified intermittency [27]. The AFT transport equations are defined as,

$$\tilde{n} = \int_{s_0}^{s} \frac{\mathrm{d}\tilde{n}}{\mathrm{d}Re_{\delta 2}} \frac{\mathrm{d}Re_{\delta 2}}{\mathrm{d}s} \tag{3.17}$$

The local growth of the local amplification factor at any point in the CFD solution can be calculated:

$$\frac{\partial \rho \tilde{n}}{\partial t} + \frac{\partial (\rho u_j \tilde{n})}{\partial x_j} = \rho \Omega F_{crit} F_{growth} \frac{d\tilde{n}}{dRe_\theta} + \frac{\partial}{\partial x_j} \Big[(\mu + \sigma_n \mu_t) \frac{\partial \tilde{n}}{\partial x_j} \Big] \tag{3.18}$$

and

$$\frac{\partial \rho \bar{\gamma}}{\partial t} + \frac{\partial \rho u_j \bar{\gamma}}{x_j} = c_j \rho S F_{onset}[1 - exp(\bar{\gamma})] - c_2 \rho \Omega F_{turb}[c_3 exp(\bar{\gamma} - 1] + \frac{\partial}{\partial x_j}\Big[\Big(\mu + \frac{\mu_t}{\sigma_\gamma}\Big)\frac{\partial \bar{\gamma}}{\partial x_j}\Big] \quad (3.19)$$

The local boundary layer shape factor is used to approximate corresponding integral properties, and is defined as,

$$H_L = \frac{d^2}{\mu}[\nabla(\rho \overrightarrow{u} \cdot \nabla d) \cdot \nabla d] \quad (3.20)$$

Where H_L determines the integral shape factor, H_{12}, as,

$$H_{12} = 0.376960 + \sqrt{\frac{H_L + 2.453432}{0.653181}} \quad (3.21)$$

Coder et al. [27] states that is is advantageous to limit H_L so that $-0.25 \leq H_L \leq 200$. The source term is then defined by the dependencies,

$$F_{crit} = \begin{cases} 0 & Re_V < Re_{V,0} \\ 1 & Re_V \geq Re_{V,0} \end{cases} \quad (3.22)$$

$$\frac{Re_{V,0}}{Re_{\theta,0}} = 0.246175{H_{12}}^2 - 0.141831 H_{12} + 0.008886 \quad (3.23)$$

$$Re_V = \frac{\rho S d^2}{\mu + \mu_t} \quad (3.24)$$

$$\log Re_{\theta,0} = 0.7 tanh\Big(\frac{14}{H_{12} - 1} - 9.24\Big) + \frac{2.492}{(H_{12} - 1)^{0.43}} + 0.62 \quad (3.25)$$

$$F_{growth} = \frac{H_{12}}{0.5482H_{12} - 0.5185}[1 + m(H_{12}]\frac{l(H_{12})}{2} \tag{3.26}$$

$$l(H_{12}) = \frac{6.54H_{12} - 14.07}{H_{12}^2} \tag{3.27}$$

$$m(H_{12}) = \frac{1}{l(H_{12})}\Big[0.058\frac{(H_{12} - 4)^2}{H_{12} - 1}0.068\Big] \tag{3.28}$$

$$\frac{d\tilde{n}}{dRe_\theta} = 0.028(H_{12} - 1) - 0.0345exp\Big[-\Big(\frac{3.87}{H_{12} - 1} - 2.52\Big)^2\Big] \tag{3.29}$$

where the diffusion coefficient for the amplification factor is $\sigma_n = 1.0$. The source terms in (3.19) are,

$$F_{onset,1} = min\Big(\frac{\tilde{n}}{N_{crit}}, 2\Big) \tag{3.30}$$

$$F_{onset,2} = max\Big[1 - \Big(\frac{\mu_t}{3.5\mu}\Big)^3, 0\Big] \tag{3.31}$$

$$F_{onset} = max\Big[F_{onset,1} - F_{onset,2}, 0\Big] \tag{3.32}$$

$$F_{turb} = exp\Big[-\Big(\frac{\mu_t}{2\mu}\Big)^4\Big] \tag{3.33}$$

Transition occurs when the amplification factor, $\tilde{n}$, is greater than or equal to N_{crit}. Coder et al. [27] calculates the critical amplification factor as,

$$N_{crit} = -8.43 - 2.4ln\Big(\frac{\tau}{100}\Big) \tag{3.34}$$

$$\tau = 2.5tanh\Big(\frac{Tu_{\infty}(\%)}{2.5}\Big) \tag{3.35}$$

where the limiter τ, based on work by Drela [28], is used to prevent negative values of N_{crit} [27]. The calibration coefficients from Menter et al. [54] are $c_1 = 100$, $c_2 = 0.06$, $c_3 = 50$, and $\sigma_{\gamma} = 1.0$ [27]. The SA-AFT2017b is coupled to the SA model through the f_{t2} function as [27],

$$f_{t2} = c_{t3}[1 - exp(\bar{\gamma})] \tag{3.36}$$

3.3 OVERFLOW Specified Massflow Boundary Condition Update

The engine must be modeled as powered-on to properly simulate propulsion/airframe integration effects. In the CFD engine simulation, the turbomachinery can be treated as a black box. The mass flow in and out of the engine is treated with specified boundary conditions. It is desired to specify the inlet mass flow using OVERFLOW boundary condition #34. Boundary condition #34 is a mass-sink/outflow boundary condition where the mass flow through a grid face can be specified.

For this engine simulation, the inlet mass flow rate coefficient was calculated, and the fan face mass flow rate was specified through OVERFLOW boundary condition #34. This boundary condition updates the mass flow by holding the pressure at the face constant and extrapolating all other flow variables. The back pressure term is updated to converge on the prescribed mass flow parameter. The nozzle entrances are specified using the total pressure and temperature ratios. Then the mass flow is extrapolated from the upstream conditions [56].

3.3.1 Old Algorithm

The current version of the mass sink boundary condition uses an ad hoc procedure to update the exit plane pressure. With each update the code takes the specified mass-flow and the current mass-flow at the surface and performs the following calculation with a relaxation factor.

$$DP = \frac{\dot{m}_{actual}}{\dot{m}_{specified}} - 1 \tag{3.37}$$

The relaxation factor is intended ensure that the mass flow converges, but its ad hoc, non-physical nature makes the update prone to failing in some situations. This is shown in Section 3.3.2. There was a need for a better, more robust back pressure update for the mass-sink boundary condition that is better grounded in the flow physics. Thus, a new back pressure update using a Newton iteration was implemented to ensure that the boundary condition is more robust.

3.3.2 New Algorithm

The new mass-sink boundary condition update is based on 1-D compressible mass-flow equation [57],

$$\frac{\dot{m}}{A} = \sqrt{\frac{\gamma}{RT_0}} \cdot P_0 \cdot \frac{M}{(1 + \frac{\gamma-1}{2}M^2)^{\frac{\gamma+1}{2(\gamma-1)}}} \tag{3.38}$$

For each update, the algorithm retrieves the density (ρ, velocity magnitude (V_{mag}), pressure (P), total pressure (P_0), total temperature (T_0), gamma (γ), and gas constant (R) from the an integration surface. With these known quantities, the Mach number is calculated at the surface. After the Mach number is known, the code calls a subroutine to determine if the flow is supersonic. If the flow is supersonic, the subroutine chokes the flow and the mass flow is limited. If the flow is subsonic, then the subroutine does nothing. The simulation continues and the mass flow is continually updated by adjusting the back pressure. The outlet backpressure update becomes more

robust because it is a function of the flow variables, and is implemented by using a Newton iteration procedure.

$$DP = -\frac{\dot{m}_{actual} - \dot{m}_{specified}}{\frac{d\dot{m}}{dP}} \tag{3.39}$$

Taking the derivative of the compressible mass-flow equation and the isentropic pressure relation with respect to Mach number yields the ordinary derivatives $\frac{d\dot{m}}{dM}$ and $\frac{dP}{dM}$.

$$\frac{d\dot{m}}{dM} = \frac{\dot{m}}{A} \cdot (\frac{1}{M} - \frac{\gamma+1}{2} \cdot \frac{M}{(1+\frac{\gamma-1}{2}M^2)}) \tag{3.40}$$

$$\frac{dP}{dM} = -\gamma M P_0 (1 + \frac{\gamma-1}{2}M^2)^{\frac{-\gamma}{\gamma-1}-1} \tag{3.41}$$

Finally, simply dividing the two relations give the mass flow derivative with respect to pressure.

$$\frac{d\dot{m}}{dP} = \frac{\frac{d\dot{m}}{dM}}{\frac{dP}{dM}} \tag{3.42}$$

3.3.3 Verification of the New Algorithm

The new algorithm was verified using a 2-D wind tunnel test case where the old algorithm was known to fail. An S809 airfoil was simulated in a 2-D wind tunnel. The tunnel inflow was specified to freestream conditions while the mass flow was specified using the new and old algorithms. The grid topology consisted of two grids: the airfoil and the boundary box grid. A C-grid was used with a trailing edge wake cut, and the near-body grid was marched approximately 0.2 chord lengths in the wall normal direction to follow best practices in overset grid generation [24]. The grid is shown in Fig. 3.2. The box grid was placed around the airfoil to act as the wind tunnel walls, inlet, and exit. The top and bottom were prescribed as viscous adiabatic walls. The upstream side of

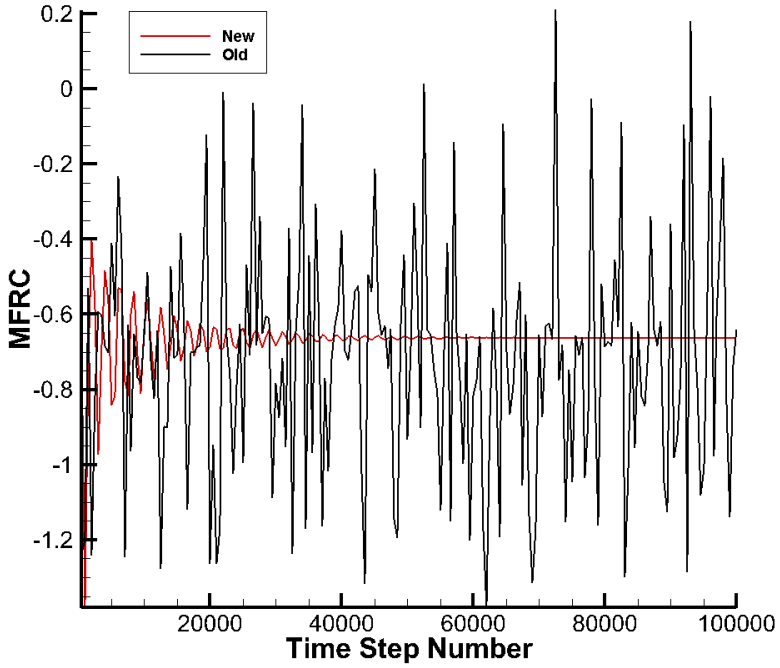


Figure 3.1: Old mass flow algorithm failure at $M_{ref} = 0.1$

the box was prescribed as the nozzle inflow while the downstream side was the outflow boundary condition to be tested (Figure 3.2. The outflow face mass flow rate coefficient was specified with an arbitrary value of $\bar{m} = 0.6627$. For a simple case such as a 2-D wind tunnel with a blockage, the old algorithm fails for small relaxation factors. This is clear from Fig. 3.1 where the old update is shown in black.

At $M_{ref} = 0.1$, the old algorithm failed to converge with a relaxation factor of 0.2. The new update was shown to converge steadily. The relaxation factor was not necessary in this case. For some conditions, OVERFLOW needs this relaxation factor because the pressure cannot be extrapolated more than 50% to adjacent cells. If the pressure is extrapolated too much, then the simulation will end. By letting the new algorithm update the backpressure less often, this issue can be avoided.

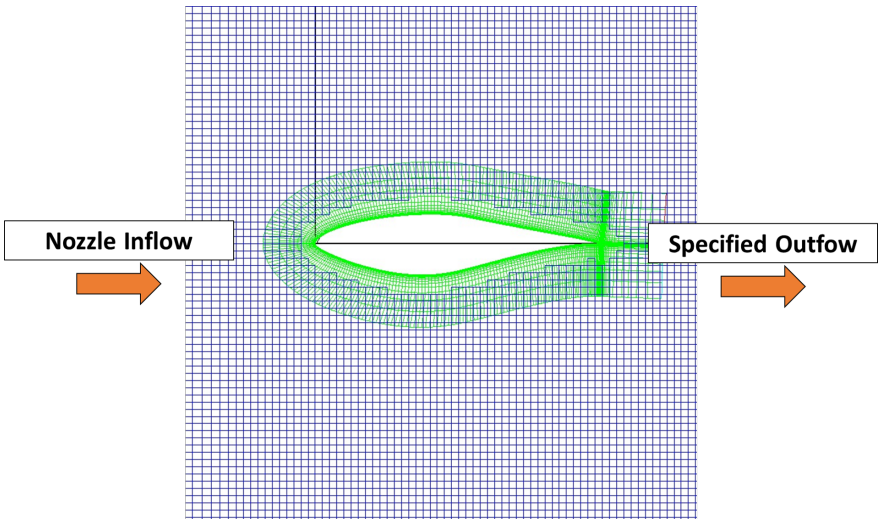


Figure 3.2: Setup of mass flow boundary conditions to validate new back pressure update.

For $M_{ref} = 0.5$, the new and old updates converge well to the prescribed mass flow value (Figure 3.3). Both the old and new updates used a relaxation value of 0.9. The new update is a function of the Mach number at the specified outflow face; therefore, the mass-flow coefficient will converge only as fast as the Mach number. It is clear that the new update shown in Fig. 3.3 converges slower than the old update for this reason. The supersonic reference Mach number is not ideal for this boundary condition. Nichols et al. [57] determined that instead of using a mass-sink to set the mass flow in supersonic simulations, it is better to specify total conditions at the inlet with a correct geometry. This method better matches supersonic mass flow as long as the geometry is correct [57].

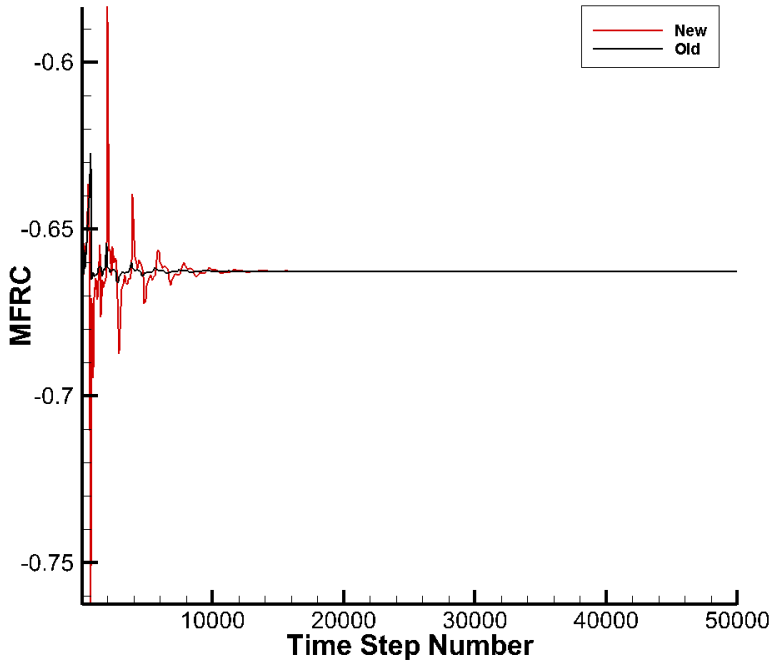


Figure 3.3: $M_{ref} = 0.5$

Chapter 4

Propulsion/Airframe Integration Results

It was the goal of this research to examine the impact of a high-bypass ratio turbofan engine on a slotted, natural-laminar-flow wing at cruise conditions. Reducing interference drag while also keeping the laminar flow benefit of the wing is key. Before a preliminary propulsion/airframe integration test could be done, a powered-on engine model was constructed. Several other researchers state the importance of simulating a powered on engine compared to a flow-through nacelle [40, 63, 68]. Flow-through engine investigations provide a reasonable first guess as to where to position the engine, but a powered-on engine is needed to properly characterize interference effects.

4.1 N+3 Engine CFD Model

Without powered-on engine geometry and mass flow data freely available, the engine model is usually up to the individual. This process can take weeks or months depending on experience and

Table 4.1: NASA N+3 reference engine data at cruise conditions scaled to develop gFan+ engine model [45]

$M = 0.80$			Altitude= 35000 ft			
Station	$\dot{m}$ (lbm/s)	P_0 (psia)	T_0 (Rankine)	Area (in^2)	M	γ
Inlet Entrance	795.64	5.272	444.41	6209.5	0.80	1.4009
Fan Entrance	795.64	5.262	444.41	7109.8	0.6015	1.4009
Fan Exit	795.64	6.717	477.58	7098.0	.4461	1.4007
Fan Nozzle Entrance	764.5	6.617	477.58	6917.7	0.4465	1.4007
Fan Nozzle Exit	764.5	6.617	477.58	4746.8	1.0000	1.4007
Core Nozzle Entrance	31.84	5.535	1246.73	945.0	0.2468	1.3499
Core Nozzle Exit	31.84	5.535	1246.73	393.4	0.8584	1.3499

available engine simulators. Stankowski et al. [69] used the in house 0-D engine modeling tool, *Turbomatch*. This code not only output mass flow and total conditions, but also generated the ducting geometry of the turbofan [68]. Thus, it was a major goal of this research to model an N+3 representative engine so that interference effects can be studied for next-generation aircraft such as the TTBW.

4.1.1 Scaled NASA N+3 Reference Engine

Jones and Tong [45] published an N+3 reference engine for a single-aisle transport where turbofan technology was extrapolated from current capabilities into the 2035 timeframe. The fan pressure ratio (FPR) was lowered to the smallest possible value so that the fan diameter was still less than 100 inches. This lead to a $BPR \approx 25$. Ideally, this would minimize the TSFC of the engine at cruise [45]. All thermodynamic properties were provided at different operating conditions, and this is shown in Table 4.1. The engine features a variable area fan nozzle so that the flow out the fan nozzle is choked at cruise conditions. The maximum mass flow out of the nozzle is allowed while the core produces only a small amount of the total engine thrust [45].

An engine model was created to simulate a representative N+3 engine at the TTBW cruise conditions. Starting with a flow-through nacelle outer cowling with an approximate $D_{fan} = 67$ inches, the fan and core nozzle duct geometry was approximated by scaling a NASA N+3 reference

engine at TTBW cruise conditions [45]. With total conditions, Mach number, γ, and N+3 areas from Jones and Tong [45], the reference engine mass flow rates were scaled with Eq. (4.1). This 0-D ducting approximation is common for CFD engine simulations [57, 16, 68].

The engine drawing given by Jones and Tong [45] was scaled to the NASA reference fan diameter of 100 inches. Assuming that core geometry contracts the flow through the fan nozzle, measurements gave a rough approximation of the NASA core geometry and radii. The NASA reference engine employs a variable-area fan nozzle (VAFN). At the fan nozzle station, the given area was used to predict the core radii. The approximated core radii match the reference engine well, so they were scaled using the fan diameter ratios. The radii yielded the approximate engine areas, which then gave the mass flow rate at each station. The gross thrust of the representative engine was within 5% error of the cruise thrust specified by Bradley and Droney [18].

The core and plug geometry were assumed axisymmetric around the given outer cowling centerline. Four inner and outer radii points were used to draw a spline curve inside of the TTBW cowling provided by Boeing. Then a surface mesh was created by simply rotating these curves about the centerline. This yielded a 3-D engine model. A convenient flow-chart describing the engine design process is shown in Fig. 4.1.

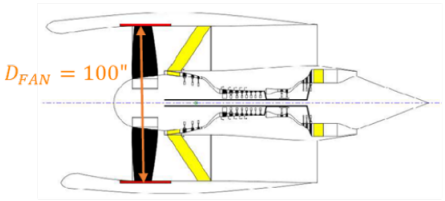
$$\frac{\dot{m}}{A} = \frac{P_0}{\sqrt{T_0}} \cdot \sqrt{\frac{\gamma}{R}} \cdot M \cdot (1 + \frac{\gamma - 1}{2} M^2)^{-\frac{\gamma+1}{2(\gamma-1)}} \tag{4.1}$$

Match $M, T_0, P_0, and\ \gamma$ at each station. → $\frac{\dot{m}}{A}$

↓

Scale NASA engine drawing to $D_{fan} = 100$ in

↓



↓

Estimate radii at most stations. At the fan nozzle exit,the given area was matched by solving for the radii using given NASA engine areas.

↓

Scale the NASA radii based on the fan diameter ratio.

$$\frac{D_{gfan}}{D_{NASA}} = \frac{67\ in}{100\ in} = 0.67$$

↓

Yields the approximate gFan+ area at each station where $\frac{\dot{m}}{A}$ is known.

↓

Use the Boeing outer cowling and scaled radii/areas to estimate core geometry.

↓

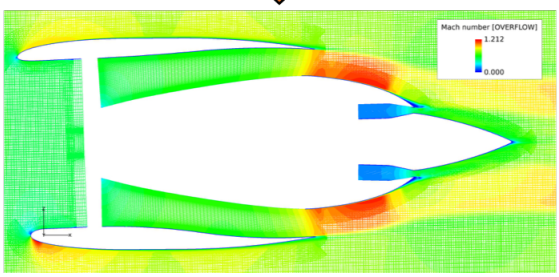


Figure 4.1: Summary of engine ducting design process

4.1.2 Boundary Condition Specification

Fig. 4.2 shows the near-body grids generated using a combination of Pointwise and NASA's Chimera Grid Tools overset, structured meshing software. Instead of modeling the inner workings of the turbomachinery, only the inlet and exit faces were prescribed using OVERFLOW boundary conditions. The inlet is simulated with a mass-sink boundary condition. The mass flow is prescribed at the inlet face and matched by the update describe in detail in chapter 3.3. Because flight conditions for the reference engine and TTBW are different, mass-flow was scaled to sea level static conditions using Eq. (4.2). At the nozzle entrances, the total temperature ($\frac{T_0}{T_{0\infty}}$) and total pressure ($\frac{P_0}{P_{0\infty}}$) are specified at the inlet face. The inflow conditions are then extrapolated from upstream [56].

$$\bar{\dot{m}} = \frac{\dot{m}_c(1 + \frac{\gamma-1}{2}M_\infty^2)^{\frac{\gamma+1}{2(\gamma-1)}}}{\rho_{sd}a_{sd}M_\infty A_{ref}} \tag{4.2}$$

where

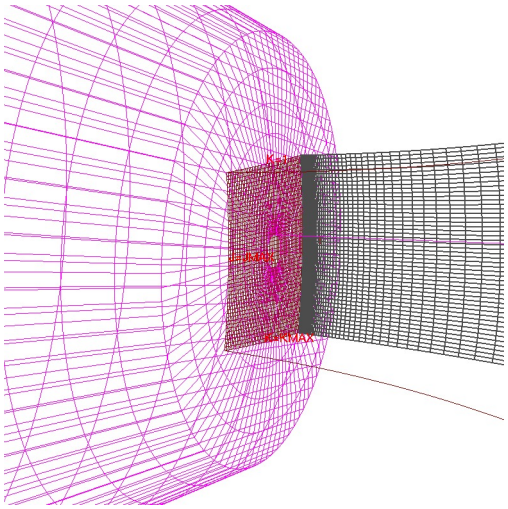
$$\dot{m}_c = \frac{\sqrt{\theta}}{\delta} \tag{4.3}$$

$$\theta = \frac{T_{0\infty}}{T_{sd}}, \delta = \frac{P_{0\infty}}{P_{sd}} \tag{4.4}$$

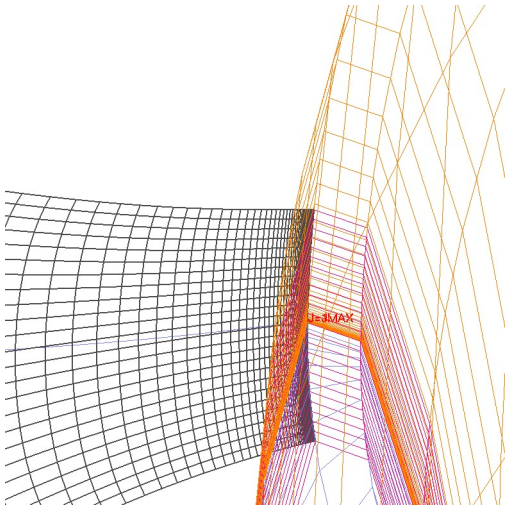
4.1.3 Grid Topology

Below in Fig. 4.2 the near-body grids are displayed. The outer cowling mainly consists of the inner and outer cowling surfaces. These grids are two separate grids; therefore, they must be joined by collars at the leading-edge and trailing-edge to prevent orphan grid cells. The collar grids are shown in detail in Fig. 4.2b and Fig. 4.2c. Following best practices, the cap grid shown in Fig. 4.2a was placed over the plug trailing edge to avoid a singular axis point [24]. The engine inlet required some special treatment because of the potential singularity point at its center. Instead of using a plug

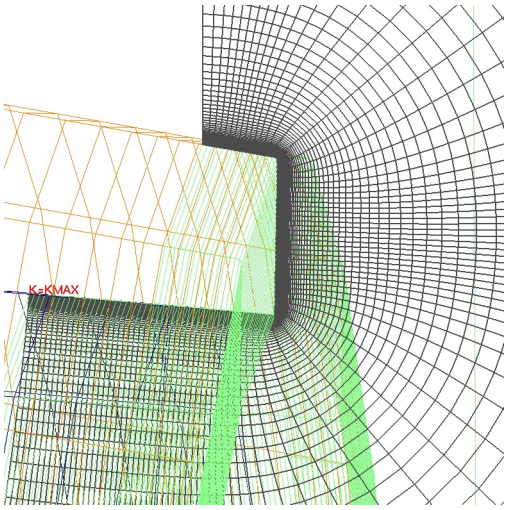
grid, a duct slit grid was generated in Pointwise. The inlet surface was extracted from the inner cowling, and a C-grid was placed around a line of points at the inlet center. The near-body grids have approximately 11.3 million grid points before hole cutting. After off-body grid generation and hole cutting, the isolated engine grid consist of approximately 18.9 million points.



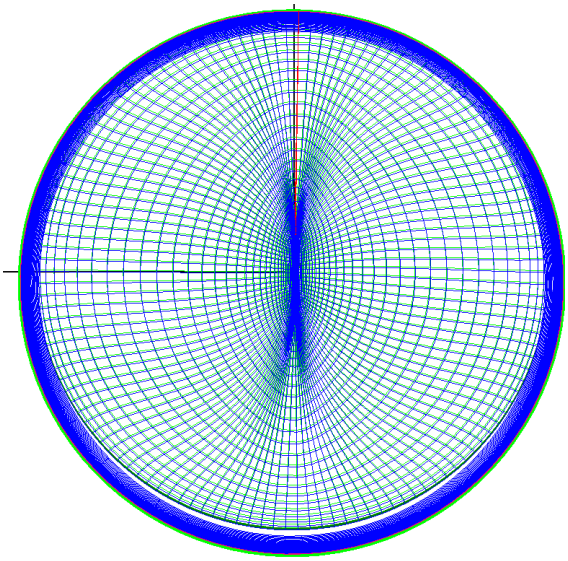
(a) Plug cap grid



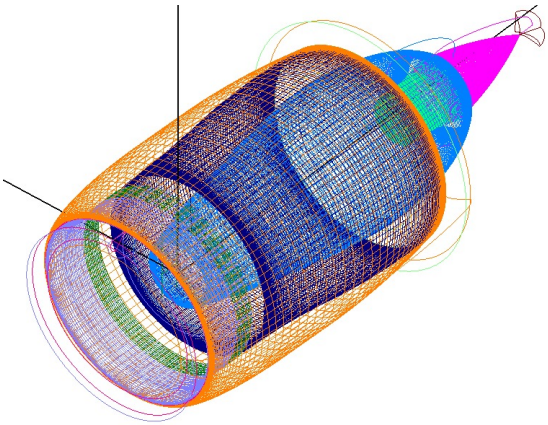
(b) Leading-edge collar grid



(c) Trailing-edge collar grid



(d) Inlet Slit Grid



(e) Combined grids

Figure 4.2: Near-body grids for the N+3 representative engine (not to scale)

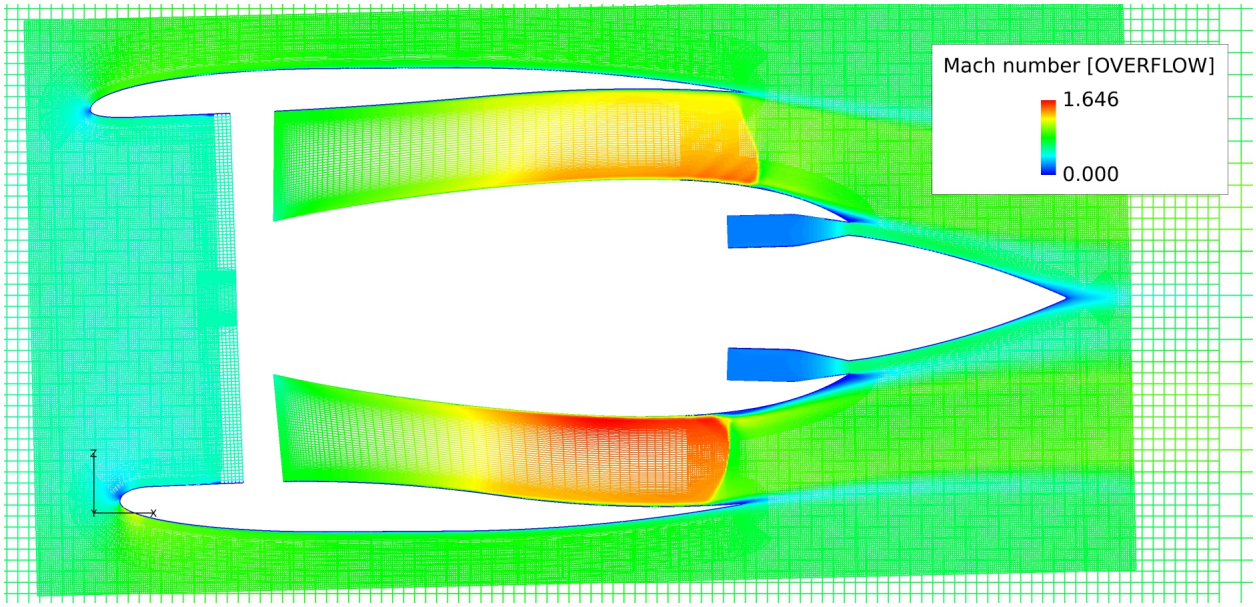
Table 4.2: Comparison of prescribed and actual mass flow values for versions 1 & 2 of the duct design.

Boundary Condition	$\dot{m}_{prescribed}$ (lbm/s)	Flight (v1), $\dot{m}$ (lbm/s)	Flight (v2), $\dot{m}$ (lbm/s)
Fan Inlet	358	357.83	357.93
Core Nozzle	14.6	13.83	11.98
Fan Nozzle	343.4	447.35	355.94

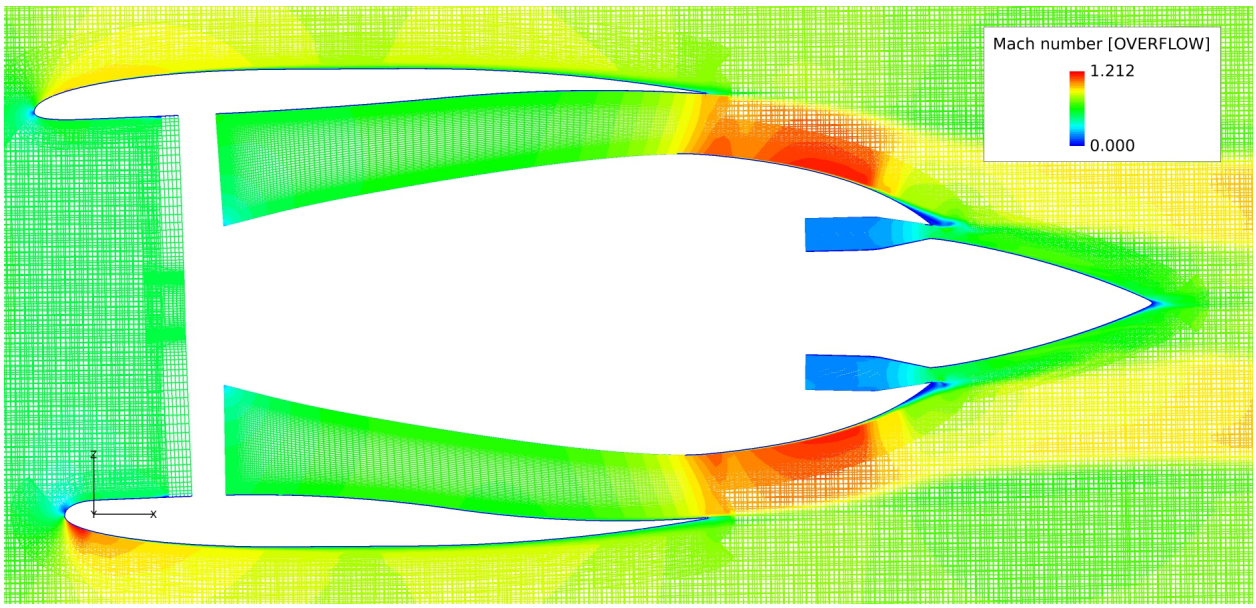
4.1.4 Engine Model Validation

The high-bypass ratio N+3 turbofan was simulated a flight conditions to validate the engine model. Fig. 4.3a shows Mach number contours plotted for the first design iteration, and the exit mass flow coefficient calculated at the boundary condition faces are compared in Table 4.2. Consistent with N+3 engine design [45], almost all of the thrust is generated by the low-pressure fan. The inlet and core nozzle mass flow rate are almost exactly the prescribed flow rates. The fan nozzle does not match the desired mass flow. Jones and Tong [45] determined that the flow out of the fan nozzle should be choked at the exit face ($M = 1$). The Mach contours in Fig. 4.3a show that this is not the case, and bypass air through the fan duct is overexpanded. There is shock wave is created as air exits the fan exhaust duct. Consequently, the fan duct had to be re-evaluated so that flow is choked.

The key modification to the fan nozzle duct was increasing the size of the outer core. The nacelle cowling geometry was left constant, and the outer-core spline was made to better match the estimated radii at the fan nozzle exit. This led to better grid agreement between the refinement box and the boundary grids. With this second version geometry, the representative engine was simulated at identical flight conditions to yield the mass flow rates shown in Table 4.2 (version 2). Figure 4.3b shows that the flow out of the fan duct is choked as expected. These mass flow values were considered close enough to simulate propulsion/airframe integration effects for an N+3 engine and an SNLF airfoil.



(a) Representative N+3 engine version #1



(b) Representative N+3 engine version #2

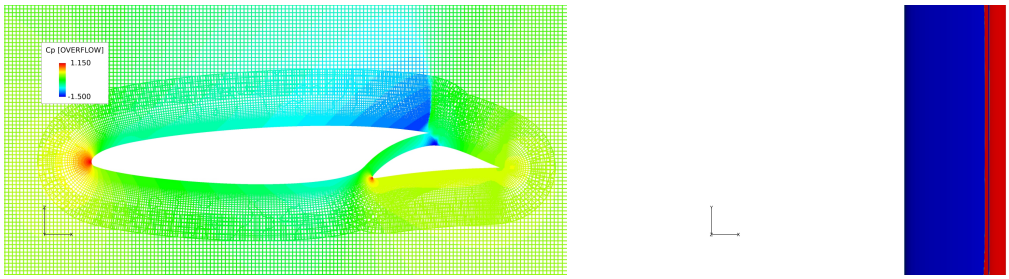
Figure 4.3: Mach number plotted for versions 1 & 2 of the N+3 representative engine OVERFLOW simulations at cruise conditions

4.2 Slotted, Natural-Laminar-Flow Wing

The SNLF airfoil being developed for the TTBW was only very recently; therefore, this researched utilized a previous SNLF design called the S204 [66]. The S204 airfoil was designed for a business-jet application rather than a commercial transport. The key difference between the two is that the commercial transports cruise deep into the transonic regime ($M \approx 0.78$) [40, 63]. Business-jet aircraft such as the HondaJet usually cruise at about $M \approx 0.7$ [9, 34]. The S204 is a 14% thick airfoil designed to cruise at $M = 0.65$ with a drag divergence Mach number greater than $M = 0.75$ at $C_L = 0.25$ [66]. Somers [66] concluded that the S204 showed potential to increase $\frac{L}{D}$ in cruise. Thus, the entire aircraft would become substantially more efficient.

The new SNLF airfoil for the transonic truss-braced wing is termed the S207. This research tried to gain insight in the potential propulsion/airframe interference effects by first investigating the S204 semi-infinite wing. Then the S207 was studied. This thesis then sought commonalities between the two integrations.

As a first look at the influence of a high-bypass ratio turbofan integrated with a slotted, natural-laminar-flow wing, the configuration was simplified. The pylon effects were ignored. The wings were modeled as a semi-infinite, constant chord wing. The S204 and S207 airfoils were extrapolated four engine diameters in the span-wise direction [24]. The engine diameters were take from the SUGAR Phase I report diameter ($D_{fan} = 77in$) [18]. Then the airfoils were extrapolated 2000 inches (25 fan diameters) with a grid stretching ratio of 1.3. In order to mitigate the influence of induced drag, the wings were extrapolated to meet the wall. Then each semi-infinite wing was simulated at specified lift coefficient ($C_L = 0.6$). This lift coefficient is in the low-drag high-lift region determined in the S204 report [66].



(a) Isolated S204 wing pressure distribution

(b) Upper surface turbulence index

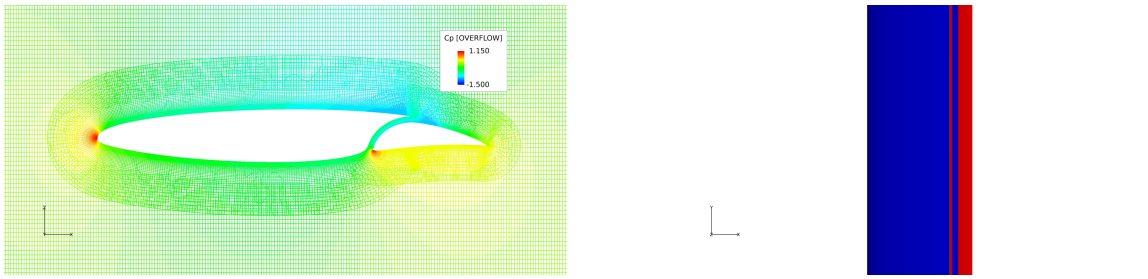
Figure 4.4: Results of isolated S204 semi-infinite wing at $C_L = 0.6$ and $M_\infty = 0.745$

4.2.1 Isolated S204 Semi-infinite Wing

The S204 was simulated at the TTBW cruise conditions listed by Bradley and Droney [18]. The entire S204 semi-infinite wing was integrated with $A_{ref} = 474408$ in^2. Predictions of pressure field and surface transition locations for the isolated S204 semi-infinite wing are shown in Fig. 4.4. It is clear that the S204 is not operating at optimal flight conditions to maximize the lift-to-drag ratio. Somers showed that $M = 0.65$ and $C_l = 0.6$ is likely outside of the S204 drag bucket. Most of the upper surface of the wing is supersonic, and these Mach waves coalesce into a shock wave at the trailing-edge of the fore element. This supersonic flow would make it extremely difficult to install a nacelle directly above the wing because of the nozzle-like effect created. It is evident from Fig. 4.4a that the S204 is strongly aft-loaded. Fig. 4.4b shows the turbulence index [67] plotted on the upper surface of the wing. Blue and red coloring represent laminar and turbulent flow respectively. The transition location agrees well with Somers [66] findings.

4.2.2 Isolated S207 Semi-infinite Wing

The S207 is expected to perform markedly better than the S204. The S207 cruises at a lower speed than the S204 to maximize the lift-to-drag ratio. The S207 semi-infinite wing was simulated at $M = 0.70$. Unlike the S204 study, the reference area was not the total wing area. It was defined as $A_{ref} = 537.626$ in^2. The lift coefficient was held to $C_L = 0.60$ at the wing centerline, not the entire



(a) Isolated S207 wing pressure distribution

(b) Upper surface turbulence index

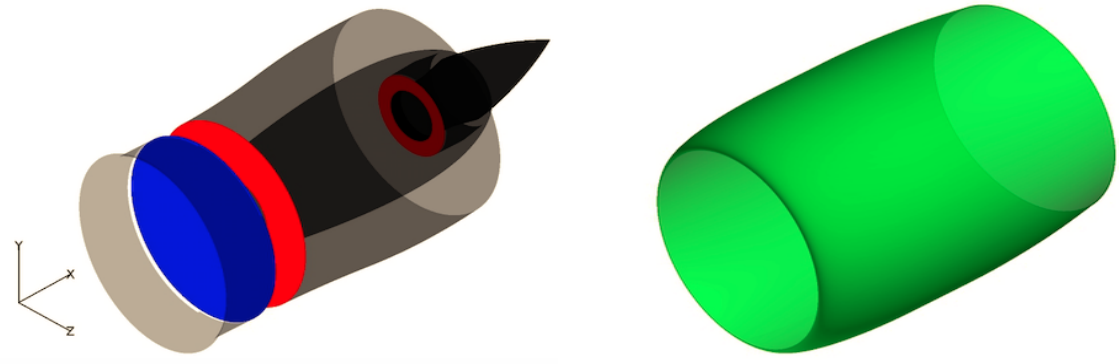
Figure 4.5: Results of isolated S204 semi-infinite wing at $C_L = 0.6$ and $M_\infty = 0.70$

semi-infinite wing. The results are shown in Fig. 4.5. A shock wave is present on the upper surface of the wing; however, this shock is much further aft and weaker compared to the S204. Laminar flow on the wing upper surface is shown in blue in Fig. 4.5b.

4.3 Thrust-Drag Bookkeeping Methodology

In order to account for all engine forces on the powered-on engine, a proper thrust-drag bookkeeping (TDB) methodology was followed [69, 43, 55, 15]. The power accounting method by Drela [29] was not used because of the known difficulty in integrating over overset grid boundaries. The power balance method assumes that the thermal losses of the engine are known and the aircraft is fully trimmed. This is not the case for this research, so conventional bookkeeping schemes were considered.

The thrust domain originally consisted of all forces acting inside of the nacelle. This includes the core, the plug, nozzle exit surfaces, and boundary condition faces. Drag was defined as forces acting outside of the nacelle such as the outer cowling and wing surface. Hooker et al. [43] state that a small region at the lip leading edge of the nacelle should be accounted as drag to capture the stagnation region. The pressure, viscous, and momentum flux forces were then integrated along each surface shown in Fig. 4.6.



(a) Thrust Domain **(b)** Drag domain

Figure 4.6: Proposed thrust-drag bookkeeping surfaces: (Blue) mass-sink; (Red) nozzle inflow; (Black) ducting losses/internal drag; (Green) nacelle drag

Following the procedure used for the Boeing 777 engine integration, the engine would be first characterized statically [15]. In the static case, the engine inlet was be treated as an inviscid adiabatic wall with the nozzles are powered on. This would yield the engine ducting losses or internal drag which are later subtracted from the flight test data. After the engine was characterized statically, the engine was to be characterized at flight conditions. In this way, the ram drag may be accounted as well as the isolated nacelle drag. These forces could later be subtracted when the wing and engine are integrated. The method used by Berry [15] turned out to be unfeasible. The engine model described by Jones and Tong [45] featured a variable area fan nozzle. This meant that the static configuration could not be tested with the engine model previously described, which relies on the flight condition boundary conditions. Ultimately, the engine could not be simulated statically, and ducting losses could not be subtracted from the total nacelle drag.

Instead of simulating the engine statically to measure the ducting losses of the nacelle, the Hooker et al. TDB scheme was used [43]. It is detailed in Fig. 2.9. The pressure, viscosity, and momentum flux across each nacelle and wing surface were integrated. This yielded the isolated nacelle and wing drag. The total interference drag ($\Delta C_{D_{interf}}$), nacelle interference drag ($\Delta C_{D_{nac}}$), and wing interference drag (ΔC_{D_w}) were then calculated for each engine configuration. The sum

of the isolated wing and nacelle will not equal the total drag of the integrated wing and nacelle configuration. The interference drag buildup used Eq. (4.5) below.

$$C_{D_{interf}} = \Delta C_{D_{nac}} + \Delta C_{D_w} \tag{4.5}$$

where

$$\Delta C_{D_{nac}} = C_{D_{nac,iso}} - C_{D_{nac,installed}} \tag{4.6}$$

$$\Delta C_{D_w} = C_{D_{w,iso}} - C_{D_{w,installed}} \tag{4.7}$$

4.4 S204 Semi-Infinite Wing, Flow-Through-Nacelle Study

Before a powered-on engine was simulated, a flow-through (FT) nacelle was positioned around a SNLF semi-infinite wing. This study gave qualitative information on how blockage influenced the laminar flow over the SNLF wing, which was later used in the two propulsion/airframe integration studies. The FT nacelle was created by subtracting the powered nacelle core, core plug, and other powered on grids. It has an approximate fan diameter of 67 inches. No thrust is generated for this flow-through case, but the thrust-drag bookkeeping scheme described above was still used. The isolated engine was simulated at $M = 0.745$ and an altitude of 44,000 feet. The isolated flow-through nacelle is shown in Fig. 4.7. Without the blockage effects of a fan and core geometry, a shock train inside of the nacelle is created. As the flow diffuses out of the nacelle, some of the flow out of the FT nacelle separates due to the shock.

Two parameters were investigated: vertical and horizontal displacement of the engine. These parameters correspond to a change in Z and X respectively. The nacelle coordinates were nondimensionalized by the SNLF wing chord length. The approximate center of the fan face and leading-edge of the wing were located at the origin (0, 0, 0).

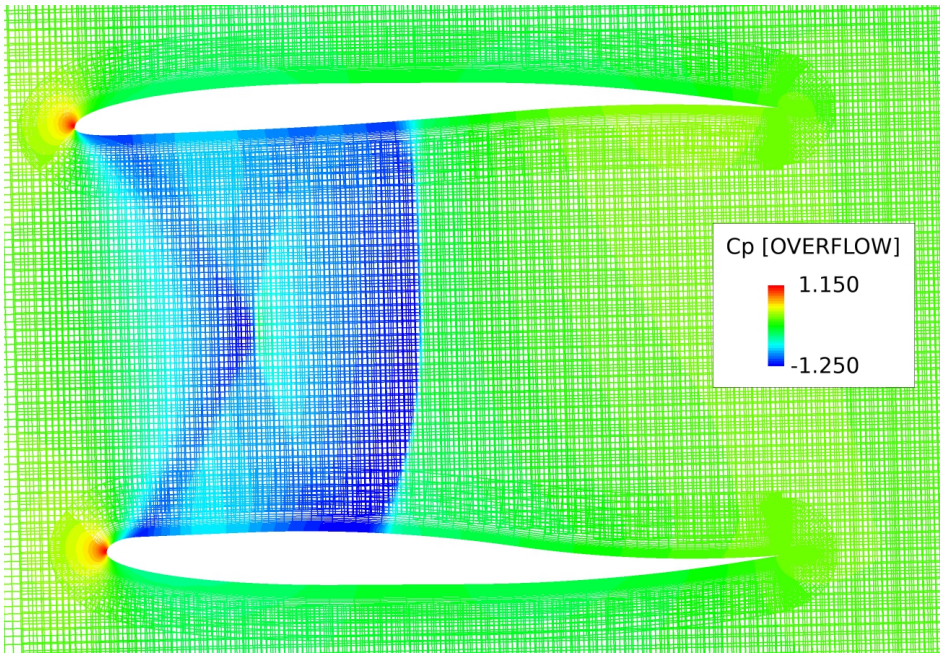


Figure 4.7: C_p plotted for the isolated FT nacelle at flight conditions

Engine locations were determined from previous work described in Chapter 2. The leading-edge OWN and wing-aft-mounted nacelle were not possible because the nacelle could not be mounted to the wing [40, 37]. Although these exact configurations were not studied, this research investigated engine locations located at the trailing-edge and leading-edge. This study did not follow previous studies where internal drag was bookkept separately [63].

The trailing-edge/over-wing nacelle results are plotted in Fig. 4.8a. This configuration was followed the position guidelines determined by Fujino and Kawamura [35]. This configuration created more interference drag than the traditional under-wing nacelle (Table 4.3). The outer nacelle increases the upper surface pressure of the S204 wing; thus, the strength of the shock wave was reduced. This did not lead to a favorable effect. The turbulence model index in Fig. 4.8a shows that the OWN cause an early transition to turbulent flow over the wing. This transition occurs much earlier than the isolated wing displayed in Fig. 4.4b.

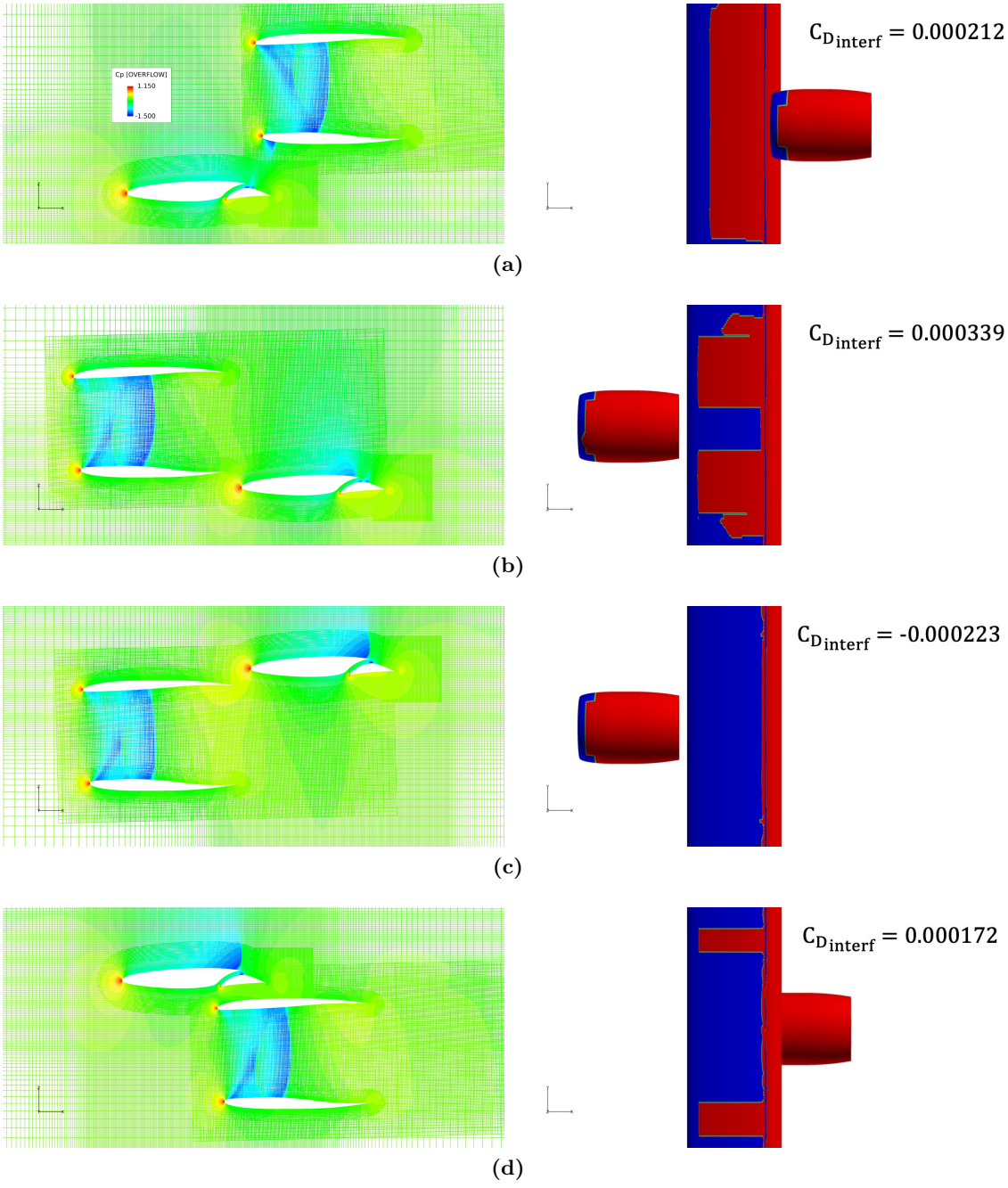


Figure 4.8: Results of S204 wing and FT nacelle integration

Table 4.3: Drag buildup of flow-through nacelle study with S204 wing

$C_{D_{nac}}$		0.001006	
$C_{D_{S204}}$		0.016677	
Positon	$\Delta C_{D_{nac}}$	ΔC_{D_w}	$C_{D_{interf}}$
TE OWN	–0.000841	0.001053	0.000212
LE OWN	0.000398	-0.000059	0.000339
LE UWN	-0.000375	0.000152	-0.000223
TE UWN	-0.000139	0.000311	0.000172

The leading-edge OWN was placed so that the outer cowling was not directly above the wing. This prevented any shock waves from forming on the upper surface of the wing. The interference drag is higher than the both under-wing configurations. Once again, laminar flow over the wing is strongly influenced by the presence of the FT nacelle (Fig. 4.8b). The wing upper surface directly behind the nacelle is laminar; however, the flow transitions close to the leading-edge on either side of the nacelle.

The conventional under-wing nacelle had favorable interference drag even due to large amounts of laminar flow over the suction surface of the wing and no strong shocks. The trailing-edge/under-wing position cause transition earlier on both sides of the nacelle while the leading-edge nacelle had almost no effect on upper surface laminar flow. These results show that nacelle position largely influences the laminar flow over a SNLF wing. Stronger shocks tended to cause early separation, and more interference drag.

4.5 S204 Semi-infinite Wing, Powered-on-Nacelle Study

The powered-on UBPR engine was placed in identical locations as the FT nacelle for the first case. Then a few modifications were made to determine the impact of shifting the nacelle vertically and/or horizontally. The mass flow out of the engine and wing lift coefficient were held constant. Flow field pressure coefficients and surface turbulence index are plotted for each configuration. Interference drag was calculated for each case and listed in Table 4.4. Although the S204 wing was

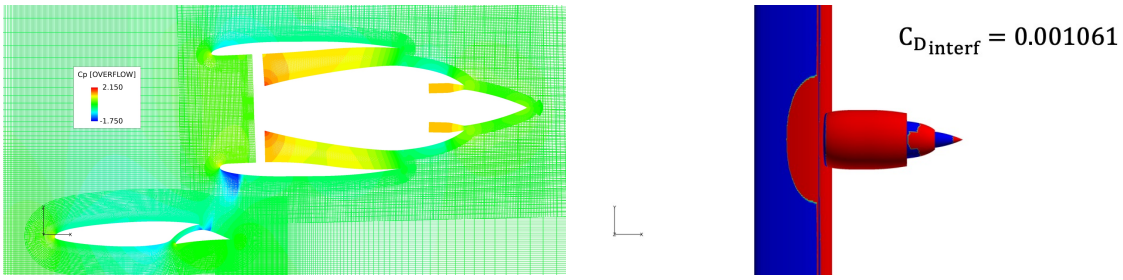
Table 4.4: Drag buildup of powered-on nacelle with S204 wing

$C_{D_{nac}}$	-0.004223			
$C_{D_{S204}}$	0.016677			
	$\Delta C_{D_{nac}}$	ΔC_{D_w}	$C_{D_{interf}}$	$(\frac{\Delta x}{c}, \frac{\Delta z}{c})$
TE OWN				
1	-0.000928	0.001989	0.001061	(1.14, 073)
2	-0.000932	0.001822	0.000890	(1,14, 0.82)
3	-0.000354	0.000952	0.000598	(1.32, 0.73)
LE OWN				
1	0.002323	-0.001678	0.000645	(-0.91, 0.45)
2	0.001607	-0.000809	0.000798	(-1.00, 0.55)
3	0.000779	0.000194	0.000973	(-1.14, 0.45)
LE UWN				
1	0.000325	0.000067	0.000392	(-0.91, -0.45)
2	0.000108	0.000254	0.000362	(-1.00, -0.45)
3	0.000355	0.000196	0.000551	(-0.91, -0.55)
TE UWN				
1	-0.000143	0.001959	0.001816	(0.91, -0.50)
2	0.000707	-0.000003	0.000704	(1.32, -0.55)
3	0.000429	0.000401	0.000830	(1.14, -0.50)

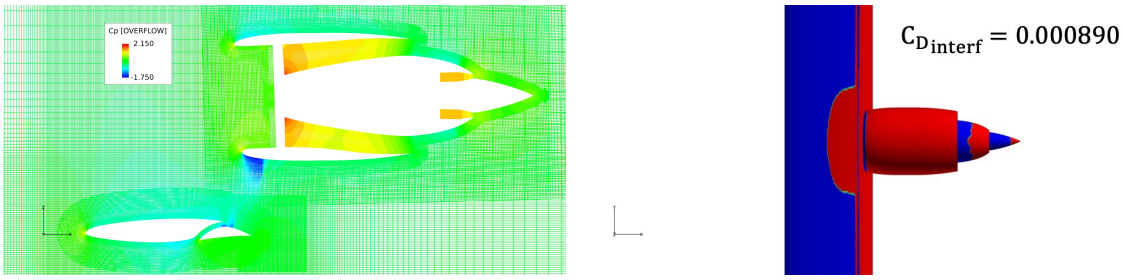
likely operating outside of the drag bucket, this study was a first step in simulating the S207 wing. Interference effects of the S204 at TTBW cruise conditions were still relevant while the S207 design was finalized.

4.5.1 Trailing-edge/Over-wing

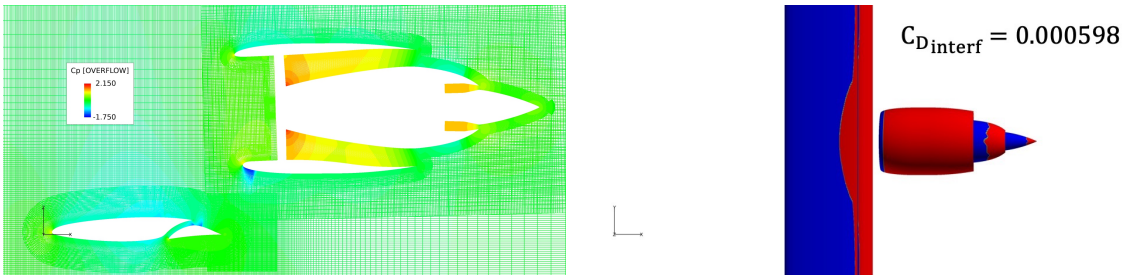
The trailing-edge/over-wing study followed the rough position guidelines given by Fujino and Kawamura [35]. The positions are shown in Table 4.4. Like the flow-through study, this engine position still had a larger total interference drag than the conventional UWN. The high-pressure region caused by the engine inlet led to higher pressure on the wing suction surface (Fig. 4.9a). The engine position was located further upstream for case 1, which performed poorly. Case 1 created a strong shock over the wing upper surface, and the pressure distribution was severely disturbed compared to cases where the engine was shifted downstream. It was determined that shifting the



(a) Case 1



(b) Case 2



(c) Case 3

Figure 4.9: Trailing-edge over-wing-nacelle congifuration (left) pressure coefficient (right) upper surface turbulence index

nacelle downstream so that the nacelle did not cause the flow to accelerate over the wing decreased interference drag. This result agrees well with previous work [16, 35, 43].

Fig. 4.9a shows that the nacelle interference causes an early transition from laminar to turbulent flow. Case 2 positioned the nacelle higher and further away from the wing. It was intended to alleviate high pressure region acting on the wing upper surface; however, the upward movement did not have a significant impact. The third case positioned the representative gFan+ engine further downstream at the same vertical distance as Case 1 for the same reason. This showed the potential

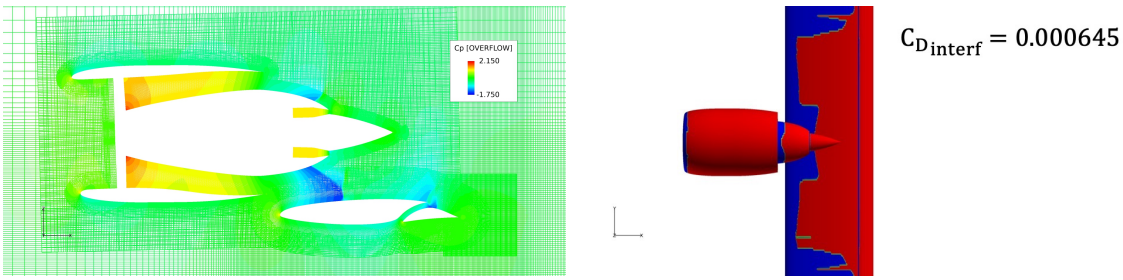
for more improvement. Shifting the nacelle 0.18 chord lengths downstream reduced $C_{D_{interf}}$ by 5 cts.

4.5.2 Leading-Edge/Over-Wing

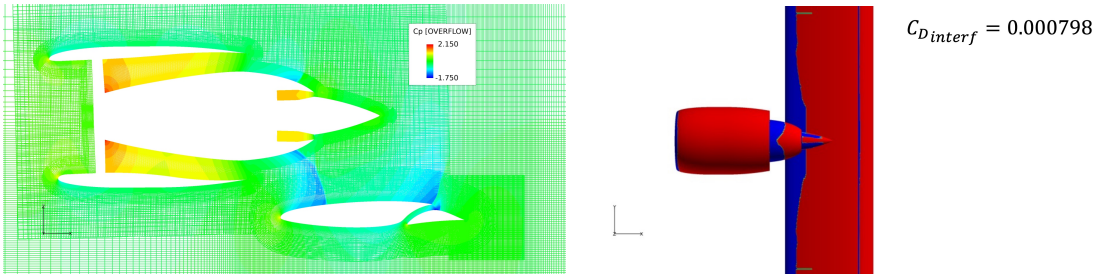
The leading-edge/over-wing nacelle location was investigated with three engine locations. The first location was placed in the same location as the flow-through nacelle. This was believed to be a candidate location for favorable interference effects based on the FT study. While the engine cowling itself did not create a shock, the core exit surface and the wing create a strong shock wave near the leading-edge of the S204 wing. This low-pressure region caused by the accelerated flow acts on the forward facing surface of the wing. The resulting C_{D_w} was negative 17 drag cts. This shock had a favorable effect on interference drag compared to the other LE OWN positions. Much like the OWN design discussed in chapter 2, the low-pressure region acted on the forward facing surface and counteracted drag [40]. The second case positioned the engine upstream and upward. This was intended to reduce the nozzle-like phenomenon between the wing and core. Fig. 4.10c shows that the flow did not accelerate as much as Case 1. This is due to the nacelle being moved further away from the wing. Unfortunately, reducing the nozzle effect did not result in a more favorable interference drag (Table 4.4). While Case 1 performed the best out of the three positions, the drag penalty created by the LE OWN was much higher than the conventional UWN. Hooker et al. [43] determined the same result at a higher Mach number ($M = 0.80$). Previous research found that LE OWN are not beneficial for supercritical wings below $M = 0.78$ [46, 40].

4.5.3 Leading-Edge/Under-Wing

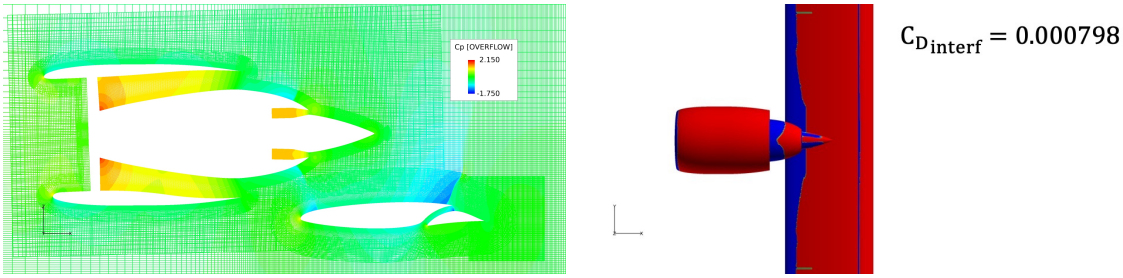
The leading-edge/under-wing position was located in the conventional nacelle location relative to the wing. This was achieved with Fig. 2.3 in Chapter 2. The flow-through analysis showed that



(a) Case 1



(b) Case 2



(c) Case 3

Figure 4.10: Leading-edge/over-wing configuration (left) pressure coefficient (right) lower surface turbulence index

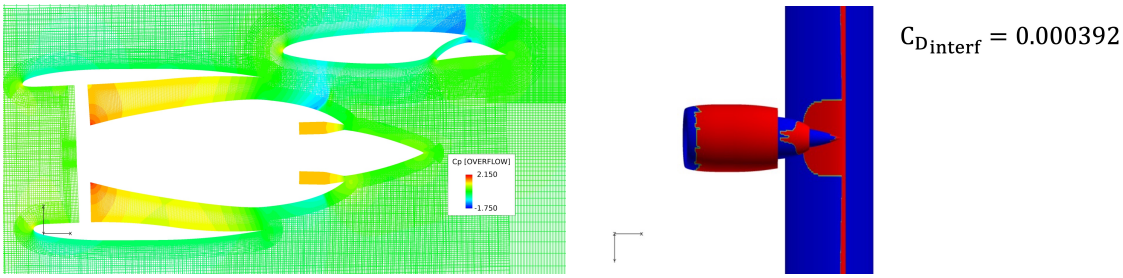
the under-wing position would be beneficial at $M = 0.745$, and the powered-on results agree. Table 4.4 shows that compared to the OWN positions, the conventional location has less interference drag. Like previous UWN pressure distribution on the wing upper surface is not disturbed by the presence of the nacelle [43].

Laminar flow on the suction side of the wing is unaffected by the presence of the nacelle. The lower side of the wing transitions to turbulent flow due to the close proximity of the engine to the wing. Fig. 4.11c shows that the upstream movement of the engine (Case 2) induced more turbulent flow below the wing. The upstream movement reduced $C_{D_{interf}}$. Increasing Δz (Case 3) with a constant Δx did not reduce $C_{D_{interf}}$. This result agreed well with previous research [49, 64, 39]. Lange [49] stated that shifting the nacelle horizontally created superimposing effects between the wing and engine. This is evident from Table 4.4.

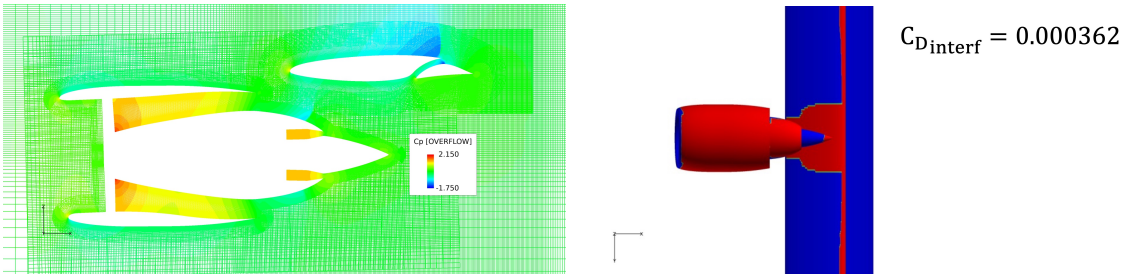
4.5.4 Trailing-Edge/Under-Wing

The flow-through and powered simulation both show that this location is not straightforward. In Case 1, the close proximity between the S204 aft element and the outer cowling causes the flow to prematurely separate from the aft element. High pressure at the start of the slot to the presence of the nacelle caused the flow to accelerate to the suction side of the wing. This is evident from Fig. 4.12. A shock resulted, and the flow separated. The result is an excessively high ΔC_{D_w}.

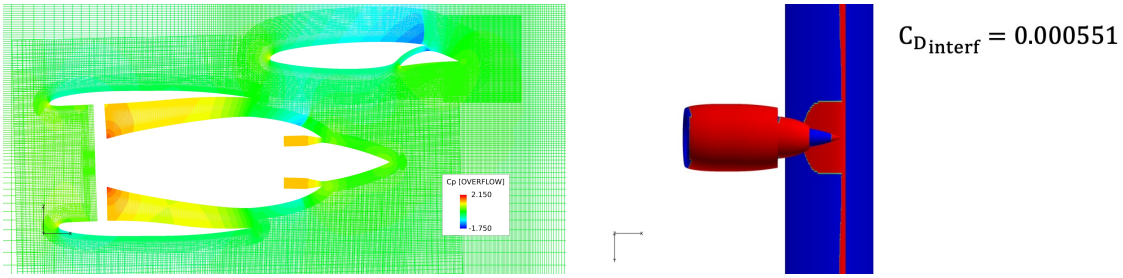
Shifting the representative N+3 engine downstream and down away from the aft element alleviated the adverse pressure gradient on the aft element upper surface (Case 2). Case 3 positioned the engine with a smaller Δx as Case 2 and an identical Δz as in Case 1. This downstream shift led to a large reduction in $C_{D_{interf}}$ of about 10 cts. The high pressure region due to the decelerated flow at the inlet caused a local increased in lift. This phenomenon was noted in previous literature as a benefit to the TE UWN position [39, 37]. Placing the engine in this location may not solve



(a) Case #1

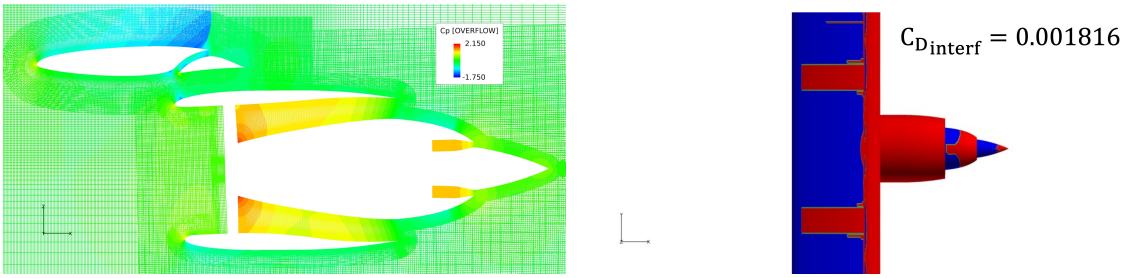


(b) Case #2

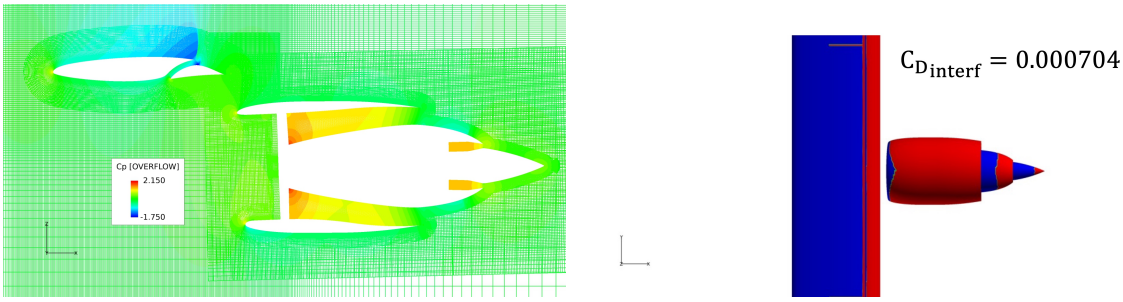


(c) Case #3

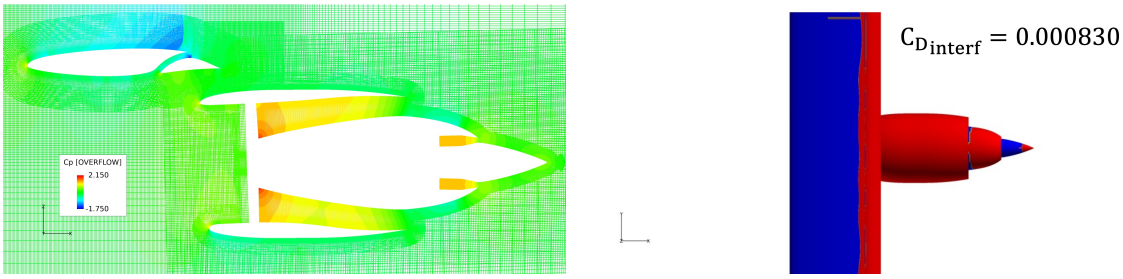
Figure 4.11: Leading-edge/under-wing configuration (left) pressure coefficient (right) lower surface turbulence index



(a) Case 1



(b) Case 2

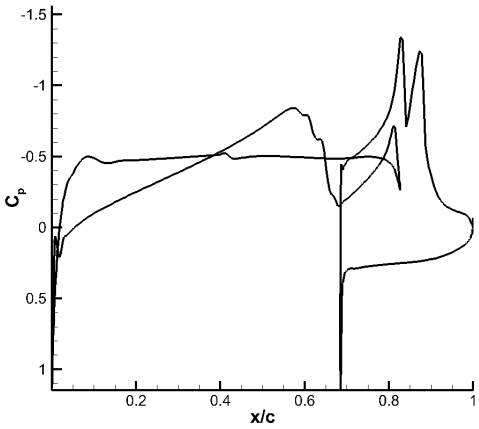


(c) Case 3

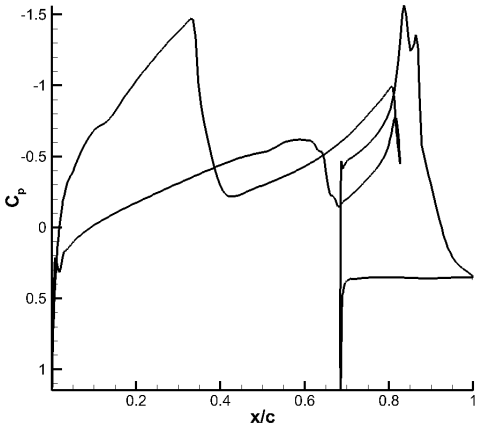
Figure 4.12: Trailing-edge/under-wing configuration (left) pressure coefficient (right) upper surface turbulence index

any of the current issues associated with under-wing nacelles such as ground clearance, noise, or debris intake [40, 46, 64]. The large improvement from position to position, however, showed that more positions should be investigated before the TE UWN concept was discarded.

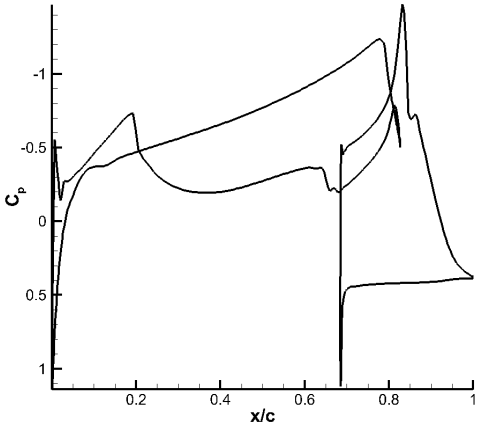
The surface pressure distributions at the Y = 0 shed some light into why transition to turbulent flow occurs. These are plotted for the first case in Fig. 4.13. A favorable pressure gradient will encourage the flow to remain laminar, which reduces skin friction drag. Turbulent flows are sometimes less prone to separation in an adverse gradient, especially when the turbulent boundary layer is young [74].



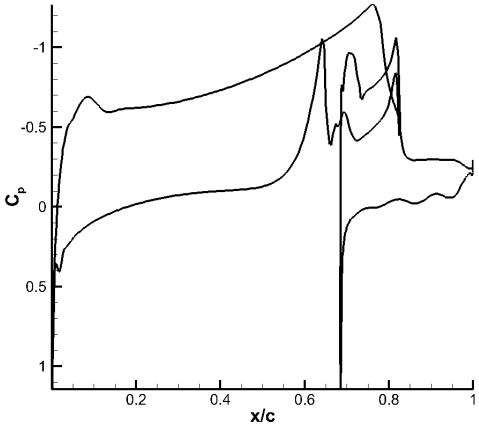
(a) TE/OWN configuration



(b) LE/OWN configuration



(c) LE/UWN configuration



(d) TE/UWN configuration

Figure 4.13: S204 surface pressure distribution for Case 1 at Y = 0

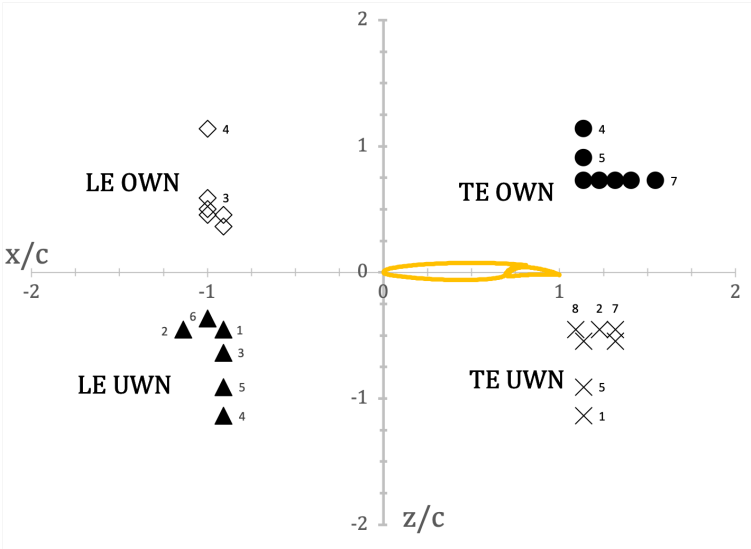


Figure 4.14: Engine fan face location relative to the S207 semi-infinite wing for each simulation (drawing not to scale)

The over-wing nacelles cause the flow to transition early on the wing suction side. The trailing-edge OWN transitioned before 50% chord because of the almost zero pressure gradient on the upper surface. The leading-edge OWN transitioned almost immediately because of the shock. Fig. 4.13 shows that the flow separates and reattaches. The leading-edge UWN has a favorable pressure gradient on the suction side, but a shock induces early transition on the lower side. The TE UWN has a favorable pressure along the fore element surface. The aft element separates at the slot exit due to the lower pressure at the aft element trailing-edge. This low-pressure region induces an unfavorable gradient where the flow does not reattach, but separates completely.

4.6 S207 Semi-Infinite Wing Powered-on-Nacelle Study

The S207 propulsion integration study was performed at the S207 flight conditions. The engine mass flow was adjusted to match the thrust requirements of the gFan+ at $M = 0.70$. Previous literature tested engine configuration deeper into the transonic regime [49, 16, 63, 37, 43]. Flight Mach numbers were above $M = 0.75$. Then it was characterized in isolation at S207 flight conditions. In

this study, the lift coefficient was kept constant at $C_L = 0.6$ at the wing centerline. The interference drag is shown in Table 4.5. Because the lift and drag were calculated at the wing centerline, the resulting interference drag is extremely pronounced. The wing reference area and chord length were identical to the isolated S207 semi-infinite wing. The center of the fan locations are depicted in Fig. 4.14.

4.6.1 Trailing-Edge/Over-Wing

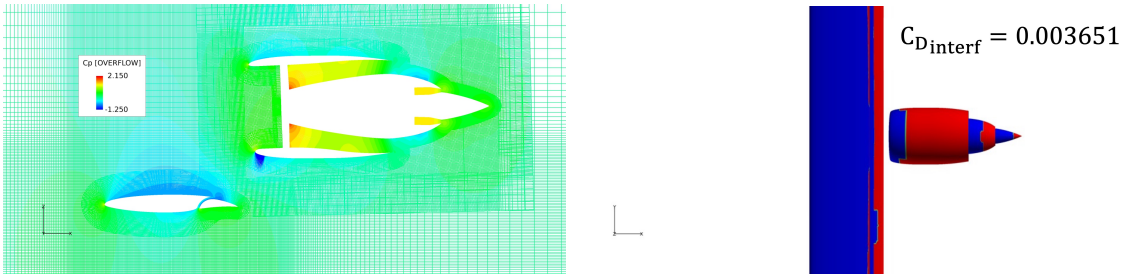
The over-wing trailing-edge location kept the same vertical height in Cases 1, 2, and 3. It was the intention for the nacelle to be shifted upstream far enough so that the nacelle inlet would align with the upper wing shock [35]. Cases 4 and 5 moved the engine upward to setup a favorable pressure gradient on the wing upper surface. Moving the engine upward did not significantly decrease $C_{D_{interf}}$, and this is shown in Table 4.5. Case 1, created 36 drag cts due to interference effects. Cases 2 and 3 results suggested that the minimum $C_{D_{interf}}$ was further downstream. Case 6 moved the engine to 1.41 chord lengths downstream while the $\frac{\Delta z}{c} = 0.73$. This was the same upward distance as Cases 1-3. The resulting $C_{D_{interf}}$ was less than 13 cts. Moving the engine downstream from the wing had a very favorable interference effect. The drag due to interference was halved between Case 1 and Case 6. Case 7 shifted the nacelle even further downstream than Case 6. The result was a negative interference drag. This confirmed the results by Fujino and Kawamura [35].

The turbulence index for the wing upper surface of Case 1 is plotted in Fig. 4.15a. The wing upper surface is entirely laminar. As the engine was moved upstream for Cases 2 and 3, the engine caused the flow to transition earlier. Case 6 shows similar behavior to Cases 2 and 3. Cases 4 and 5 are positioned the furthest above the wing. They setup laminar flow over the wing; however, these positions are not far enough downstream to avoid creating a nozzle-like effect between the wing and cowling. These positions create excessive interference drag. It is possible that moving the

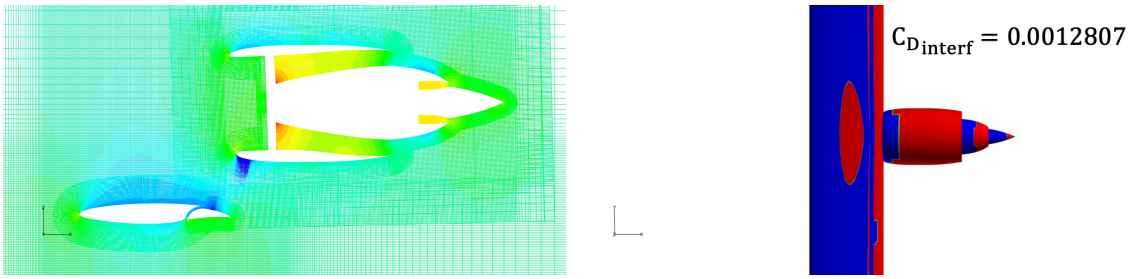
Table 4.5: Drag buildup of powered-on nacelle with S207 wing

$C_{D_{nac}}$	-0.004614			
$C_{D_{S204}}$	0.005869			
	$\Delta C_{D_{nac}}$	ΔC_{D_w}	$C_{D_{interf}}$	$(\frac{\Delta x}{c}, \frac{\Delta z}{c})$
TE OWN				
1	-0.000777	0.004428	0.003651	(1.32, 0.73)
2	-0.001054	0.013861	0.012807	(1.23, 0.73)
3	-0.001365	0.029648	0.028283	(1.14, 0.73)
4	-0.000951	0.012948	0.011997	(1.14, 1.14)
5	-0.001199	0.023102	0.021903	(1.14, 0.91)
6	-0.000587	0.001869	0.001282	(1.41, 0.73)
7	-0.000402	-0.000978	-0.001380	(1.55, 0.73)
LE OWN				
1	0.001739	-0.013016	-0.011277	(-0.91, 0.45)
2	0.001142	-0.011332	-0.010190	(-1.00, 0.50)
3	0.001033	-0.011290	-0.010257	(-1.00, 0.59)
4	0.000649	-0.008643	-0.007994	(-1.00, 1.14)
5	0.001229	-0.009904	-0.008675	(-1.00, 0.45)
6	0.002401	0.000928	0.003329	(-0.91, 0.36)
LE UWN				
1	0.000140	-0.013490	-0.013350	(-0.91, -0.45)
2	-0.000182	0.002511	0.002329	(-1.14, -0.45)
3	0.000033	-0.006596	-0.006563	(-0.91, -0.64)
4	-0.000111	-0.002194	-0.002305	(-0.91, -1.14)
5	-0.000089	-0.003620	-0.003709	(-0.91, -0.91)
6	0.000078	-0.011916	-0.011838	(-1.00, -0.36)
TE UWN				
1	0.000068	0.000898	-0.000830	(1.14, -1.14)
2	0.000685	-0.022724	-0.022039	(1.23, -0.45)
3	0.000571	-0.016204	-0.015633	(1.14, -0.55)
4	0.000465	-0.015720	-0.015255	(1.32, -0.55)
5	0.000139	-0.003210	-0.003071	(1.14, -0.91)
6	0.000575	-0.020662	-0.020087	(1.32, -0.45)
7	0.000793	-0.025219	-0.024426	(1.09, -0.45)
8	0.000172	-0.002767	-0.002595	(0.91, -0.45)

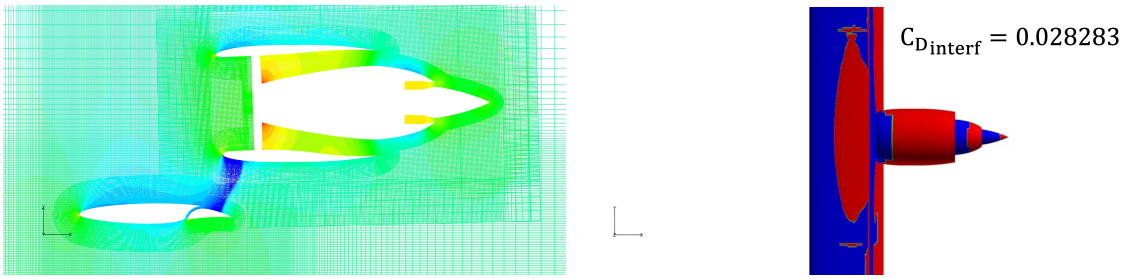
engine further downstream would reduce interference drag by mitigating the low-pressure region on the aft portion of the wing. This is evident from Cases 1, 2, 3, and 6 where the engine was shifted downstream. Installing the engine too far downstream of the wing could exacerbate structural problems or increase the weight of the pylon. It is evident from the unsteadiness of the surface pressure coefficients in Fig. 4.17 that a few cases had minor convergence issues.



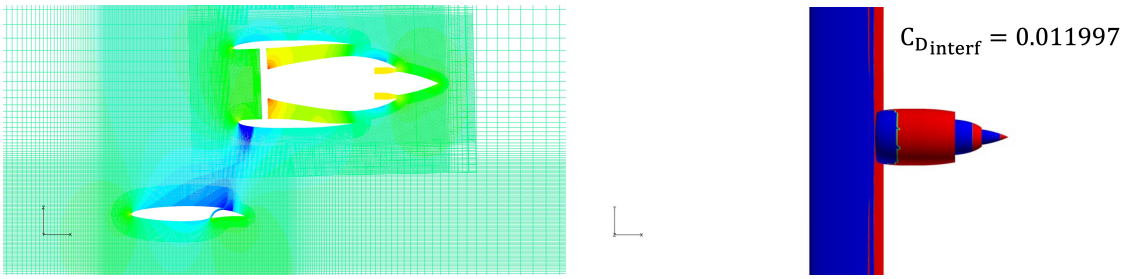
(a) Case 1



(b) Case 2

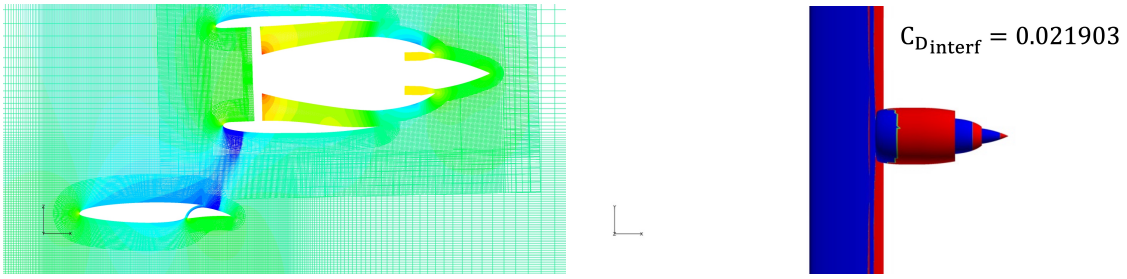


(c) Case 3

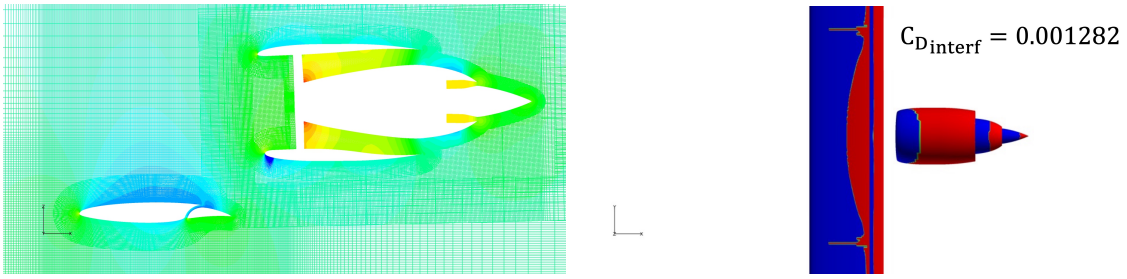


(d) Case 4

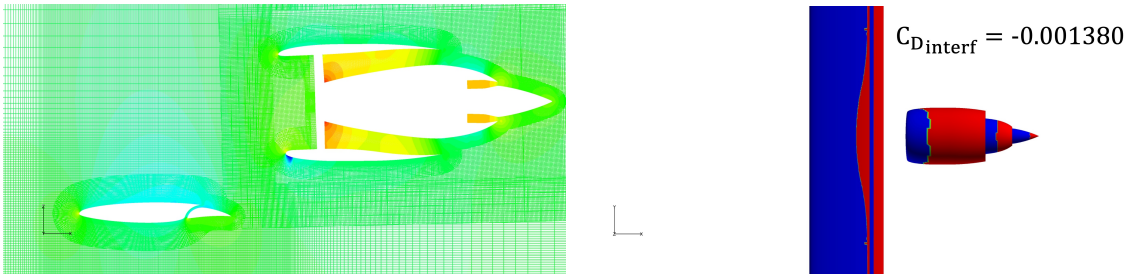
Figure 4.15: TE OWN Cases 1-4 (left) pressure contours (right) upper surface turbulence index



(a) Case 5

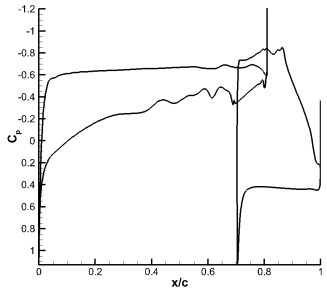


(b) Case 6

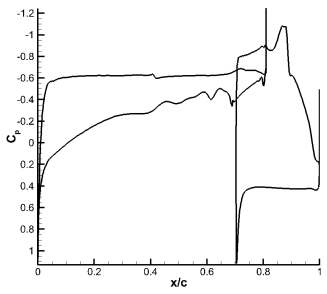


(c) Case 7

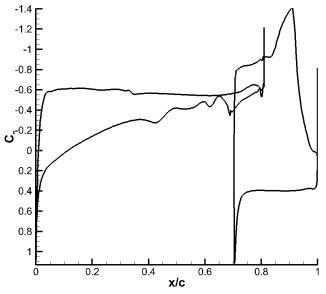
Figure 4.16: TE OWN Cases 5-7 (left) pressure contours (right) upper surface turbulence index



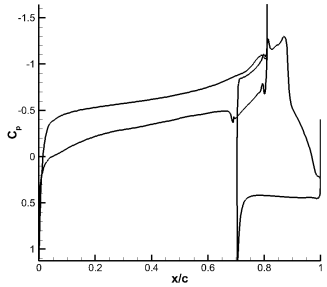
(a) Case 1



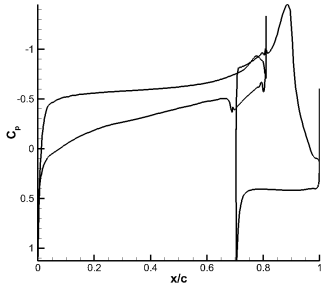
(b) Case 2



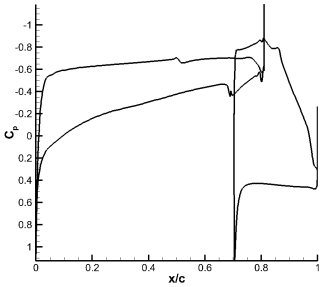
(c) Case 3



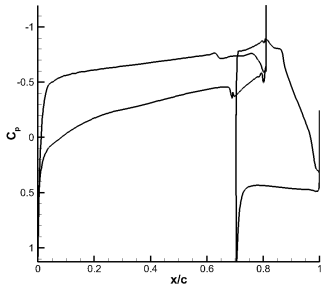
(d) Case 4



(e) Case 5



(f) Case 6



(g) Case 7

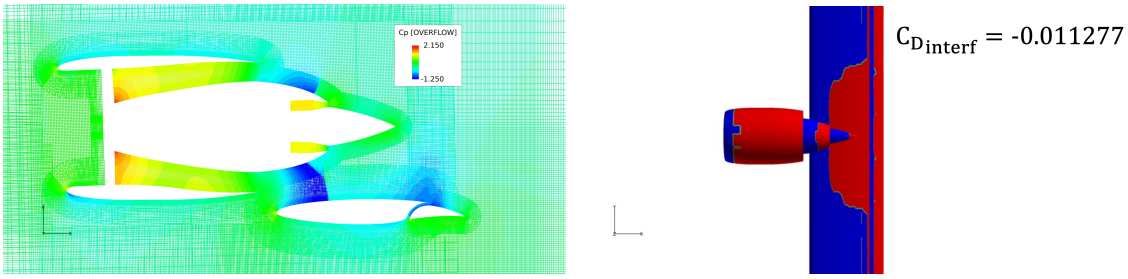
Figure 4.17: S207 surface pressure distribution at Y = 0 for TE OWN configuration

4.6.2 Leading-Edge/Over-Wing

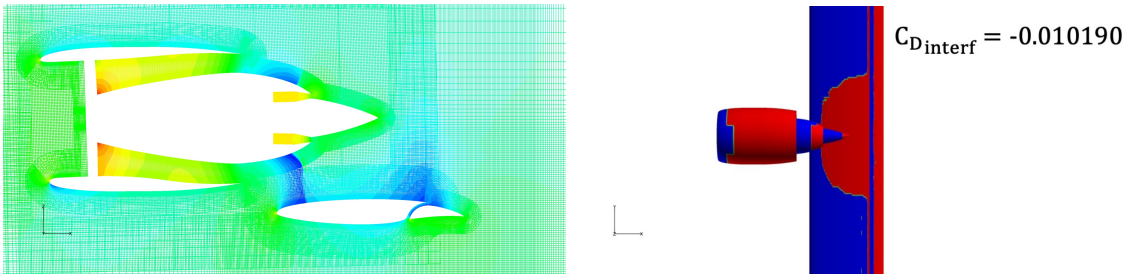
The LE OWN configuration was studied using the engine locations listed in Table 4.5. The results show that the nacelle accounts for most of the total drag when located in the LE OWN position. Cases 1, 2, 3, and 6 created a shock near the leading-edge of the wing. This is shown in Fig. 4.18, Fig. 4.19, and Fig. 4.20. Unlike the S204, the shock creates negative ΔC_{D_w}. This is likely due to a weaker shock; and, a smaller drag penalty. All of these cases except Case 6 result in negative ΔC_{D_w}. The low-pressure region acted on the forward facing surface of the wing; thus, reducing wing drag. Hill et al. [40] stated how leading-edge shocks can be exploited since the boundary layer is young. The flow stays attached even with a strong shock wave at the leading-edge. The location nearest the wing, Case 6, did not perform better than Case 1. In Case 6, accelerated flow out of the fan nozzle exhaust created a strong shock near the wing leading-edge.

The shock in Case 1 is weaker than Case 6; therefore, it created a favorable interference effect. Case 1 performed slightly better than Cases 2 and 3. Cases 1, 2, and 3 moved the engine upward with a constant Δx. The resulting interference drag was negative, but in Cases 2 and 3 $C_{D_{interf}}$ was about 1 count higher than Case 1. Case 5 shifted the nacelle upstream from the Case 1 position, but this did not result in a lower $C_{D_{interf}}$. The low-pressure region formed on the wing was reduced in Case 5. This is shown upon close inspection of Figs. 4.20a and 4.20e.

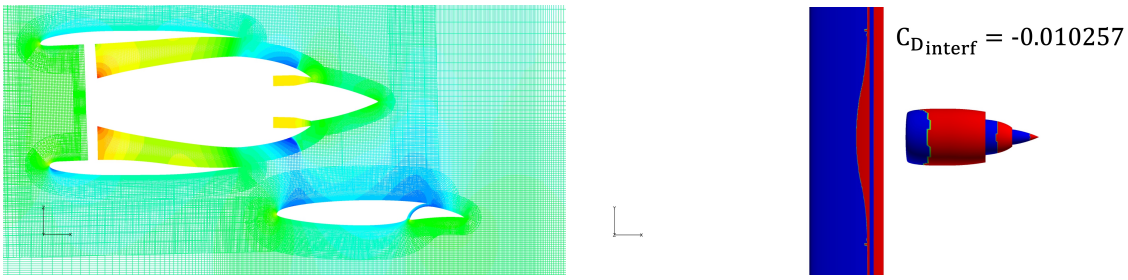
Laminar flow under the wing was not influenced by the leading-edge OWN. The turbulence index is plotted in Fig. 4.18 and Fig. 4.19. It is evident that placing the engine vertically closer to the wing (Cases 1, 5, and 6) led to early transition on the wing upper surface. The shocks are visible from Fig. 4.20. After the shock the pressure gradient is adverse, this is not suitable for laminar flow. While not shown, the close coupling of Case 6 caused the wing pressure side to prematurely transition to turbulent flow. This is most likely due to the turbulent wake from the cowling.



(a) Case 1

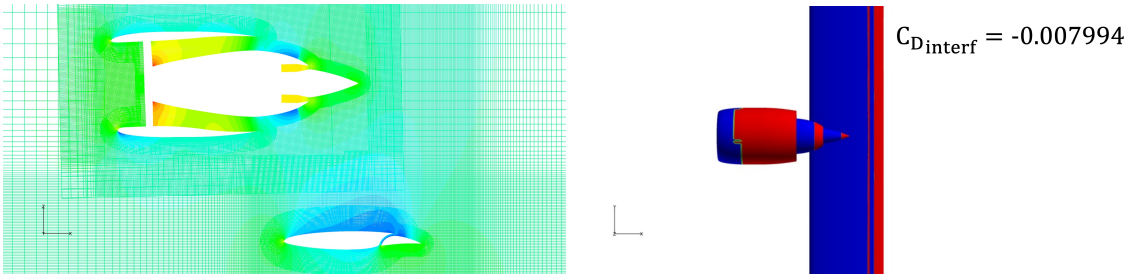


(b) Case 2

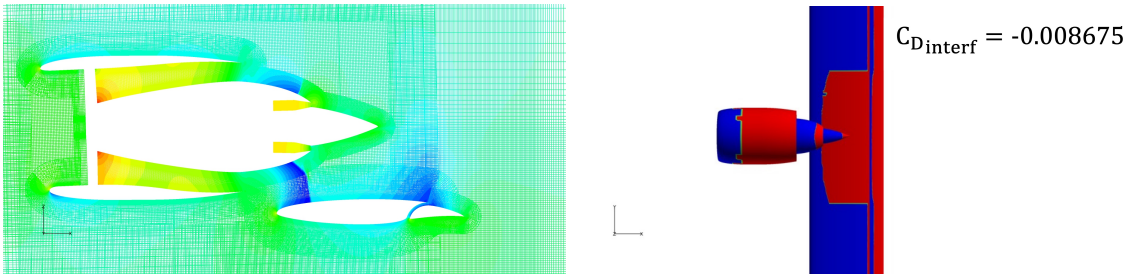


(c) Case 3

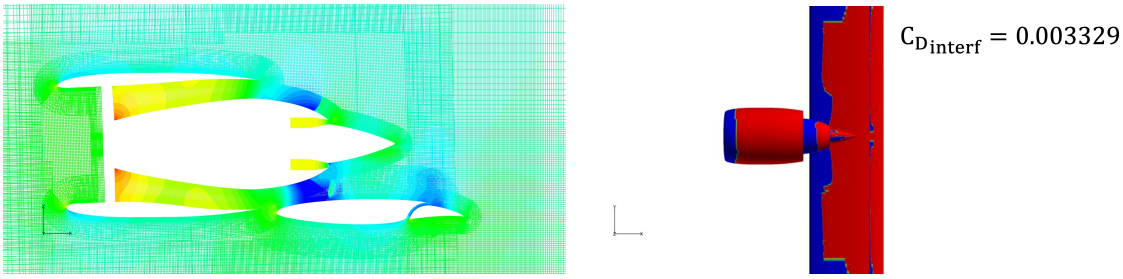
Figure 4.18: LE OWN Cases 1-3 (left) pressure contours (right) upper surface turbulence index



(a) Case 4

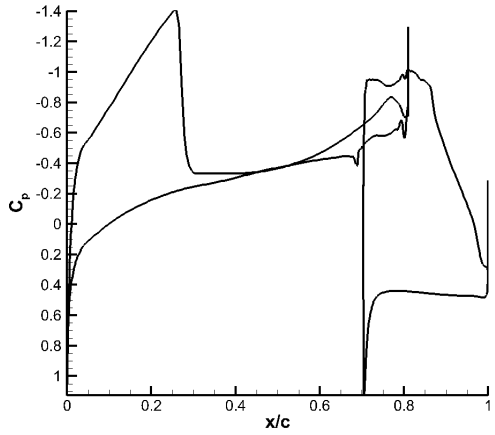


(b) Case 5

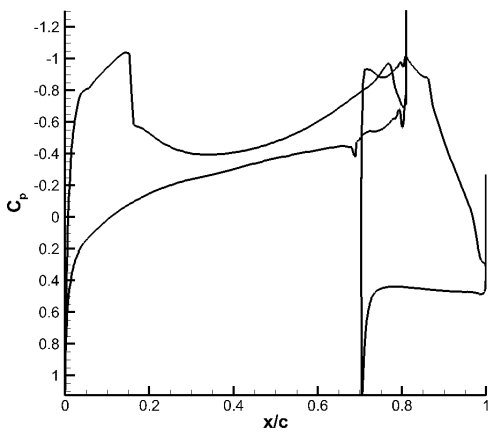


(c) Case 6

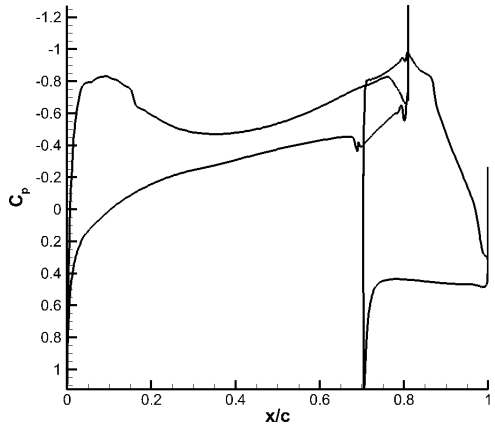
Figure 4.19: LE OWN Cases 5-6 (left) pressure contours (right) upper surface turbulence index



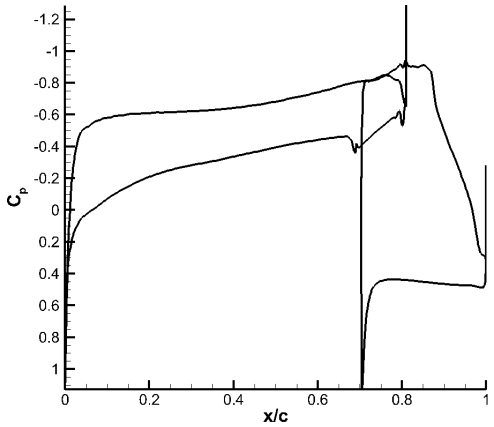
(a) Case 1



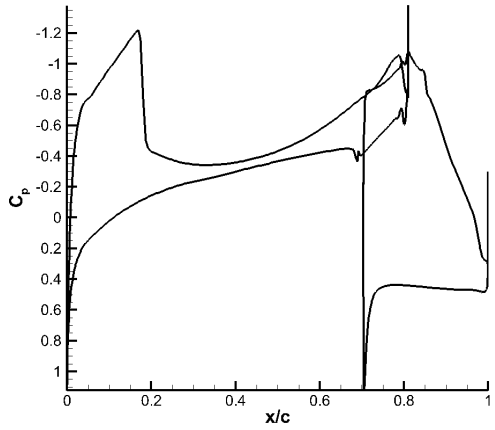
(b) Case 2



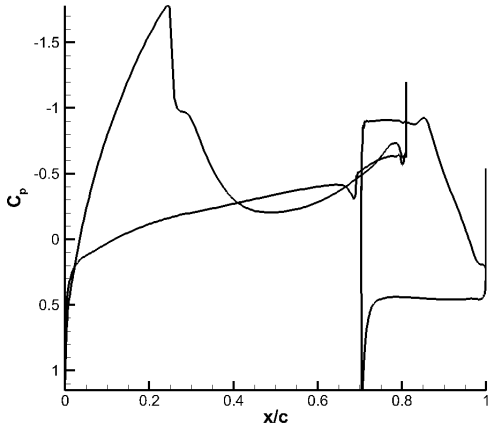
(c) Case 3



(d) Case 4



(e) Case 5



(f) Case 6

Figure 4.20: S207 surface pressure distribution at Y = 0 for LE OWN configuration

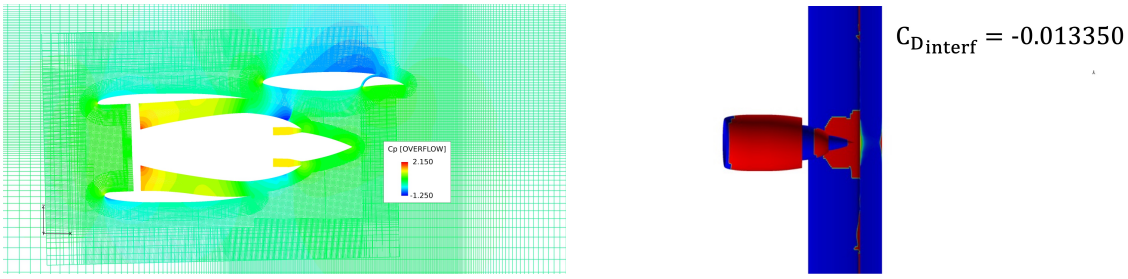
4.6.3 Leading-Edge/Under-Wing

LE UWN positions were largely affected by the change in Δz. Case 1 resulted in the lowest amount of interference drag. Cases 3 and 4 moved the engine downward with Δx equal to Case 1. As the engine was shifted downward with a constant Δx, the interference drag grew. Previous research stated that a vertical shift did not influence interference drag [65, 64]. These papers do not mention how far of a vertical shift was simulated, and previous research simulated flight conditions of $M = 0.75$ and higher [68, 49, 43]. It is not clear whether or not these results contradict previous findings.

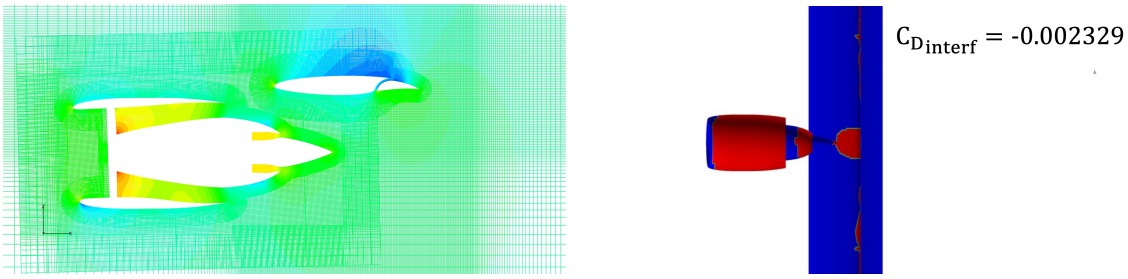
The close coupling between the wing and nacelle core resulted in a strong shock and low-pressure region on the wing. This is shown in Fig. 4.21a. Henderson and Patterson [39] also determined this somewhat close coupling to be beneficial. Case 6 moved the engine closer to the wing by decreasing Δz. This position did not improve upon the interference drag found for Case 1. A suction peak on the lower surface of the wing is visible in Fig. 4.23f. This is due to interaction of the fan exhaust interacting with the wing.

As the nacelle was moved downward, the low-pressure region remained, but the nozzle effect between the engine and wing was less pronounced. Case 2 moved the engine upstream with the same vertical displacement as Case 1. This did not equate to a decrease in interference drag. Instead, $C_{D_{interf}}$ increased by 156 drag counts. It is likely that the superimposing effects noted by Lange [49] do not exist with the nacelle this far upstream.

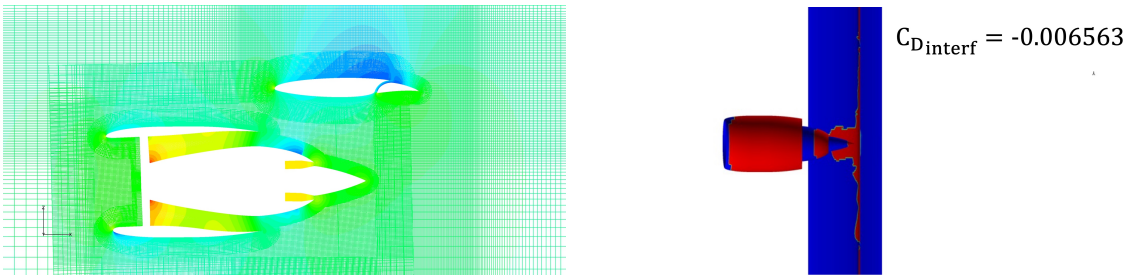
This configuration did not influence laminar flow on the upper surface of the wing, but the lower surface turbulence index is plotted in Figs. 4.21 and 4.22. It is clear that more closely coupling (reducing Δz) the engine and wing reduced the amount of laminar flow under the wing. Turbulent flow under the wing was limited areas directly aft of the engine. As the distance between the outer core and wing was increased, transition was delayed.



(a) Case 1

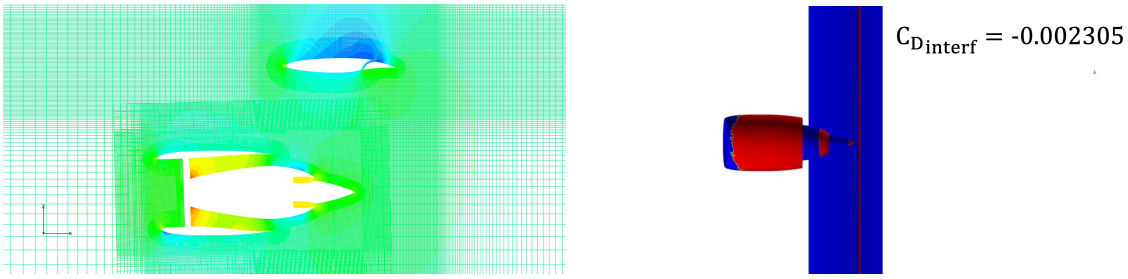


(b) Case 2

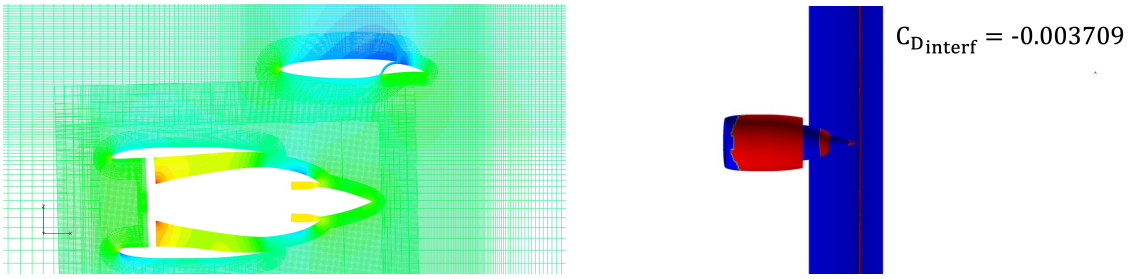


(c) Case 3

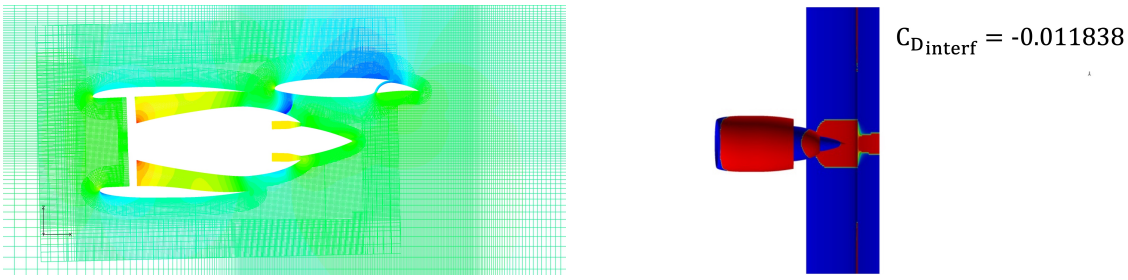
Figure 4.21: LE UWN Cases 1-4 (left) pressure contours (right) lower surface turbulence index



(a) Case 4

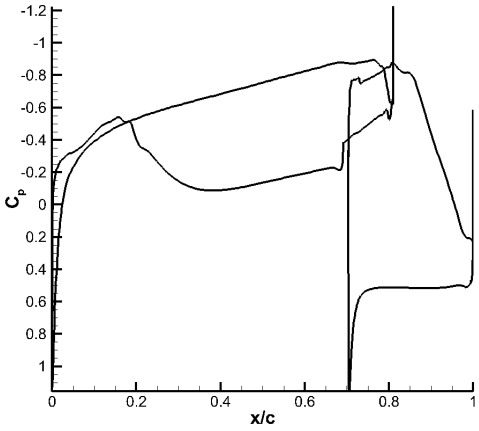


(b) Case 5

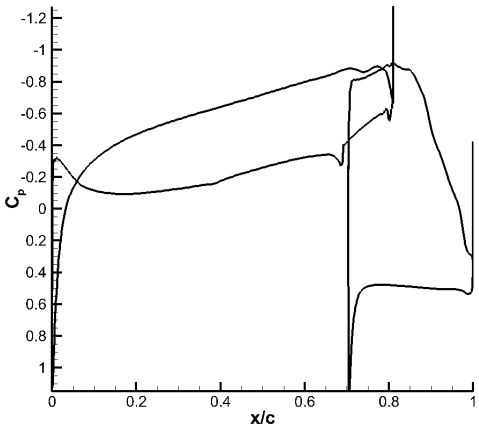


(c) Case 6

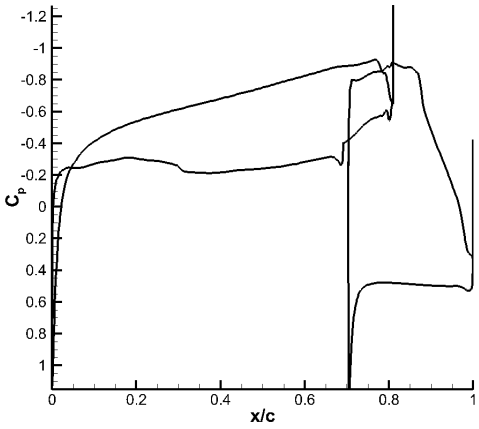
Figure 4.22: LE UWN Cases 5-6 (left) pressure contours (right) lower surface turbulence index



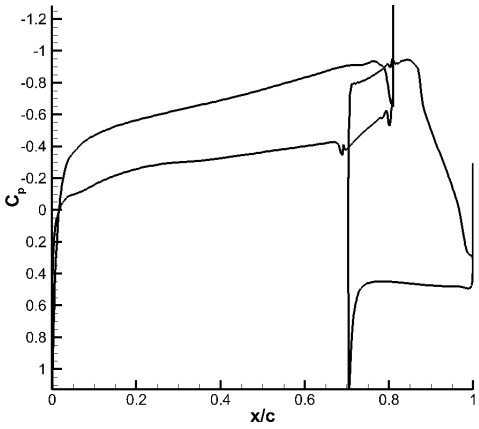
(a) Case 1



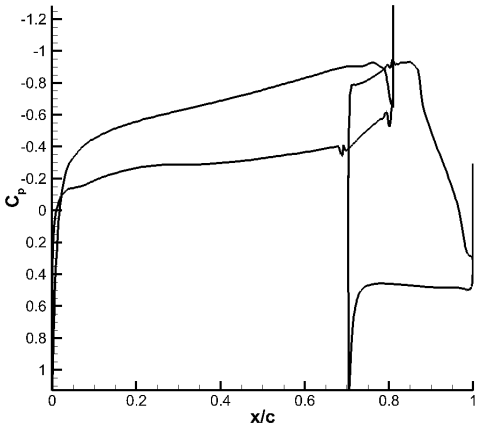
(b) Case 2



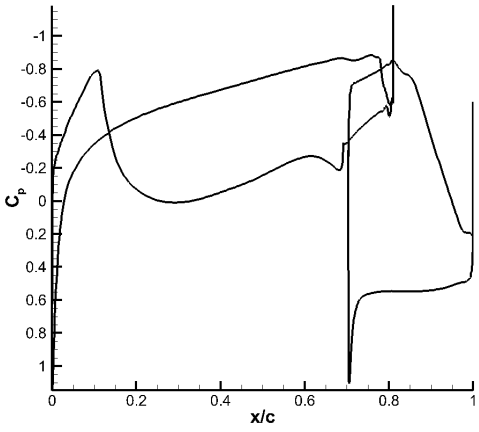
(c) Case 3



(d) Case 4



(e) Case 5



(f) Case 6

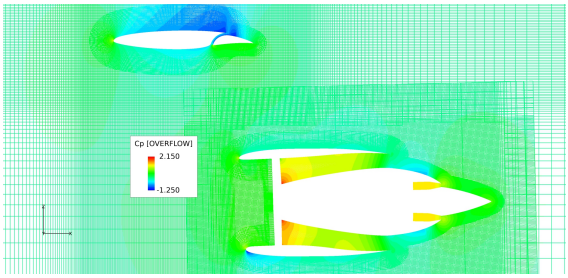
Figure 4.23: S207 surface pressure distribution at Y = 0 for LE UWN configuration

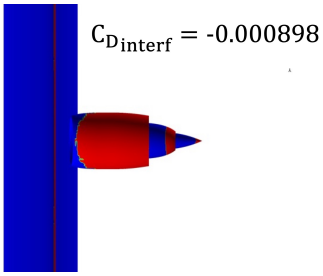
4.6.4 Trailing-Edge/Under-Wing

Results from the S204 integration showed that the the engine must not cause the aft element to separate. If the outer cowling is too close to the slot on the lower surface, the flow through the slot is accelerated. As the flow exited the slot, the flow separated over the aft element due to the shock. In this investigation, the engine was moved further aft of the wing. In Cases 1 and 5, the engine was placed far downward from the wing. The pressure field plots are shown in Figs. 4.24 and 4.25. Both of these positions led to relatively low $\Delta C_{D_{nac}}$ and high ΔC_{D_w}. Case 5 moved the engine 0.23 chord lengths upward. Interference drag was reduced by 22 cts. compared to Case 1. Cases 3 and 4 achieved negative $C_{D_{interf}}$ and 100% laminar flow on the lower surface. Case 4 was located further downstream than Case 3. This resulted in a relatively small increase in $C_{D_{interf}}$. Both Case 3 and Case 4 resulted in a stronger shock on the aft element compared to Case 2. Cases 2 and 6 positioned the nacelle closer vertically than Cases 3 and 4. These configurations resulted in the lowest overall drag. Case 2 resulted in the minimum interference drag for the trailing-edge UWN.

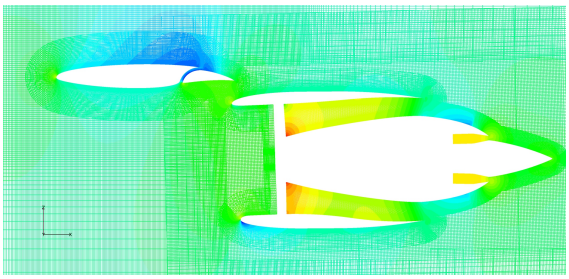
Case 6 setup a stronger shock on the aft element compared to Case 2. This is evident from Fig. 4.26. Relatively large negative wing interference drag was induced by the high pressure region of the nacelle inlet. Case 2 positioned the lip of the nacelle directly under the aft element. This had a favorable interference effect in counteracting drag. On the lower surface of the aft element, this increase is shown in Fig. 4.26b. Case 6 does not show the same region of higher pressure on the aft element.

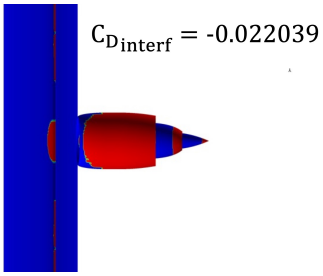
Under-wing aft mounted nacelles like this configuration are not often investigated in literature, but some studies showed that mounting the engine aft of the wing had favorable interference effects [39, 37]. Henderson and Patterson [39] determined that placing the nacelle near the aft portion of the wing created a local increase in lift instead of the local decrease in lift seen from the LE UWN.



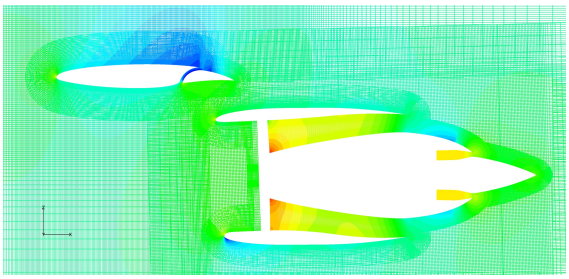


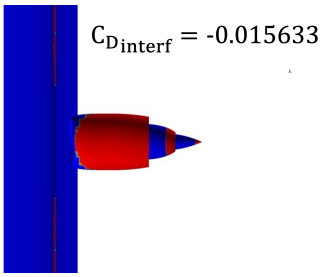
(a) Case 1



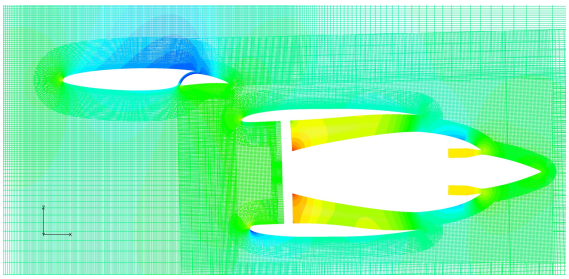


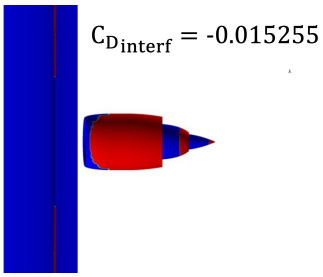
(b) Case 2





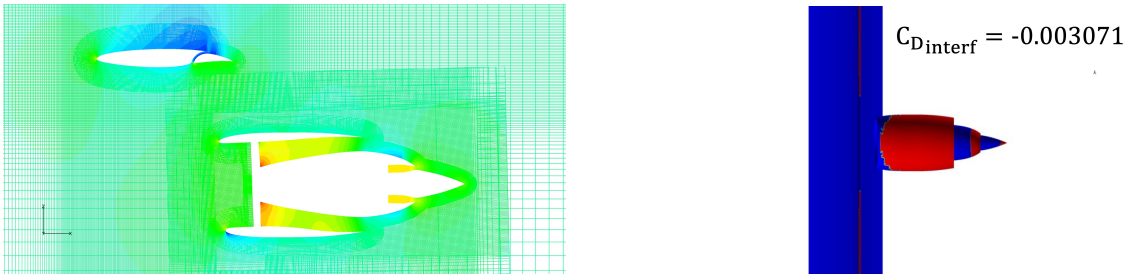
(c) Case 3



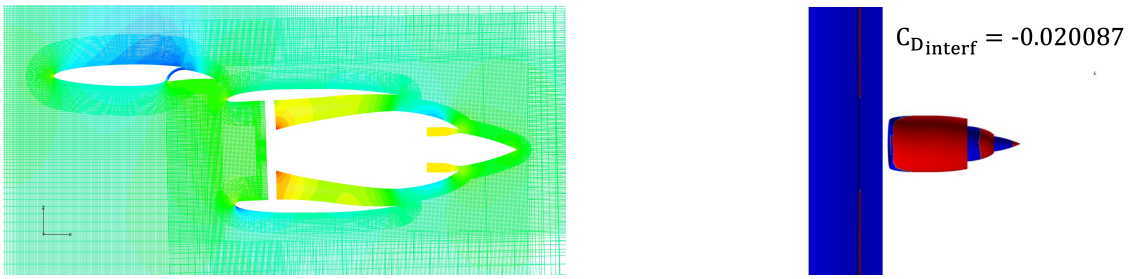


(d) Case 4

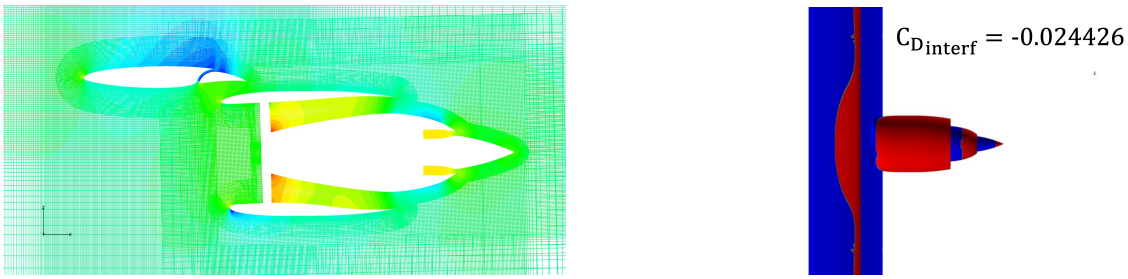
Figure 4.24: TE UWN Cases 1-4 (left) pressure contours (right) lower surface turbulence index



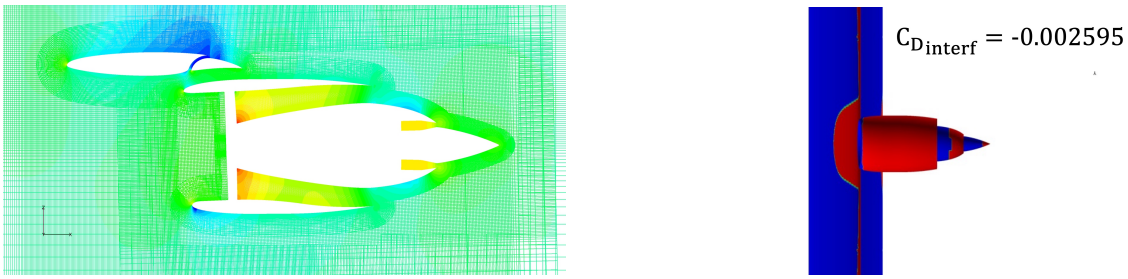
(a) Case 5



(b) Case 6

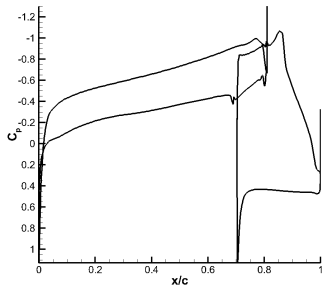


(c) Case 7

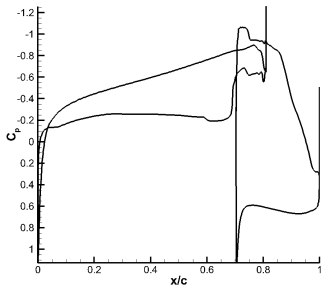


(d) Case 8

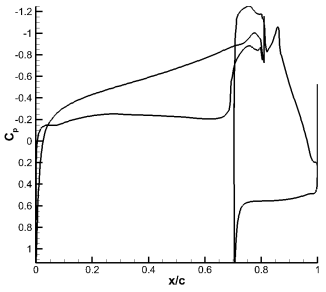
Figure 4.25: TE UWN Cases 5-8 (left) pressure contours (right) lower surface turbulence index



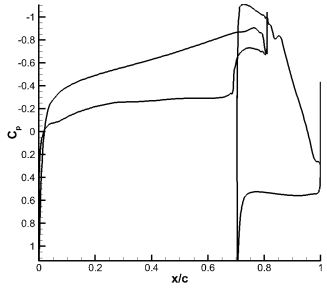
(a) Case 1



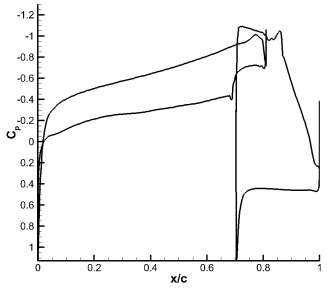
(b) Case 2



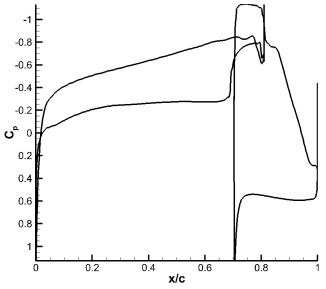
(c) Case 3



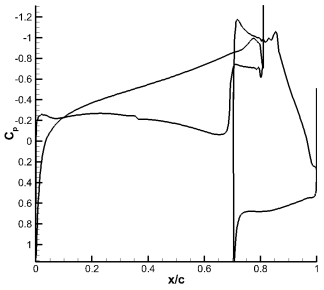
(d) Case 4



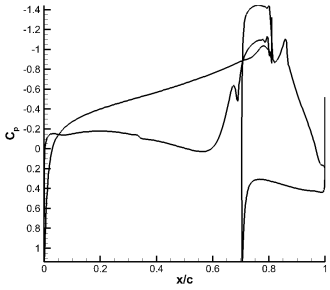
(e) Case 5



(f) Case 6



(g) Case 7



(h) Case 8

Figure 4.26: S207 surface pressure distribution at Y = 0 for TE UWN configuration

In this way the TE UWN acted like a flap. While these engine positions are not mounted to the wing as in previous literature, it is evident that the engine location is promising. It is known that the conventional under-wing nacelle results in noise due sound waves reflected off of the wing lower surface [40]. The TE UWN concept could result in lower community noise.

Chapter 5

Conclusions

The structured, overset CFD code OVERFLOW was used to simulate propulsion/airframe interference effects between a slotted, natural-laminar-flow wing and an ultra-high bypass ratio turbofan. This research further improved the OVERFLOW code by adjusting a boundary condition used to model engine inlets, as the old version was an impromptu scheme that was not reliable. This research implemented a back pressure update based on the isentropic flow relations. This made the back pressure calculation physically meaningful and the more robust. A two-dimensional airfoil in a wind tunnel was simulated at varying reference mach numbers. This simulation validated that the new version is more reliable than the old ah hoc back pressure update.

As a first step to simulating propulsion interference effects, a representative engine model was created by scaling a NASA N+3 reference engine to TTBW cruise conditions. Starting with an outer nacelle cowling sized for the TTBW, the mass flow, total conditions, and ducting geometry were modeled using a 0-D model. The first engine version allowed more than the desired mass flow out of the engine. Flow out the fan nozzle was over-expanded. The fan nozzle duct was altered to more accurately represent the TTBW engine thrust requirement at cruise. Version two of the fan nozzle matched the specified mass flow, and it was deemed adequate to simulated interference

effects. At the nozzle exit, the flow is choked. This matched the engine data of the NASA N+3 engine.

As the final wing design of the TTBW was in progress, the S204 airfoil was studied. The S204 was designed for a business-jet application. A semi-infinite, constant chord wing was meshed in order to simplify the analysis of the wing. A flow-through nacelle was simulated before a powered-on engine. Flight conditions were set to SUGAR Phase I cruise specifications for the TTBW: $M_\infty = 0.745$, $Alt = 44000ft$, and $C_L = 0.60$. This analysis gave qualitative information about how the engine blockage influences laminar flow. It was determined that over-wing nacelles cause the flow to transition much earlier than under-wing nacelles. At the specified flight conditions, no engine locations caused detrimental interference drag.

A powered engine installed on the S204 semi-infinite wing was simulated at the TTBW flight conditions. Only a few positions were investigated, for each of the four engine locations. It was determined that the conventional engine position led to the lowest interference drag. The TE OWN study showed that moving the engine downstream is beneficial. For leading-edge engine configurations, it was determined that the upper surface shock introduced by installation is not detrimental in terms of interference drag. This shock could be taken advantage of in the same way previous research [46, 40]. The candidate TE UWN could not be ruled out due to the strong improvement from position to position. Previous research showed that this location could be beneficial in reducing interference drag [37]. The conventional engine placement (LE UWN) performed the best overall at TTBW cruise Mach numbers.

The finalized airfoil for the TTBW, the S207, was simulated at $M_\infty = 0.70$ instead of $M_\infty = 0.745$ in order to maximize the lift-to-drag ratio. A multitude of engine positions were investigated for all four engine positions supported in literature. For each major position (TE OWN, LE OWN, LE UWN, and TE OWN), placing the engine far from the wing did not create favorable interference

drag. The TE OWN positions showed good improvement as the engine was shifted downstream. Even negative interference drag was calculated. LE OWN induced negative C_{interf} due to the low-pressure region on the wing leading-edge. A low-pressure region at the wing leading-edge allowed for favorable interference drag for the LE UWN, and the flow acceleration led to a shock on the upper wing surface which led to early transition. The TE UWN positions resulted in negative interference drag and negative ΔC_{D_w} for all of the simulated configurations.

The conventional nacelle placement at the leading-edge under-wing led to largely favorable interference effects. The close coupling of the engine and wing created a suction peak on the wing lower surface; however, placing the engine too close was not favorable. Shifting the engine too far upstream increased interference drag dramatically. The overall best performing engine location was found to be the trailing-edge UWN. This location created a similar effect as a flap. Case 2 performed the best out of all tested engine locations.

For conventional commercial aircraft such as the Boeing 737, the aft-mounted engine position is likely not viable. Landing gear would have to be excessively long and heavy to accommodate a trailing edge nacelle at landing and takeoff. At lower Mach numbers, the OWN is less beneficial. OWNs generally performed worse than under-wing locations.

The TTBW is still in the early stages of development, and it is not clear which design considerations will determine where the engine is located. The high wing of the TTBW will allow more than enough ground clearance for either under-wing locations. It is likely that an over-wing position could be too troublesome for regular access to maintenance. If low engine noise is desired, however, then an over-wing configuration may be ideal. It was the goal of this research to minimize interference drag at cruise. Based upon these findings, the trailing-edge under-wing Case 2 out performed all other candidate positions. The TE UWN position has the potential for noise reduction as well because sound radiated from the nozzle would not be reflected downward. Sound

waves may still reach the ground, but less than the conventional UWN. Both leading-edge locations created negative $C_{D_{interf}}$. The conventional under-wing nacelle allowed more upper surface laminar flow compared to the LE OWN.

A consistent approach to examining integration effects for semi-infinite wings should be established. The investigations of the S204 and S207 showed inconsistent results due to the chose reference areas, and interference drag calculations for the S207 were orders of magnitude different than the isolated wing. Thus, three-dimensional integration effects are essential for finalizing the engine position and minimizing interference drag. The UWN locations showed potential for minimizing interference drag, and a high wing design such as the TTBW allows the TE UWN ample ground clearance at takeoff and landing. The engine should be integrated onto the full TTBW three-dimensional wing with the pylon. The effect of surface contouring the wing/nacelle/pylon should be investigated. Previous research has shown that contouring can minimize or create negative interference drag.

Bibliography

[1] (1999). http://www.b737.org.uk/history.htm. ix, 1, 2

[2] (2005). Boeing 747 jumbo-jet history. http://www.modernairliners.com/boeing-747-jumbo/boeing-747-jumbo-history/. 1

[3] (2014). The mighty dc-9. https://airwaysmag.com/uncategorized/mighty-dc-9/. 4

[4] (2017). Hondajet: Pilot review: What's it like to fly? https://www.avbuyer.com/articles/jets-for-sale-review/hondajet-pilot-review-what-s-it-like-to-fly-112050. ix, 18

[5] (2018). Aviation history. https://www.geaviation.com/company/aviation-history. Last accessed Jan 13, 2019. 3, 23

[6] (2019). Boeing 757. https://en.wikipedia.org/wiki/Boeing_757. 3, 4

[7] (2019). Civil aerospace. https://www.rolls-royce.com/products-and-services/civil-aerospace/airlines/. Last accessed Jan 13, 2019. 3

[8] (2019). Commercial engines. https://www.pw.utc.com/products-and-services/products/commercial-engines/. Last accessed Jan 13, 2019. 3

[9] (2019). Honda ha-420 hondajet. https://en.wikipedia.org/wiki/Honda_HA-420_HondaJet. 53

[10] (2019). Nasa university leadership initiative. https://nasa-uli.utk.edu. ix, 6

[11] Allmaras, S. R., Johnson, F. T., and Spalart, P. R. (2012). Modications and claricatios for the implementation of the spalart-allmaras turbulence model. Seventh International Conference on Computational Fluid Dynamics (ICCFD7). 33

[12] Antonatos, P. P., S. L. E. and Stave, D. L. (1972). Inlet/Airplane Interference and Integration. Number 53. Advisory Group for Aerospace Research and Development. 10

[13] Bardina, J. and Lombard, C. K. (1987). Three dimensional hypersonic flow simulations with the cscm implicit upwind navier-stokes method. Number 87-1114. AIAA. 33

[14] Benson, T. (Jun 2014). Engines. `https://www.grc.nasa.gov/www/k-12/UEET/StudentSite/engines.html`. Last accessed Jan 11, 2019. 1

[15] Berry, D. L. (1994). The Boeing 777 Engine/Aircraft Integration Aerodynamic Design Process. *International Council of Aeronautical Sciences*. ix, 4, 13, 14, 22, 24, 25, 55, 56

[16] Blaesser, N. J., Schetz, J. A., and Kapanta, R. K. (2019). Interference drag assocated with engine locations for multidisciplinary design optimization. AIAA Scitech 2019 Forum, AIAA SciTech Forum (AIAA 2019-0259). 5, 8, 21, 22, 46, 62, 70

[17] Bradley, M. K., D. C. K. and Allen, T. K. (2015). *Subsonic Ultra Green Aircraft Research: Phase II – Volume I – Truss Braced Wing Design Exploration*. Boeing Research & Technology, Huntington Beach, California. Retrieved from `https://ntrs.nasa.gov/archive/nasa/casi.ntrs.nasa.gov/20150017036`. 6, 22, 23

[18] Bradley, M. K. and Droney, C. K. (2011). *Subsonic Ultra Green Aircraft Research: Phase I Final Report*. Boeing Research & Technology, Huntington Beach, California. Retrieved from `https://ntrs.nasa.gov/search.jsp?R=20110011321`. ix, 5, 6, 9, 10, 22, 23, 46, 53, 54

[19] Brazier, M. E. and Ball, W. H. (1975). Accounting of Aerodynamic Forces on Airframe/Propulsion Systems. Number 150. Advisory Group for Aerospace Research and Development. 24

[20] Broderson, O. and Stürmer, A. (2001). Drag Prediction of Engine-Airframe Interference Effects Using Unstructured Navier-Stokes Calculations. *American Institute of Aeronautics and Astronautics*. 16

[21] Carlson, J. R. and B. Compton, III, W. (1984). An experiments investigation of nacelle-pylon installation of an unswept wing at subsonic and transonic speeds. Technical report, NASA. 11

[22] Carlson, J. R. and Lamb, M. (1987). Integration effects of pylon geometry and rearward mounted nacelles for a high-wing transport. *American Institute of Aeronautics and Astronautics*. ix, 10, 12, 13, 22

[23] Carrick, E. (2019). Airlines extend flight cancelations into the summer due to boeing 737 max 8 grounding. `https://www.travelandleisure.com/airlines-airports/airlines-announce-flight-cancellations-due-to-boeing-737-max-8-grounding`. 2

[24] Chan, W. M., III, R. J. G., Rogers, S. E., and Buning, P. G. (2002). Best practices in overset grid generation. 32nd AIAA Fluid Dynamics Conference (AIAA 2002-3191). 40, 48, 53

[25] Coder, J. G. (2017). Enhancement of the amplification factor transport transition modeling framework. AIAA SciTech Forum, 55th AIAA Aerospace Sciences Meeting. 35

[26] Coder, J. G. and Maughmer, M. D. (2014). Computational fluid dynamics compatible transition modeling using an amplification factor transport equation. *AIAA Journal*, 52(11). 35

[27] Coder, J. G., Pulliam, T. H., and Jensen, J. C. (2018). Contributions to hiliftpw-3 using structured, overset grid methods. Kissimmee, Florida. AIAA SciTech Forum, 2018 AIAA Aerospace Sciences Meeting. 35, 36, 37, 38

[28] Drela, M. (1998). Mises implementation of modified abu-ghannam/shaw transition criterion (second revision). Technical report, Massachusetts Institute of Technology Dept. of Aeronautics and Astronautics. 38

[29] Drela, M. (2009). Power balance in aerodynamic flows. *AIAA Journal*, 47(7):1761–1771. 26, 27, 55

[30] Drela, M. and Giles, M. B. (1987). Viscous-inviscid analysis of transonic and low-reynolds number airfoils. *AIAA Journal*, 25(10):1347–1355. 35

[31] Ewald, B. and Smyth, R. (1981). The Role and Implementation of Different Nacelle/Engine Simulation Concepts for Wind-Tunnel Testing in Research and Development Work on Transport Aircraft. Number 301. Advisory Group for Aerospace Research and Development. 10, 11

[32] Ferri, A. (1972). Engine Airplane Interference - Definition of the Problem and Related Basic Fluid Dynamic Phenomena. Number 53. Advisory Group for Aerospace Research and Development. 10

[33] Fuhs, A. E. (1972). Engine Integration and Thrust/Drag Definition. Number 53. Advisory Group for Aerospace Research and Development. 10, 11

[34] Fujino, M. (2003). Design and development of the hondajet. Number 2003-2530. AIAA/ICAS International Air and Space Symposium and Exposition: The Next 100 Years, American Institute of Aeronautics and Astronautics. 53

[35] Fujino, M. and Kawamura, Y. (2003). Wave-Drag Characteristics of an Over-the-Wing Nacelle Business-Jet Configuration. *Journal of Aircraft*. 5, 17, 18, 22, 58, 61, 62, 71

[36] Godunov, S. K. (1959). A difference method for numerical calculation of discontinuous solutions of the equations of hydrogynamics. *Mat. Sb. (N.S.)*, 47(89):271–306. 32

[37] Henderson, W. P. (1990). Airframe/propulsion integration characteristics at transonic speeds. *The American Society of Mechanical Engineers*. 11, 12, 13, 22, 58, 65, 70, 85, 91

[38] Henderson, W. P. and Abeyounis, W. K. (1985). Aerodynamic characteristics of a high-wing transport configuration with an over-the-wing nacelle-pylon arrangement. Technical report, NASA. 12, 17

[39] Henderson, W. P. and Patterson, Jr., J. P. (1983). Propulsion installation characteristics for turbofan transports. *American Institute of Aeronautics and Astronautics*. 11, 12, 22, 65, 81, 85

[40] Hill, G. A., Kandil, O. A., and Hahn, A. S. (2009). Aerodynamic investigations of an advanced over-the-wing nacelle transport aircraft configuration. *Journal of Aircraft*, 46(1):25–35. viii, ix, 18, 19, 20, 22, 44, 53, 58, 63, 68, 77, 89, 91

[41] Hoerner, S. F. (1965). *Fluid-Dynamic Drag*. Hoerner Fluid Dynamics, Bakersfield, CA. 10

[42] Hoheisel, H. (1997). Aerodynamic aspects of engine-aircraft integration of transport aircraft. *Aerospace Science and Technology*, 1(7):475–487. 3

[43] Hooker, J. R., Wick, A., Zeune, C., and Agelastos, A. (2013). Over Wing Nacelle Installations for Improved Energy Efficiency. *31st AIAA Applied Aerodynamics Conference*. doi: 10.2514/6.2013-2920. ix, 5, 20, 21, 22, 25, 26, 27, 55, 56, 62, 63, 65, 70, 81

[44] Jaarsma, F. (1972). Experimental Determination of Nozzle Characteristics and Nozzle Airframe Interference. Number 53. Advisory Group for Aerospace Research and Development. 10, 11

[45] Jones, M. S., W. J. H. and Tong, M. T. (2017). An n+3 technology level reference propulsion system. Technical report, NASA, Glenn Research Center, Cleveland, Ohio. viii, 3, 22, 23, 45, 46, 51, 56

[46] Kinney, D. J., Hahn, A. S., and Gellhausen, P. A. (1997). Comparison of Low and High Nacelle Transport Configurations. *American Institute of Aeronautics and Astronautics*. ix, 15, 16, 18, 19, 22, 63, 68, 91

[47] Klopfer, G. H., der Wijngaart, R. F. V., Hung, C. M., and Onufer, J. T. (1998). A diagonalized diagonal dominant alternating direction implicit (d3adi) scheme and subiteration correction. *AIAA Journal*. 33

[48] Laflin, K. R., Vassberg, J. C., Wahls, R. A., Morrison, J. H., Brodersen, O., Rakowitz, M., Tinoco, E. N., and Godard, J.-L. (2004). Summar of data from the second aiaa cfd drag prediction workshop (invited). Number 2004-555. 42nd AIAA Aerospace Sciences Meeting and Exhibit, AIAA. 17

[49] Lange, F. (2018). Aerodynamic optimization of an uhbr engine position on a representative short range aircraft configuration at cruise flight conditions. 2018-3811. 2018 Applied Aerodynamics Conference, AIAA AVIATION Forum (AIAA 2018-3811). 4, 21, 22, 65, 70, 81

[50] Langtry, R. B., Kuntz, M., and Menter, F. R. (2005). Drag Prediction of Engine-Airframe Interference Effects with CFX-5. *Journal of Aircraft*. 17, 33

[51] Lee, Jr., E. E. and Pendergraft, Jr., O. C. (1985). Installation effects of long-duct pylon mounted nacelles on a twin-jet transport model with swept supercritical wing. Technical report, NASA. 12, 21

[52] Loftin, L. K., Jr. (1985). *Quest for Performance: The Evolution of the Modern Aircraft*. NASA History Office. `https://history.nasa.gov/SP-468/ch10-3.htm`. 1

[53] Malouin, B., Martin Garièpy, J.-Y. T., and Laurendeau, E. (2015). Internal Drag Evaluation for a Through-Flow Nacelle Using a Far-Field Approach. *Journal of Aircraft*, 52(6). doi: 10.2514/1.C033093. 25

[54] Menter, F. R., Smirnov, P. E., Liu, T., and Avancha, R. (2015). A one-equation local correlation-based transition model. *Flow Turbulence and Combustion*, 95(4):583–619. 38

[55] Ministry-Industry Drag Analysis Panel (MIDAP) Study Group (1979). Guide to in-flight thrust measurement of turbojets and fan engines. Technical Report 237, AGARD. 24, 55

[56] Nichols, R. H. and Buning, P. G. (2017). User's manual for overflow 2.2. https://overflow.larc.nasa.gov/home/users-manual-for-overflow-2-2/. 32, 35, 38, 48

[57] Nichols, R. H., Denny, A. G., Calahan, J. A., Savelle, S. A., and Heikknen, B. D. (2011). *Firebolt* v1.0 - Coupling of Transient and Steady Engine Performance Models with a High-Fidelity Navier-Stokes Code. *American Institute of Aeronautics and Astronautics*. 39, 42, 46

[58] Nichols, R. H., Tramel, R. W., and Buning, P. G. (2006). Solver and turbulence model upgrades to overflow 2 for unsteady and high-speed applications. Number 2006-2824. 25th Applied Aerodynamics Conference, American Institute of Aeronautics and Astronautics. 33

[59] Pulliam, T. H. and Chaussee, D. S. (1981). A diagonal form of an implicit approximate factorization algorithm. *Journal of Computational Physics*, 39:347–363. 33

[60] Pulliam, T. S. and Steger, J. L. (1980). Implicit finite-difference simulations of three-dimensional compressible flow. *AIAA Journal*, 18(2). 28

[61] Reubush, D. E. (1979). Effect of over-the-wing nacelles on wing-body aerodynamics. *Journal of Aircraft*. 11, 12, 17

[62] Roe, P. L. (1981). Approximate riemann solvers, parameter vectors, and difference schemes. *Journal of Computational Physics*, 43:357–372. 32

[63] Rossow, C.-C., Goddard, J.-L., Hoheisel, H., and Schmitt, V. (1994). Investigations of propulsion integration interference effects on a transport aircraft configuration. *Journal of Aircraft*, 31(5):1022–1030. ix, 14, 15, 16, 24, 44, 53, 58, 70

[64] Rossow, C.-C. and Hoheisel, H. (1994). Numerical Study of Interference Effects of Wing-Mounted Advanced Engine Concepts. *International Council of Aeronautical Sciences*. 2, 9, 15, 17, 22, 65, 68, 81

[65] Rudnik, R., Rossow, C.-C., and v. Gehr, H. F. (2002). Numerical Simulation of Engine/Airframe Integration for High-bypass Engines. *Aerospace Science and Technology*. 9, 16, 17, 22, 81

[66] Somers, D. M. (2012). Design of a Slotted, Natural-Laminar Flow Airfoil for Business-Jet Applications. Technical report, Airfoils, Incorporated, Port Matilda, Pennsylvania. NASA/CR–2012-217559. ix, 6, 7, 53, 54

[67] Spalart, P. R. and Allmaras, S. R. (1992). A one-equation turbulence model for aerodynamic flows. 30th Aerospace Sciences Meeting & Exhibit, American Institute of Aeronautics and Astronautics. 33, 34, 54

[68] Stankowski, T. P., MacManus, D. G., Robinson, M., and Sheaf, C. T. (2017). Aerodynamic effect of propulsion integration for high bypass ration engines. *Journal of Aircraft*, 54(6):2270–2284. ix, 8, 21, 24, 25, 26, 44, 45, 46, 81

[69] Stankowski, T. P., MacManus, D. G., Sheaf, C. T., and Grech, N. (2016). Aerodynamics of aero-engine installation. AIAA Aerospace Sciences Meeting, AIAA SciTech Forum (AIAA 2016-0764). 45, 55

[70] Torenbeek, E. (2013). *Advanced Aircraft Design: conceptual design, technology, and optimization of subsonic civil airplanes.* John Wiley and Sons, Inc. Retrieved from http://ebookcentral.proquest.com. ix, 1, 2, 3, 9

[71] Tramel, R. W., Nichols, R. H., and Buning, P. G. (2009). Addition of improved shock-capturing schemes to overflow 2.1. Number 2009-3988. 19th AIAA Computational Fluid Dynamics Conference, American Institute of Aeronautics and Astronautics. 32, 33

[72] van Dam, C. P. (1999). Recent experience with different methods of drag prediction. volume 35, pages 751–798. Progress in Aerospace Sciences, Pergamon. 26

[73] Vassberg, J. C. (2016). Challenges and Accomplishments of the AIAA CFD Drag Predicition Workshop Series. Technical report, The Boeing Company. 17

[74] White, F. M. (1991). *Viscous Fluid Flow.* McGraw-Hill, Inc., 2nd edition. 6, 7, 68

[75] Zonars, D. (1972). Dynamic Characteristics of Engine Inlets. Number 53. Advisory Group for Aerospace Research and Development. 10

Vita

David Palmer was born in Memphis, TN. He is one of five children to Betty and Bob Palmer. His siblings are Rob, Sarah, James, and Virgie. David graduated from the University of Memphis with a Bachelor's of Science in Mechanical Engineering in 2017. He then decided to pursue a Master's of Science degree in Mechanical Engineering at the University of Tennessee.